People's Democratic Republic of Algeria
Ministry of Higher Education and Scientific Research
Ferhat Abbas-Setif1 University
Faculty of Sciences
Department of Physics

Thesis Submitted for the Degree of Doctor 3rd Cycle LMD of Physics in

Material Physics

Title:

Synthesis and characterization of mixed oxides: experimental and theoretical study of their photocatalytic activity

Presented by: **BOURIACHI Sarra**

Board of Examiners:

Pr. BOUKELKOUL Mebarek	University of Setif 1	President
Pr. HADDADI Khelifa	University of Setif 1	Supervisor
Dr. HAMICI Melia	University of Setif 1	Co- Supervisor
Dr. GUERBOUS Lakhdar	Nuclear Research Centre of Algiers	Examiner
Dr. MEDKOUR Youcef	University of Setif 1	Examiner
Dr. MOULKIA Hassiba	University of Oum El Bouaghi	Examiner

- December 05, 2024-

Acknowledgments

This PhD work was performed in the “Emergent Materials Research Unit (EMRU)) and “Laboratory of Dosing, Analysis and Characterization with High Resolution (DAC-hr)” at the University of Ferhat Abbas Sétif-1.

First of all, I wish to express my deepest gratitude to my supervisors Pr. HADDADI Khelifa and Dr. HAMICI Melia for their valuable advice, guidance and outstanding supervision. It has been a pleasure to work and learn under your guidance since March 2021.

I would like to thank my friend FOUDIA Lamis for her encouragement throughout this period.

A special acknowledgment to my uncle, Dr. BOUDRAA Lahcene, for believing in me and encouraging me to pursue a PhD and also for always being there whenever I needed anything.

Finally, a big thank you to my family. My mother and father, your love and support has always kept me going, and I would not be here without you. My brother and sisters, thank you for being there for me and supporting me unconditionally. I offered my gratitude to my in-laws for their unwavering support at every possible step during the three previous years. My husband, you put up with me all along and it wasn’t easy for you, but you were there all the way, thank you.

This thesis is dedicated to my little Isra.

List of Figures

Chapter I

Chapter II

Chapter III

Chapter IV

Chapter V

Chapter VI

List of Tables

Chapter I

Chapter IV

Chapter V

Chapter VI

Content

Chapter I: Literature Review

Chapter II: Experimental Techniques

Chapter III: Theoretical Methods

Chapter IV: Synthesis and Characterization of $LaFeO_3$ Perovskite

Chapter V: Adsorption and Photocatalytic Activities

Chapter VI: DFT Calculation of $LaFeO_3$ Properties and MB Adsorption

General Introduction

Water pollution represents one of the most world's pressing issues, which could be attributed to the accelerated demand for textiles, plastics, printing, paper industry, and cosmetics; approximately 14 billion pounds of plastics, 706 million gallons of oil, 300 - 400 metric tons of waste that contains heavy metals and toxic sludge are dropped into the ocean every year [1]. Based on the UN World Water Development Report, between 2.2 and 3.2 billion people, which corresponds to 32 - 46% of the world population, lived under water stress in 2010 [2]. According to the World Health Organization, about 1 million people and 395,000 children under the age of five are estimated to die each year from diseases related to poor sanitation, hygiene, or unsafe water [3]. Around 80% of the global wastewater is released to the environment without treatment [4], where 17 - 20% of the water pollution is contributed by dyeing [4,5]. Organic dyes with a stable and complicated polyaromatic structure, are resistant to environmental conditions and non-biodegradable [6]. Methylene Blue (MB) is considered one of the most aromatic basic dyes used in the textile industry, including coloring silk, wool, cotton, and paper [7], where large amounts of MB dye are released into natural water sources. Above certain concentrations, MB dye is considered toxic and carcinogenic which presents a potential threat to the environment and human health [7]. Therefore, a lot of efforts are afforded to develop suitable wastewater treatment methods, such as photo-Fenton treatment, oxidation, catalytic peroxymonosulfate activation, ozonation, electrochemical oxidation, and combined methods. Among the various wastewater treatment methods, adsorption and photocatalysis are considered advantageous methods for several organic pollutants' removal due to their low costs, high efficiency, ease of application, and environmental friendliness. Adsorption is a surface phenomenon where the adsorbent is accumulated on the adsorbent surface while photocatalysis is known as a light-activated reaction involving a semiconductor photocatalyst. The combination of adsorption and photocatalysis processes is a one-step treatment that can increase the removal efficiency [8,9].

Mixed oxides with the ABO_3 perovskite-type structure have attracted considerable attention for use as gas sensors, photocatalytic systems, solid oxide fuel cells, and magnetic devices [10-12] due to their high thermal stability, non-toxicity, excellent electronic, optical, and magnetic properties [13,14]. Among the ABO_3 perovskite family, lanthanum ferrite $LaFeO_3$ is one of the most promising photocatalytic materials that could be attributed to its structural stability and narrow band gap of 2.1 - 2.6 eV [15,16]. G-type antiferromagnetic $LaFeO_3$ perovskite with orthorhombic structure is known to show different characteristics depending on synthetic conditions. Anajafi et *al.* have investigated the influence of the synthetic method, microwave-thermal treatment, hydrothermal, and sol-gel methods, on the different $LaFeO_3$ properties: the morphology of the synthesized samples is affected by the considered method and small band gap values were obtained for hydrothermal method [17]. Singh et *al*. [18] have studied the effect of temperature on the physical properties of the $LaFeO_3$ powder; their results revealed that the crystallite size of the prepared samples increases with an increase in calcination temperature, which is accompanied by a decrease in the specific surface area. The moment of an anti-ferromagnetic particle was also found to increase with decreasing particle size. Hongfang et *al.* showed that the $LaFeO_3$ nanoparticles, prepared through the sol-gel method and calcined by vacuum microwave calcination, exhibit high photocatalytic performance for the degradation of methylene orange (MO) and methylene blue (MB) compared to those calcined by conventional calcination [19]. Kamal et *al*. investigated the effect of the citric acid-to-metal ratio on the crystallinity, band gap, and particle size, where the molar ratio varied from 2 to 16. The results showed that smaller particle size was found at high citric acid ratios; also, the crystallinity and band gap of the prepared samples are affected by the citric acid ratio [15].

Despite the several works and studies reported on the $LaFeO_3$ perovskite, the effect of precursors on its physicochemical properties and its catalytic and photocatalytic performance have not yet been explored, which will be the subject of the present manuscript. The manuscript is composed of six chapters. The first chapter provides a literature review of the different topics considered in the thesis: an overview of the organic dyes including the dye considered during the realization of this thesis, the water treatment methods where the adsorption and photocatalytic processes are highlighted. The perovskite structure, magnetic properties, and electronic structures of $LaFeO_3$ are also addressed in this chapter.

The second chapter describes the experimental process “sol-gel” used to elaborate the $LaFeO_3$ powders, including its principle, basic reactions in the sol-gel procedure, and the main factors influencing this process. Additionally, it provides a brief presentation of the different techniques considered to characterize the physicochemical properties of the synthesized powders.

In the third chapter, we provide an introduction to basic molecular quantum mechanics. Subsequently, we delve into a comprehensive presentation of density functional theory (DFT), starting from the Hohenberg-Kohn theorem and extending to the plane-wave pseudopotential approach. The concluding section of this chapter is dedicated to discussing the DFT codes utilized in the course of this thesis.

Chapter Four outlines the synthesis procedure of $LaFeO_3$ nanoparticles, followed by a detailed examination of their various properties, including crystallinity, specific surface area, morphology, porosity, optical properties, and functional groups.

Chapter Five is divided into two main sections. Initially, we extensively discuss the adsorption of methylene blue on the $LaFeO_3$ surface. We fit the kinetics of adsorption to pseudo-first and second-order models, as well as the Elovich model, and analyze the adsorption mechanism using the intraparticle diffusion model. Furthermore, we study the adsorption isotherm through the Langmuir and Freundlich models, followed by a thermodynamic adsorption analysis. The second part of this chapter focuses on the photocatalytic study of $LaFeO_3$ nanoparticles, where we fit the kinetics of methylene blue photodegradation to the pseudo-first-order rate equation.

The first section of the final chapter examines the structural and electronic properties of G-type antiferromagnetic $LaFeO_3$ and surface optimization. In the subsequent section, we investigate methylene blue adsorption on (121) and (100) surfaces, presenting the adsorption properties such as adsorption energy, adsorbent-adsorbate distance, and estimated interactions involved during the adsorption process.

Aim and Objectives

The objective of this research was twofold: firstly, to synthesize a mixed oxide with the formulation $LaFeO_3$ adopting the perovskite structure using the sol-gel method for photocatalytic applications. Two salt precursors, namely nitrate salts and chloride salts, were utilized in the elaboration of this perovskite. The impact of these salt precursors on the thermal behavior, morphology, surface area, structural and optical properties, as well as adsorption and photocatalytic activities, will be comprehensively examined. The adsorption and photocatalytic activities of the synthesized $LaFeO_3$ perovskites were evaluated through the degradation of methylene blue (MB) dye. Moreover, this thesis seeks to conduct an in-depth analysis of both bulk and surface properties of the $LaFeO_3$ perovskite using the CASTEP and Dmol^3 packages within the framework of density functional theory. Additionally, the adsorption of MB on the $LaFeO_3$ surface will be investigated.

References

[1] Globe Water, Water pollution statistics, https://www.globewater.org/, 2022.

[2] Koncagül, E., & Connor, R. (2023). The United Nations World Water Development Report 2023: partnerships and cooperation for water; facts, figures and action examples.

[3] *World Health Organization. (2023, September 13). Drinking-water*

[4] Water, U. N. (2020). Water and climate change. *The United Nations World Water Development Report*.

[5] Roy, M., & Saha, R. (2021). Dyes and their removal technologies from wastewater: A critical review. *Intelligent environmental data monitoring for pollution management*, 127-160.

[6] Khan, I., Khan, I., Usman, M., Imran, M., & Saeed, K. (2020). Nanoclay-mediated photocatalytic activity enhancement of copper oxide nanoparticles for enhanced methyl orange photodegradation. *Journal of Materials Science: Materials in Electronics*, *31*, 8971-8985. DOI: 10.1007/s10854-020-03431-6.

[7] Khan, I., Saeed, K., Zekker, I., Zhang, B., Hendi, A. H., Ahmad, A., ... & Khan, I. (2022). Review on methylene blue: Its properties, uses, toxicity and photodegradation. *Water*, *14*(2), 242. DOI: 10.3390/w14020242.

[8] Bi, Y., Sun, E., Zhang, S., Du, F., Wei, H., Liu, F., & Zhao, C. (2021). Synergistic effect of adsorption and photocatalysis for the degradation of toluene by TiO2 loaded on ACF modified by Zn (CH3COO) 2. *Environmental Science and Pollution Research*, *28*(40), 57398-57411. DOI: 10.1007/s11356-021-14539-5.

[9] Andronic, L., Isac, L., Cazan, C., & Enesca, A. (2020). Simultaneous adsorption and photocatalysis processes based on ternary TiO2–CuxS–fly ash hetero-structures. *Applied Sciences*, *10*(22), 8070. DOI: 10.3390/app10228070.

[10] Haye, E., Capon, F., Barrat, S., Boulet, P., Andre, E., Carteret, C., & Bruyere, S. (2016). Properties of rare-earth orthoferrites perovskite driven by steric hindrance. *Journal of Alloys and Compounds*, *657*, 631-638. DOI: 10.1016/j.jallcom.2015.10.135.

[11] Sun, R., Yan, J., Shen, L., & Bai, H. (2020). Performance and mechanism study of LaFeO 3 for biomass chemical looping gasification. *Journal of Materials Science*, *55*, 11151-11166. DOI: 10.1016/j.jallcom.2015.10.135.

[12] Behara, S., & Thomas, T. (2020). Stability and amphotericity analysis in rhombohedral ABO3 perovskites. *Materialia*, *13*, 100819. DOI: 10.1016/j.mtla.2020.100819.

[13] Li, S., Guo, M., Wang, X., & Gao, K. (2020). Fabrication and photocatalytic activity of LaFeO3 ribbon-like nanofibers. *Journal of the Chinese Chemical Society*, *67*(6), 990-997. DOI: 10.1002/jccs.201900431.

[14] García, F. E., Litter, M. I., & Sora, I. N. (2021). Assessment of the arsenic removal from water using Lanthanum Ferrite. *ChemistryOpen*, *10*(8), 790-797. DOI: 10.1002/open.202100065.

[15] García, F. E., Litter, M. I., & Sora, I. N. (2021). Assessment of the arsenic removal from water using Lanthanum Ferrite. *ChemistryOpen*, *10*(8), 790-797. DOI: 10.1002/open.202100065.

[16] Phan, T. T. N., Nikoloski, A. N., Bahri, P. A., & Li, D. (2018). Optimizing photocatalytic performance of hydrothermally synthesized LaFeO3 by tuning material properties and operating conditions. *Journal of environmental chemical engineering*, *6*(1), 1209-1218. DOI: 10.1016/j.jece.2018.03.053

[17] Anajafi, Z., Naseri, M., & Neri, G. (2019). Optical, magnetic and gas sensing properties of LaFeO 3 nanoparticles synthesized by different chemical methods. *Journal of Electronic Materials*, *48*, 6503-6511. DOI: 10.1007/s11664-019-07436-8.

[18] Singh, S., & Singh, D. (2017). Synthesis of LaFeO 3 nanopowders by glycine–nitrate process without using any solvent: effect of temperature. *Monatshefte für Chemie-Chemical Monthly*, *148*, 879-886.

[19] Shen, H., Xue, T., Wang, Y., Cao, G., Lu, Y., & Fang, G. (2016). Photocatalytic property of perovskite LaFeO3 synthesized by sol-gel process and vacuum microwave calcination. *Materials Research Bulletin*, *84*, 15-24.

Chapter I:
Literature Review

Mixed oxides are considered one of the most attractive class of compounds. Regarding their structural properties, they could be divided into different categories. Among mixed oxides, perovskite-type structure has been a subject of constant attention since the 1970s due to their multitude of structures and properties.

This chapter provides a literature review of the different topics considered in the thesis. The first section of this chapter is an overview of the organic dyes including the dye considered during the realization of this thesis, the second section is dedicated to the water treatment methods where the adsorption and photocatalytic processes are highlighted. The last part is devoted to the perovskite structure with an emphasis on the $LaFeO_3$ structure: crystalline, magnetic, and electronic structures in addition to the surface studies of $LaFeO_3$.

I.1 Organic Dyes

Among the large list of organic pollutants, organic dyes represent one of the most popular water pollutants. Dyes are largely utilized in many industrial fields such as; textiles, fabric, cosmetics, pharmaceutical and food industries, pulp and paper, and printing. These organic dyes are mostly carbon-based, generally, they have a stronger and more stable molecular configuration than inorganic colorants [1,2]. Generally, dyes are applied to substrates to give them permanent color, therefore, their properties are improved to give a high resistance to light, sweat, water, microbial attack and oxidizing agents [3]. Most of these synthetic dyes are non-biodegradable, toxic and carcinogenic either to humans or living organisms in the aquatic environment [3]. Dyes are classified into cationic, anionic and nonionic dyes [4]. Anionic dyes depend on a negative ion where most of them form a covalent bond [4]. Anionic dyes include direct, acid and reactive dyes with common characteristics; water-solubilizing and ionic substituents [4,5]. Cationic dyes are also known as basic dyes where they carry a positive charge in their molecule. This type of dye is highly visible with high brilliance and intensity of color [4]. Nonionic dyes are known as dispersed dyes due to their non-ionization in an aqueous medium [5].

Methylene blue with the chemical formula $C_{16}H_{18}N_3ClS$ is one of the most aromatic basic dyes used in the textile industry. The structure of methylene blue (MB) is illustrated in Figure I.1. It is a solid, odorless, dark blue-green color in powder and blue color when dissolved in water with a molecular weight of 319.85 g mol^{-1} [3].

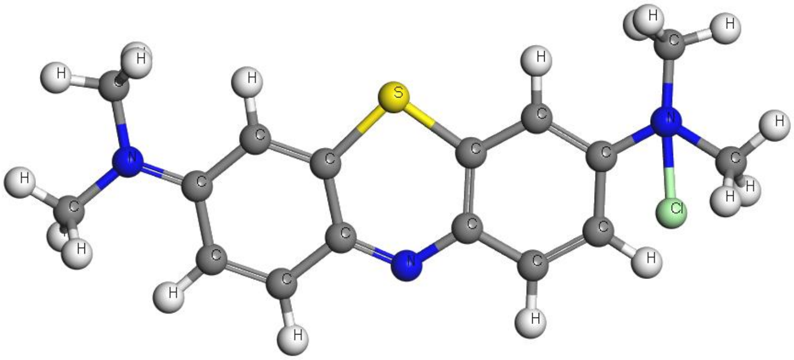

Figure I.1: The structure of MB dye molecule.

According to the literature [3,4], MB has large benefits as well as harmful effects, part of which are summarized in Figure I.2.

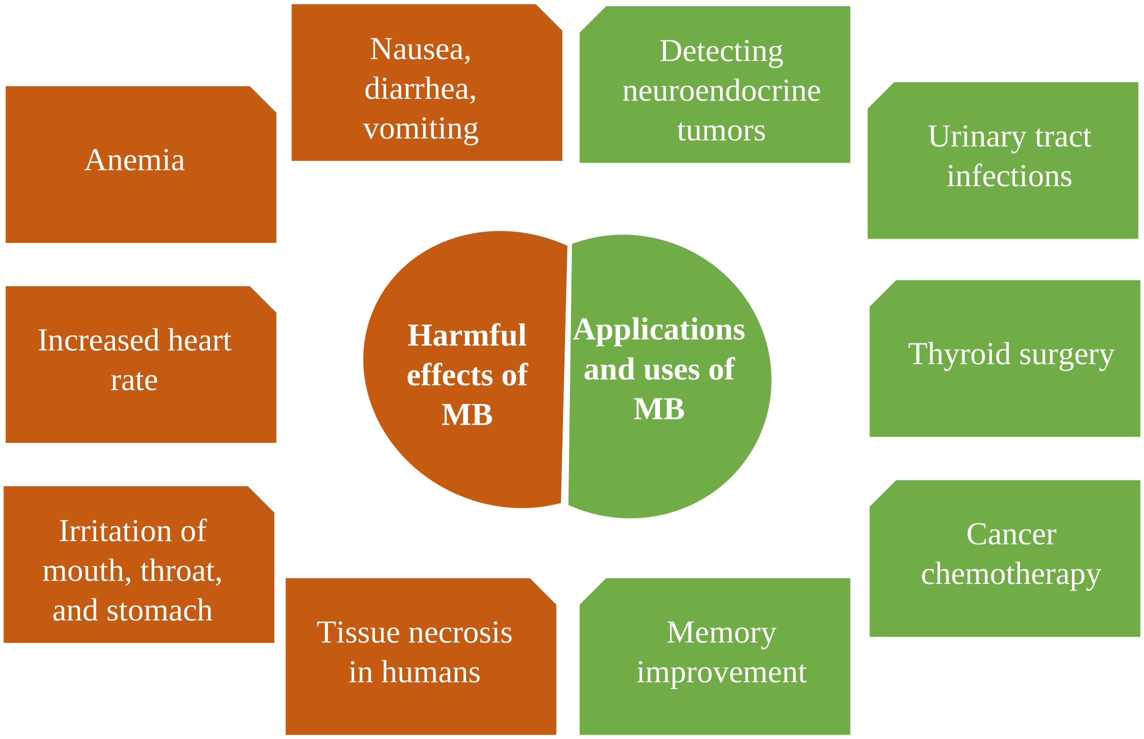

Figure I.2: Application and uses and the harmful effects of the MB dye.

I.2 Wastewater Treatment Methods

Water has always represented an important natural resource of the earth and an essential tool for the existence of all living beings. According to the World Health Organization, in 2020, 2 billion people used drinking water sources containing fecal contaminants [6]. To solve this problem, the application of a suitable water treatment program is needed. Wastewater treatment methods are divided into two main groups physical/chemical and biological methods [7]. Among the physicochemical processes, adsorption and photocatalysis are commonly used for wastewater treatments.

I.2.1 Adsorption

Adsorption is defined as the grouping together of molecules on the surface of an adsorbate i.e., liquid or solid, this grouping results from the attractive forces between molecules [8]. The adsorption process, which typically occurs at solid-solid, gas-solid, or liquid-solid interfaces, results in the formation of an adsorbent layer on the surface of the adsorbate, as shown in Figure I.3. Adsorption is known as one of the most effective methods for removing organic pollutants due to its high efficiency, simple operation and low costs. However, adsorption is still restricted by the limited capacity of the adsorbate, slow kinetics, and high energy requirement for adsorbent regeneration.

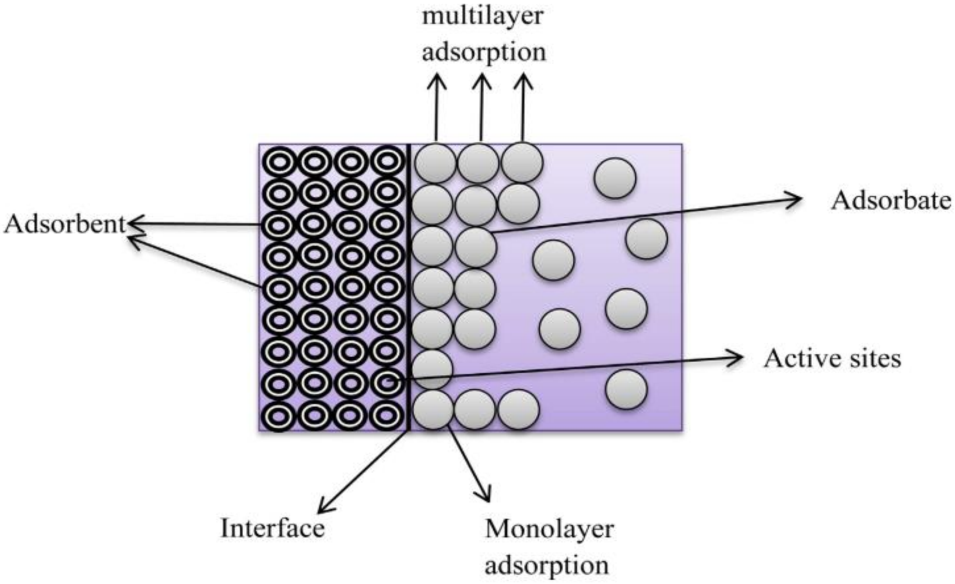

Figure I.3: Schematic diagram of the adsorption process [9].

Adsorption could be affected by different factors including [8]:

- The physicochemical characteristics of the adsorbate, such as; the chemical composition, molecule size and its molecular polarity as well as the concentration in the liquid phase and pH of the solution.
- The physicochemical characteristics of the adsorbent, such as; the specific surface area and pore size as well as the chemical composition.
- The contact time between the adsorbate and adsorbent in addition to the temperature of the system.

I.2.1.1 Types of Adsorption

Based on the nature of interaction forces between the adsorbent and adsorbate, adsorption is classified into two types; physisorption and chemisorption.

- **Physisorption**

In such a physisorption process, the adsorbate molecules are attached to the adsorbent surface by relatively weak interactions, such as Van Der Walls forces, polarity and dipole-dipole interactions [10,11]. Because of these weak forces, physisorption is a multilayer reversible process that does not require activation energy with a fast adsorption and desorption rate. The number of layers is proportional to the concentration of the adsorbed species, i.e., higher concentrations lead to the formation of more layers [8]. Physisorption is a physical treatment method that does not change the target substance's, adsorbate, chemical structure and biological composition [12]. The endpoint of a physisorption process is reached when the concentration of the adsorbing species reaches its saturation value [11].

- **Chemisorption**

Chemisorption is a monolayer process that occurs when strong interactions, due to the exchange of electrons, occur between the adsorbate and the solid surface, these interactions could be either covalent or ionic bond formation. When the adsorbate and solution come into contact, the surface of the adsorbent attracts the dye molecules via the functional groups as a result of the attractive forces at the solid surface [8]. Chemisorbed spices are irreversibly bound to the surface of the adsorbent [12]. The final stage of the chemisorption process is reached when all the active sites on the solid surface are occupied by the adsorbed molecules [12]. This process requires high activation energy above 10 kcal/mol which usually results in the formation of a chemical bond with a strength of 25-100kcal [12].

I.2.2 Photocatalysis

Photocatalysis is defined as a photochemical reaction that takes place under light irradiation in the presence of a photocatalyst [13]. The word photocatalysis is a combination of two words "photo" and "catalysis", where the word "photo" refers to light while "catalysis" is the process of enhancing the rate of a chemical reaction in the presence of a catalyst [13]. The distinction between conventional catalysis and photocatalysis stands in the usage of light instead of heat for the activation of the catalyst. Photocatalysis employs semiconductors as a photocatalyst which are typically made of metal oxides/ sulfides, oxysulfides or oxynitrides [14].

I.2.2.1 Photocatalysis Mechanism

The photocatalytic process is manifested when the photocatalyst absorbs light of an energy greater than or equal to its band gap E_g which results in the excitation of the electron (e^-) from the valence band (VB) to the conduction band (CB) leaving a hole (h^+) behind. It is noted that these electron-hole pairs may recombine due to the electrostatic force of interaction, resulting in the conversion of the input energy into heat or radiation light [15] as equation (I.1) shows. These charge carriers are then transferred into the surface of the photocatalyst, which in turn in the case of aqueous solutions, react with oxygen, water and hydroxyl molecules to generate highly active radicals as explained by equations (I.2-I.4) [16]. These free radicals are capable of reducing or oxidizing the pollutant adsorbed on the surface of the photocatalyst.

$$h^+ + e^- \rightarrow heat \tag{I.1}$$

$$e^- + O_2 \rightarrow O_2^{\bullet -} \tag{I.2}$$

$$h^+ + H_2O \ \rightarrow OH^{\bullet} + h^+ \tag{I.3}$$

$$h^+ + OH^- \rightarrow OH^{\bullet} \tag{I.4}$$

As it is known, the holes h^+ contain high oxidation power with redox potential ranging from +1 to +3.5V [16] can directly attack the pollutant into reactive intermediates. The hole photocatalytic process is depicted in Figure I.4.

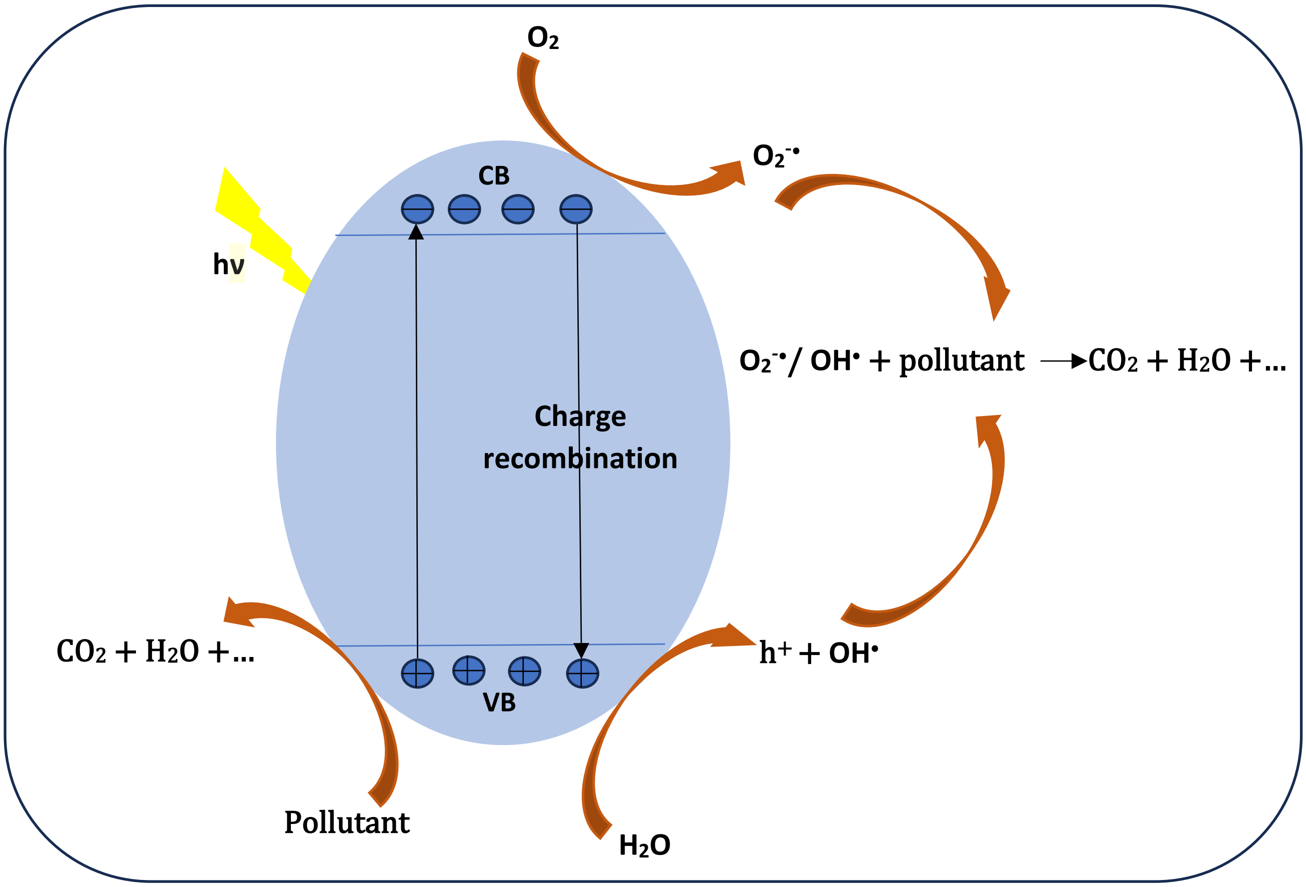

Figure I.4: Schematic illustration of the principle of photocatalysis.

Photocatalysis could be affected by several factors such as [17]:

- The photocatalytic material: the particle size and shape, morphology, specific surface area, band gap and the presence of impurities are the main critical factors that may influence the process.
- The wavelength and intensity of the source light.
- The pH and temperature of the solution.
- The initial quantity and concentration of the dye.

I.2.2.2 Types of Photocatalysis

Photocatalysis can be homogeneous or heterogeneous, depending on the type of catalyst and reacting spices. In a homogeneous photocatalytic process, the reactants exist in the same phase as the photocatalyst where the distribution is uniform [18]. For this type of reaction, each catalytic entity acts as an active site, the reason that makes this process more active and selective compared to heterogenous photocatalysis [17]. However, the synthesis of a homogeneous photocatalytic system is normally costly because of the complexity of the structure, where the separation is difficult, and the utilization of expensive precursors.

In heterogeneous photocatalysis, the reactants and photocatalysts exist in different phases [18]. This type of photocatalytic reaction is the most frequently used due to the easy separation of the photocatalyst material after application.

I.3 Perovskite Type Oxide

Perovskites are mixed oxides with the typical chemical formula of ABO_3, where site A is occupied by a rare earth or alkaline-earth element and B by a transition metal. Three-dimensional perovskites consist of network corner sharing BO_6 octahedral, where the A atoms with a coordination number of 12 are characterized by a large radius compared to the 6-coordinated B atoms [19]. The beauty of this structure is manifested by the presence of a large number of cations with different oxidation numbers, ex: $A^{1+}B^{5+}O_3$, $A^{2+}B^{4+}O_3$ and $A^{3+}B^{3+}O_3$ [19,20]. Controlling the A- and -B cations either by changing the size of the cation or the oxidation state, the properties of the ABO_3 perovskite can be varied to fit the desired application [21].

Ideal perovskites are known to show a cubic structure Pm-3m as shown in Figure I.5.a where the A cation is situated on the vertex, the B occupies the body center position and the O is at the face center [20]. The extended network structure connected by the corner-shared octahedra BO_6 is illustrated in Figure I.5.b, it can be seen that the B-O-B angles are 180°. The ionic radii have the following relationship:

$$r_A + r_O = \sqrt{2}(r_B + r_O) \tag{I.1}$$

Where r_A, r_B and r_O are the ionic radii of the A, B and O atoms, respectively.

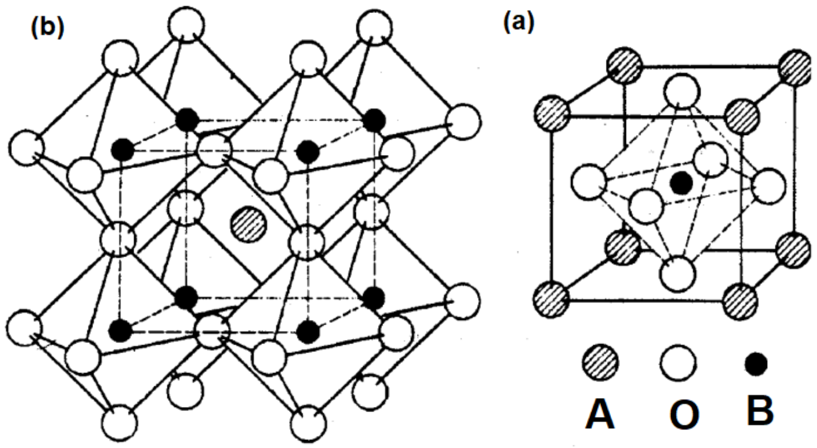

Figure I.5: (a) The ideal perovskite structure and (b) the extended network structure connected by the corner-sharing BO_6 octahedra [22].

I.3.1 Structure Distortion

The stability of a perovskite structure is of primary importance. The Goldschmidt tolerance factor (t) is a geometrical consideration that helps to predict the preferentially formed perovskite structure, where $t = \frac{r_A + r_B}{\sqrt{2}(r_B + r_O)}$ [23]. Generally, for most of the perovskite structures, t ranges between 0.78 and 1.05 [24]. When $t = 1$, the ideal cubic perovskite geometry is expected. For a perovskite structure, the distortion and stability are dependent on the tolerance factor, a small defect in the lattice can decrease the symmetry of the system [23,25]. Therefore, cubic, orthorhombic, rhombohedral, monoclinic, triclinic and tetragonal perovskites are all known [26]. For large size A atoms and small size B ones, $t > 1$ where the B atoms have a larger room to move [27], otherwise, for $t < 1$, the B cations are found to have a large size.

The deviation from an ideal cubic structure into a distorted structure could be attributed to one of the following three mechanisms: ion displacement, distortion of the octahedra or tilting of the octahedra [28]. The first two mechanisms are caused by the electronic instabilities of the cations where the Jahn-Teller and ferroelectric displacements are examples of octahedral distortions. The third type of distortion may be found in an orthorhombic or rhombohedral compound [26], tilting of the octahedron occurs when the ionic radii of the A cations are too small to occupy fully the available volume. Table I.1 represents the different distortions in an ABO_3 perovskite structure.

Table I.1: Different distortions in an ABO_3 perovskite structure [26,29].

ABO_3 perovskite	r_A (Å)	r_B (Å)	r_O(Å)	Tolerance factor (t)	Distortion
$SrTiO_3$	1.44	0.605	1.40	1.001	No distortion (cubic)
$BaTiO_3$	1.61	0.605	1.40	1.061	The ferroelectric displacement of titanium (tetragonal)
$CaTiO_3$	1.34	0.605	1.40	0.966	Tilt in BO_6 octahedra (the coordination of the A-site changed from 12 to 8) (Orthorhombic)
$GdFeO_3$	1.053	0.63	1.40	0.8	Jahn-Teller distortion (orthorhombic)

I.3.2 $LaFeO_3$ Perovskite

I.3.2.1 Crystal Structure

$LaFeO_3$ perovskite crystallizes in an orthorhombic structure (*Pnma* space group, 62), where the Fe^{3+} cations are octahedral coordinated (FeO_6) with a tolerance factor that ranges between 0.906 and 0.9546 [30,31]. The structure of $LaFeO_3$ changes from orthorhombic *Pnma* to the rhombohedral *R3c* structure at 1280 K depending on thermal history and stoichiometry with a further phase transition from rhombohedral to cubic *Pm3m* at 2140 K [32]. Table I.2 presents the atomic positions while Figure I.6 illustrates the $LaFeO_3$ cell. As Figure I.6 depicts, the octahedron in the orthorhombic $LaFeO_3$ structure is irregular exhibiting two dissimilar oxygen sites O1 and O2.

Table I.2: Atomic coordinates of the $LaFeO_3$ orthorhombic structure [33].

Element	Site	Wyckoff position	x	y	z
La	**La1**	4c	0.02493	0.25	0.99615
Fe	**Fe1**	4b	0	0	0.5
O	**O1**	4c	0.48288	0.25	0.08164
	O2	8d	0.28163	0.46142	0.71871

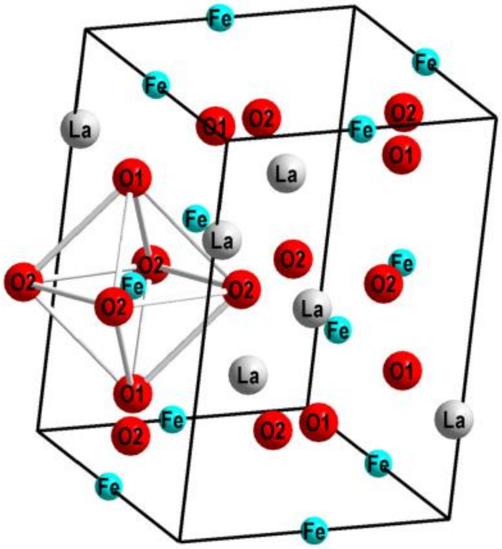

Figure I.6: Crystal structure of the $LaFeO_3$ unit cell showing the tilting of the octahedra [34].

In such a perovskite cubic structure, the A atom is surrounded by 12 equidistance oxygen atoms while the B atom is situated at the center of an undistorted oxygen octahedron. Which is not the case in an orthorhombic one. The 12 A-O distances vary over a large range [35]. The La-O bond lengths vary from 2.585 to 2.793 Å according to Capone et *al*. [36], while the average Fe-O and O-O bond lengths are 2.006 and 2.837 Å, respectively [35]. The Fe-O-Fe bond angle is 156° which is considered to be the largest bond angle in the ferrite perovskite systems [37]. The Fe-O-Fe bond in an ideal perovskite is 180° [34], thus, a significant distortion in the FeO_6 octahedra could be seen with b/a=1.002 Å, this distortion could be attributed to the displaced oxygen and rare earth ions from their cubic position [38,39].

I.3.2.2 Magnetic and Electronic Structure

Perovskite compounds exist in different magnetic ordering (ferromagnetic, A, C and G antiferromagnetic spin ordering) as illustrated in Figure I.7. In $LaFeO_3$ perovskite, the 3d electron configuration influences the magnetic ordering of transition metal ions through super-exchange interactions between Fe^{3+} ions in the Fe^{3+}–O^{2-}–Fe^{3+} bond angle [40]. These interactions cause lattice distortions due to the strong local electric field generated [33]. Consequently, this leads to the formation of an antiferromagnetic arrangement within the material.

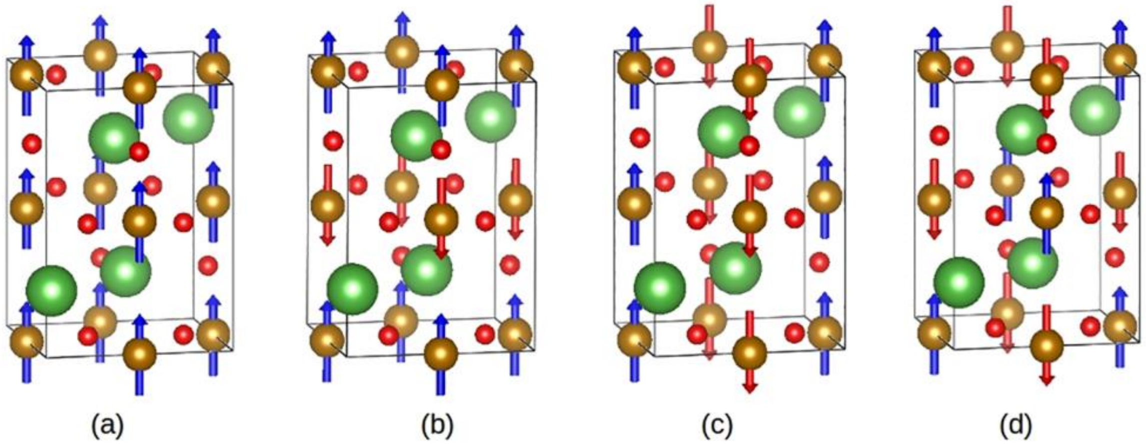

Figure I.7: (a) Ferromagnetic (FM), antiferromagnetic (AFM) (b) A- type, (c) C- type, (d) G-type configurations [41].

$LaFeO_3$ is known as a G-type antiferromagnetic perovskite with a Néel temperature of 735 K which is considered to be the highest in the orthoferrites system [8,14] as shown in Figure I.8. The Fe magnetic moment is 4.23 μ_B with a total magnetic moment of 0 μ_B[42]. As depicted in Figure I.8, the strong antiferromagnetic coupling interactions are influenced by differences in A-site occupancies, resulting from decreasing the ionic radii, unit cell's contractions, deviation of the Fe-O-Fe bond angels and increased covalent bond character with rising the atomic number along the lanthanide series [43]. Therefore, as the A-O bond becomes more covalent, the Fe-O bonds tend to be more ionic. Thus, with increasing the ionicity of the Fe-O bonds, the Fe^{3+}–O^{2-}–Fe^{3+} super-exchange interactions decrease which leads to low T_N temperatures [43].

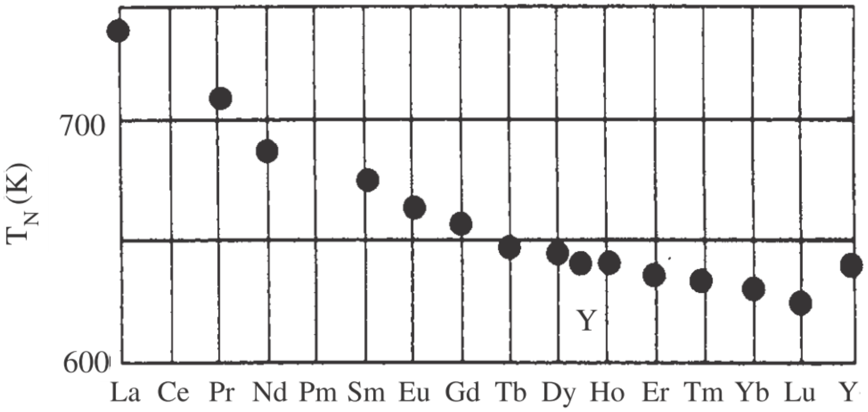

Figure I.8: Variation of the Néel temperature T_N with rare earth ion R for $RFeO_3$ [44].

The $LaFeO_3$ perovskite shows a *p*-type semiconducting behavior with a band gap of 2.1 - 2.6 eV [45,46]. Figure I.9 depicts the electronic band structure and partial density of state (PDOS) of the $LaFeO_3$ which exhibits a spin degenerate structure where both spin up and spin downs are equal. The valence energy states are mainly contributed by the Fe -*3d* and O -*2p* electrons.

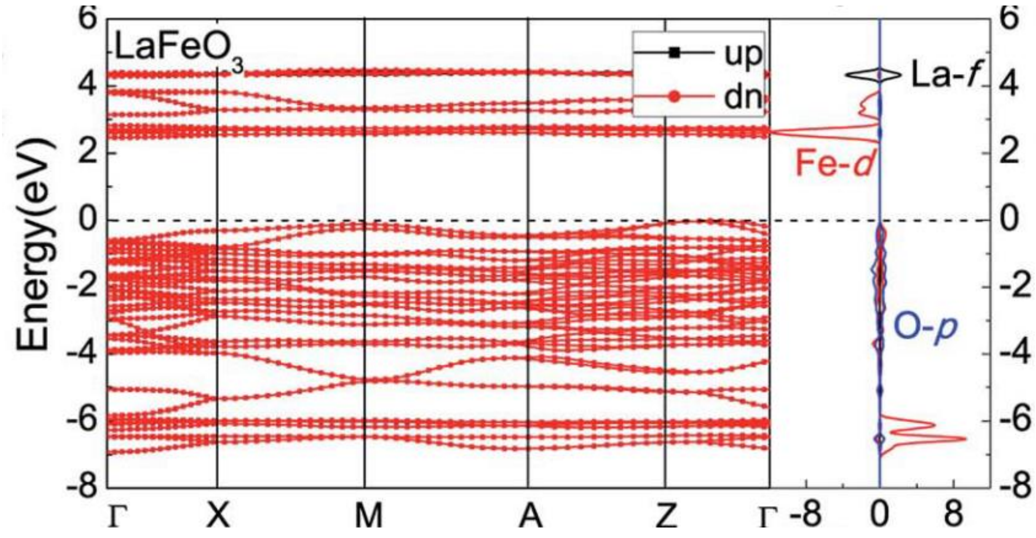

Figure I.9: The band structures and partial density of states for $LaFeO_3$ [47].

I.3.2.3 Surface Studies on $LaFeO_3$

An important consideration during an adsorption study is its surface structure. The most commonly studied surfaces are (010), (111) and (110) as illustrated in Figure I.10.

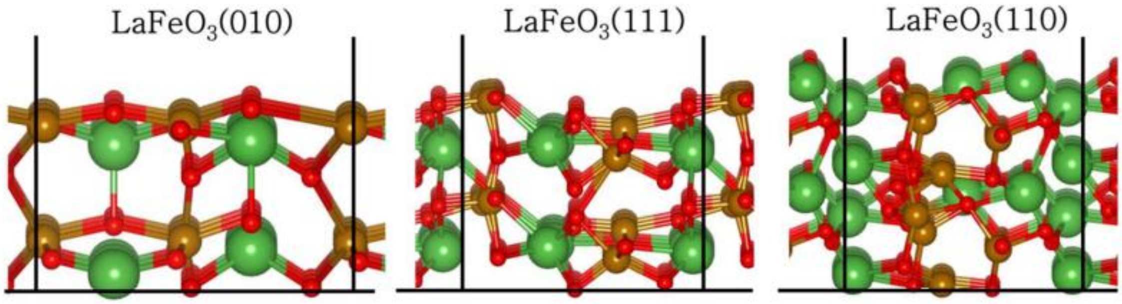

Figure I.10: The optimized structures of the (010), (111) and (110) surfaces of $LaFeO_3$ in side views [48].

The (010) $LaFeO_3$ surface is characterized by two termination surface types, Fe-O terminated surface and La-O terminated surface. Mudi Wu et al. studied the properties of these two different terminations [49]. The results show that the formation energy of the surface oxygen vacancies of the Fe-O bond terminations is lower than that of the La-O bond termination. Which means that the Fe-O bonds are weaker and easier to break. Therefore, it is easier to form more oxygen vacancies which makes the $LaFeO_3$ much more suitable for catalytic applications.

Most studies about the (010) surface indicate the reduction of the surface band gap compared to the bulk one, which means that the transfer of electrons becomes more easier on the surface [50, 51]. Lihui Sun et al. show that the adsorption of NO on (010) $LaFeO_3$ surface is more favorable on the Fe site with Fe-NO configuration which was the same case for the adsorption of O_2 where the adsorbed O_2 on Fe ion was more stable than that on La or O sites [52,53]. In another paper, Lihui Sun et al. [54] also demonstrate that the adsorption of the CO molecule favors the Fe-O configuration where the CO here acts as a donor and loses energy for the (010) surface. They concluded that the Fe-d and CO-*p* orbits dominate the bond of the adsorbed CO and Fe site. Xing Liu et al. [50] show that the O ion surface dominates the adsorption of methanol on the same surface, where the adsorbed H_{O-H} on O ion is the most stable configuration regarding the other H atoms and carbon atoms configuration.

Haonan Pei et al. [55] studied the removal of mercury using the $LaFeO_3$, La_2O_3 and Fe_2O_3 metal oxides through experimental and theoretical investigations. They demonstrate that the $LaFeO_3$ shows the best removal efficiency. (121), (101) and (010) $LaFeO_3$ surfaces were chosen for the mercury removal study. The highest adsorption energy was achieved for the (101) surface. The results indicate that Hg-O and Hg-Fe bonding is covalent. This makes the $LaFeO_3$ perovskite a promising adsorbent for Hg removal.

References

[1] Shen, H., Xue, T., Wang, Y., Cao, G., Lu, Y., & Fang, G. (2016). Photocatalytic property of perovskite LaFeO3 synthesized by sol-gel process and vacuum microwave calcination. *Materials Research Bulletin*, *84*, 15-24. DOI: 10.1016/j.materresbull.2016.07.024.

[2] Sadasivuni, K. K., Deshmukh, K., Pasha, S. K., & Kovarik, T. (Eds.). (2021). *MXenes and their Composites: Synthesis, Properties and Potential Applications*. Elsevier. DOI: 10.1016/B978-0-12-823361-0.00024-1.

[3] Khan, I., Khan, I., Usman, M., Imran, M., & Saeed, K. (2020). Nanoclay-mediated photocatalytic activity enhancement of copper oxide nanoparticles for enhanced methyl orange photodegradation. *Journal of Materials Science: Materials in Electronics*, *31*, 8971-8985. DOI: 10.1007/s10854-020-03431-6.

[4] Salleh, M. A. M., Mahmoud, D. K., Karim, W. A. W. A., & Idris, A. (2011). Cationic and anionic dye adsorption by agricultural solid wastes: a comprehensive review. *Desalination*, *280*(1-3), 1-13. DOI: 10.1016/j.desal.2011.07.019.

[5] Robinson, T., McMullan, G., Marchant, R., & Nigam, P. (2001). Remediation of dyes in textile effluent: a critical review on current treatment technologies with a proposed alternative. *Bioresource technology*, *77*(3), 247-255. DOI: 10.1016/S0960-8524(00)00080-8.

[6] World Health Organization. (2002). *Guidelines for drinking-water quality*. World Health Organization. DOI: 10.1016/B978-0-12-823361-0.00024-1.

[7] Saravanan, A., Kumar, P. S., Jeevanantham, S., Karishma, S., Tajsabreen, B., Yaashikaa, P. R., & Reshma, B. (2021). Effective water/wastewater treatment methodologies for toxic pollutants removal: Processes and applications towards sustainable development. *Chemosphere*, *280,* 130595. DOI: 10.1016/j.chemosphere.2021.130595.

[8] Cheremisinoff, P. N. (2019). *Handbook of water and wastewater treatment technology*. Routledge. DOI: 10.1201/9780203752494.

[9] Soliman, N. K., & Moustafa, A. F. (2020). Industrial solid waste for heavy metals adsorption features and challenges; a review. *Journal of Materials Research and Technology*, *9*(5), 10235-10253. DOI: 10.1016/j.jmrt.2020.07.045.

[10] Kausar, A., Iqbal, M., Javed, A., Aftab, K., Bhatti, H. N., & Nouren, S. (2018). Dyes adsorption using clay and modified clay: A review. *Journal of Molecular Liquids*, *256*, 395-407. DOI: 10.1016/j.molliq.2018.02.034.

[11] Ballantine Jr, D. S., White, R. M., Martin, S. J., Ricco, A. J., Zellers, E. T., Frye, G. C., & Wohltjen, H. (1996). *Acoustic wave sensors: theory, design and physico-chemical applications*. Elsevier.

[12] Afolalu, S. A., Ikumapayi, O. M., Ogedengbe, T. S., Kazeem, R. A., & Ogundipe, A. T. (2022). Waste pollution, wastewater and effluent treatment methods–an overview. *Materials Today: Proceedings*, *62*, 3282-3288. DOI: 10.1016/j.matpr.2022.04.231.

[13] Naliwajko, P., & Strunk, J. (2021). Photocatalysis–the heterogeneous catalysis perspective. *Heterogeneous Photocatalysis: From Fundamentals to Applications in Energy Conversion and Depollution*, 101-126. DOI: 10.1002/9783527815296.ch5.

[14] Suib, S. L. (Ed.). (2013). *New and future developments in catalysis: Batteries, Hydrogen Storage and Fuel Cells*. Newnes. DOI: 10.1016/C2010-0-68687-1.

[15] Pan, L., & Zhu, G. (Eds.). (2016). *Perovskite materials: synthesis, characterisation, properties, and applications*. BoD–Books on Demand. DOI: 10.5772/60469.

[16] Khan, I., Saeed, K., Zekker, I., Zhang, B., Hendi, A. H., Ahmad, A., ... & Khan, I. (2022). Review on methylene blue: Its properties, uses, toxicity and photodegradation. *Water*, *14*(2), 242. DOI: 10.3390/w14020242.

[17] Nayak, A. K., & Sahu, N. K. (Eds.). (2021). *Nanostructured materials for visible light photocatalysis*. Elsevier. DOI: 10.1016/C2019-0-05075-3.

[18] Xu, Y. J., & Colmenares, J. C. (2016). Heterogeneous Photocatalysis: From Fundamentals to Green Applications. DOI: 10.1007/978-3-662-48719-8.

[19] Ishihara, T. (Ed.). (2009). *Perovskite oxide for solid oxide fuel cells*. Springer Science & Business Media. DOI: 10.1007/978-0-387-77708-5.

[20] Ahmad, K., & Raza, W. (Eds.). (2022). *Perovskite Materials for Energy and Environmental Applications*. John Wiley & Sons. DOI: 10.1002/9781119763376.

[21] Kilner, J. A., & Burriel, M. (2014). Materials for intermediate-temperature solid-oxide fuel cells. *Annual Review of Materials Research*, *44*(1), 365-393. DOI: 10.1146/annurev-matsci-070813-113426.

[22] Goodenough, J. B., & Zhou, J. S. (1998). Localized to itinerant electronic transitions in transition-metal oxides with the perovskite structure. *Chemistry of materials*, *10*(10), 2980-2993. DOI: 10.1021/cm970818u.

[23] Cheng, Z., & Lin, J. (2010). Layered organic–inorganic hybrid perovskites: structure, optical properties, film preparation, patterning and templating engineering. *CrystEngComm*, *12*(10), 2646-2662. DOI: 10.1039/C001929A.

[24] Wolfram, T., & Ellialtioglu, S. (2006). *Electronic and optical properties of d-band perovskites*. Cambridge University Press. DOI: 10.1017/CBO9780511541292.

[25] Ma, Y., Wang, S., Zheng, L., Lu, Z., Zhang, D., Bian, Z., ... & Xiao, L. (2014). Recent research developments of perovskite solar cells. *Chinese Journal of Chemistry*, *32*(10), 957-963. DOI: 10.1002/cjoc.201400435

[26] Woodward, P. M. (1997). Octahedral tilting in perovskites. I. Geometrical considerations. *Acta Crystallographica Section B: Structural Science*, *53*(1), 32-43. DOI: 10.1107/S0108768196010713.

[27] Sebastian, M. T. (2010). *Dielectric materials for wireless communication*. Elsevier. DOI: 10.1016/B978-0-08-045330-9.X0001-5.

[28] Behara, S., & Thomas, T. (2020). Stability and amphotericity analysis in rhombohedral ABO3 perovskites. *Materialia*, *13*, 100819. DOI: 10.1016/j.mtla.2020.100819.

[29] Yang, Y., Guo, P., Xie, Y., Lu, Y., & Luo, Y. (2021). Electronic and magnetic properties of LaRuO3 and LaFeO3: Orbital order and canted antiferromagnetism. *Computational Materials Science*, *200*, 110839. DOI: 10.1016/j.commatsci.2021.110839.

[30] Liu, Q., You, Z., Zeng, S. J., & Guo, H. (2016). Infrared properties of Mg-doped LaFeO 3 prepared by sol–gel method. *Journal of Sol-Gel Science and Technology*, *80*, 860-866. DOI: 10.1007/s10971-016-4141-x.

[31] Selbach, S. M., Tolchard, J. R., Fossdal, A., & Grande, T. (2012). Non-linear thermal evolution of the crystal structure and phase transitions of LaFeO3 investigated by high temperature X-ray diffraction. *Journal of Solid State Chemistry*, *196*, 249-254. DOI:10.1016/j.jssc.2012.06.023

[32] Jia, T., Zeng, Z., Lin, H. Q., Duan, Y., & Ohodnicki, P. (2017). First-principles study on the electronic, optical and thermodynamic properties of ABO 3 (A= La, Sr, B= Fe, Co) perovskites. *Rsc Advances*, *7*(62), 38798-38804. DOI: 10.1039/C7RA06542F.

[33] Abbas, Y. M., Mansour, A. B., Ali, S. E., & Ibrahim, A. H. (2018). Synthesis, structure and magnetic characterization of orthoferrite LaFeO3 nanoparticles. *Journal: Journal of Advances in Physics*, *14*(3). DOI: 10.24297/JAP.V14I3.7693.

[34] Singh, S., & Singh, D. (2017). Synthesis of LaFeO 3 nanopowders by glycine–nitrate process without using any solvent: effect of temperature. *Monatshefte für Chemie-Chemical Monthly*, *148*, 879-886. DOI: 10.1007/s00706-016-1818-3

[35] Marezio, M., & Dernier, P. D. (1971). The bond lengths in LaFeO3. *Materials Research Bulletin*, *6*(1), 23-29. DOI: 10.1016/0025-5408(71)90155-3.

[36] Capone, Mara, et al. "Subtle structural changes in LaFeO3 at high pressure." *physica status solidi (b)* 258.2 (2021): 2000413. DOI: 10.1002/pssb.202000413.

[37] Lin, Q., Lin, J., Yang, X., He, Y., Wang, L., & Dong, J. (2019). The effects of Mg2+ and Ba2+ dopants on the microstructure and magnetic properties of doubly-doped LaFeO3 perovskite catalytic nanocrystals. *Ceramics International*, *45*(3), 3333-3340. DOI: 10.1016/j.ceramint.2019.09.246.

[38] Peterlin-Neumaier, T., & Steichele, E. (1986). Antiferromagnetic structure of LaFeO3 from high resolution tof neutron diffraction. *Journal of magnetism and magnetic materials*, *59*(3-4), 351-356. DOI: 10.1016/0304-8853(86)90431-2.

[39] Fajriyani, F., & Triyono, D. (2020, July). Study of La (Fe, Zn) O3 on the structural properties prepared by sol-gel method. In *IOP Conference Series: Materials Science and Engineering* (Vol. 902, No. 1, p. 012033). IOP Publishing. DOI: 10.1088/1757-899X/902/1/012033.

[40] Phokha, S., Pinitsoontorn, S., Maensiri, S., & Rujirawat, S. (2014). Structure, optical and magnetic properties of LaFeO 3 nanoparticles prepared by polymerized complex method. *Journal of sol-gel science and technology*, *71*, 333-341. DOI: 10.1007/s10971-014-3383-8.

[41] Yassine, R., Abdallah, A. M., Awad, R., & Bitar, Z. (2022). Structural, optical and magnetic properties of (x) NiO/(1-x) CdFe2O4 nanocomposites. *Physica B: Condensed Matter*, *624*, 413444. DOI: 10.1016/j.physb.2021.413444.

[42] Zhou, Y., Lü, Z., Li, J., Xu, S., Xu, D., & Wei, B. (2021). The electronic properties and structural stability of LaFeO3 oxide by niobium doping: A density functional theory study. *International Journal of Hydrogen Energy*, *46*(13), 9193-9198. DOI: 10.1016/j.ijhydene.2020.12.202.

[43] Goodenough, J. B. (2004). Electronic and ionic transport properties and other physical aspects of perovskites. *Reports on Progress in Physics*, *67*(11), 1915. DOI: 10.1088/0034-4885/67/11/R01.

[44] Navrotsky, A., & Weidner, D. J. (1989). Perovskite: a structure of great interest to geophysics and materials science. *Geophysical monograph series*, *45*. DOI: 10.1029/GM045.

[45] Khalil, K. M., Mahmoud, A. H., & Khairy, M. (2022). Formation and textural characterization of size-controlled LaFeO3 perovskite nanoparticles for efficient photocatalytic degradation of organic pollutants. *Advanced Powder Technology*, *33*(1), 103429. DOI: 10.1016/j.apt.2022.103429.

[46] Phan, T. T. N., Nikoloski, A. N., Bahri, P. A., & Li, D. (2018). Optimizing photocatalytic performance of hydrothermally synthesized LaFeO3 by tuning material properties and operating conditions. *Journal of environmental chemical engineering*, *6*(1), 1209-1218. DOI: 10.1039/C8RA07073C.

[47] Jia, T., Zeng, Z., Lin, H. Q., Duan, Y., & Ohodnicki, P. (2017). First-principles study on the electronic, optical and thermodynamic properties of ABO 3 (A= La, Sr, B= Fe, Co) perovskites. *Rsc Advances*, *7*(62), 38798-38804. DOI: 10.1039/C7RA06542F.

[58] Boateng, I. W., Tia, R., Adei, E., Dzade, N. Y., Catlow, C. R. A., & De Leeuw, N. H. (2017). A DFT+ U investigation of hydrogen adsorption on the LaFeO 3 (010) surface. *Physical Chemistry Chemical Physics*, *19*(10), 7399-7409. DOI: 10.1039/C6CP08698E.

[49] Wu, M., Ma, S., Chen, S., & Xiang, W. (2020). Fe–O terminated LaFeO3 perovskite oxide surface for low temperature toluene oxidation. *Journal of Cleaner Production*, *277*, 123224. DOI: 10.1016/j.jclepro.2020.123224.

[50] Liu, X., Cheng, B., Hu, J., & Qin, H. (2013). Theoretical calculation of ethanol molecule adsorption on LaFeO3 (0 1 0) surface. *Computational materials science*, *68*, 90-94. DOI: 10.1016/j.commatsci.2012.09.019.

[51] Liu, X., Cheng, B., Hu, J., & Qin, H. (2012). Study on adsorption of O2 on LaFe1− xMgxO3 (0 1 0) surface by density function theory calculation. *Applied surface science*, *258*(22), 8678-8682. DOI: 10.1016/j.apsusc.2012.05.073.

[52] Sun, L., Hu, J., Gao, F., Zhang, Y., & Qin, H. (2011). First-principle study of NO adsorption on the LaFeO3 (0 1 0) surface. *Physica B: Condensed Matter*, *406*(21), 4105-4108. DOI: 10.1016/j.physb.2011.07.060.

[53] Liu, X., Hu, J., Cheng, B., Qin, H., Zhao, M., & Yang, C. (2009). First-principles study of O2 adsorption on the LaFeO3 (0 1 0) surface. *Sensors and Actuators B: Chemical*, *139*(2), 520-526. DOI: 10.1016/j.snb.2009.03.052.

[54] Sun, L., Hu, J., Qin, H., Zhao, M., & Fan, K. (2011). Influences of Ca doping and oxygen vacancy upon adsorption of CO on the LaFeO3 (010) surface: a first-principles study. *The Journal of Physical Chemistry C*, *115*(13), 5593-5598. DOI: 10.1021/jp107038z.

[55] Pei, H., Li, X., Song, Y., Zhang, M., Wang, D., Wu, J., ... & Jia, T. (2022). LaFeO3 perovskite nanoparticles for efficient capture of elemental mercury from coal-fired flue gas. *Fuel*, *309*, 122134. DOI: 10.1016/j.fuel.2021.122134.

Chapter II:
Experimental Techniques

The present chapter is divided into two sections, the first one is dedicated to the sol-gel process. The basic reactions during a sol-gel process are described in detail followed by a comprehensive explanation of the factors influencing this process. The second section deals with the different techniques used to study the structure, thermal stability, surface morphology and optical properties of the synthesized materials including X-ray diffraction spectroscopy (XRD), thermogravimetric analysis (TGA), Scanning electron microscopy (SEM), Brunauer-Emmett-Teller analysis (BET), Fourier transform infrared spectroscopy (FTIR) and UV-Visible spectroscopy (UV-Vis).

II.1 Sol-Gel Process

Sol-gel process, also known as inorganic polymerization [1], was first introduced by Ebelman in 1845 [2]. It is a process commonly used for synthesizing highly homogenous nanomaterials which consists of forming a new phase through hydrolysis and condensation of a liquid [2]. Basically, at the macroscopic scale, it seems to be a very simple process which is not the case at the microscopic scale involving three states of matter: liquid, colloid and solid [1]. Sol-gel technique provides various advantages starting from controlling the microstructure and surface properties during synthesizing and low temperature of reaction to the high purity level and better homogeneity of the final product [3,4].

I.1.1 Basic Reactions in the Sol-Gel Process

Sol-gel process is illustrated in Figure II.1. Three steps could be distinguished during a so-gel process:

i. Preparation of the sol: a sol is defined as a colloidal suspension made of nanometer-sized solid particles (~1-1000nm) in a liquid solution [1]. Within these nanometer-sized particles, only Van Der Waals attractions and surface charges exist (such as Coulomb repulsive forces), and gravitational forces are neglected [1]. During this process, sol is prepared through hydrolysis of an alkoxide or inorganic salt precursors. Generally, water (aqueous sol-gel method) or organic solvents (nonaqueous sol-gel method) are used as solvent mediums. In the case of water medium and alkoxide precursor [-M-OR] the hydrolysis step is given with the following formula [5];

$$-M-OR+H_2O \rightarrow -MOH+ROH \tag{II.1}$$

Where M and R represent the metal and alkyl groups, respectively.

ii. Gelation of the sol: at this stage, the sol is solidified through polycondensation into a gel-forming 3D network structure. This chemical reaction occurs at the surface of the colloids where the hydrolyzed molecules are linked together with metal-oxo-metal or metal-hydroxy-metal bonds [1,2]. The condensation reaction is represented by the following equations [5];

Olation $$-M-OH+R-OM- \rightarrow -M-OH-M- \; +H_2O \tag{II.2}$$

Oxalation $$-M-OH+R-OM- \rightarrow -M-O-M- \; +ROH \tag{II.3}$$

Two competitive mechanisms are involved during polycondensation. Olation occurs when a hydroxyl bridge (-OH-) is formed between two metal centers while oxalation is manifested in the case of an oxo bridge (-O-) [1].

iii. Removal of the solvent: the gel here is transformed into a dense solid through the drying process leading to a liquid phase removal [2]. The drying process depends on the required network of the gel. At ambient pressure and low temperatures, xerogel is obtained, otherwise (i.e., drying under supercritical conditions) aerogel with low density and high surface area is obtained [2,6].

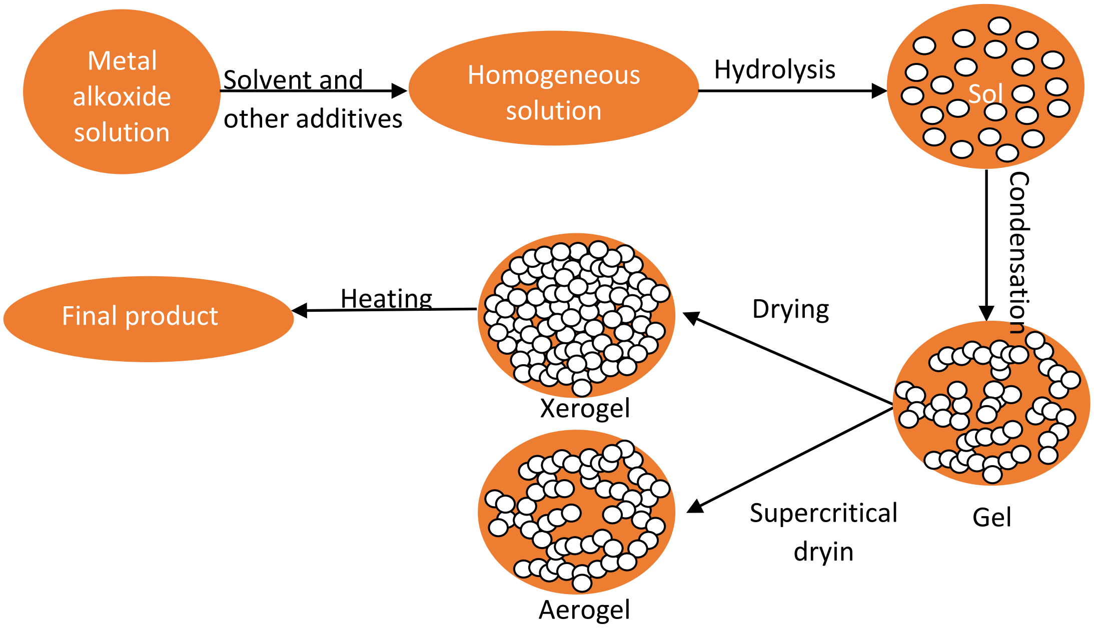

Figure II.1: Schematic diagram representing the various steps of the Sol-gel process.

Generally, sol-gel reactions require a thermal treatment of the M-OH surface group through calcination [3,6].

I.1.2 Factors Influencing Sol-Gel Process

During each step of the sol-gel method, multiple physical and chemical factors could affect the final structure of the synthesized product. These factors are the following:

i. Nature of the solvent: the addition of the solvent during a sol-gel process is necessary either to enhance mixing or to increase the contact between the molecules [7-9]. Forming of highly condensed spices could be obtained by lowering the energy of the intermediates during the condensation reaction which could be gained with the aid of the solvent [9]. Therefore, the type and polarity of the solvent can affect the sol-gel process.

ii. The amount and rate of water: adjusting the water ratio is a key to control hydrolysis. Generally, a large content of water leads to a faster hydrolysis reaction [8,10]. In some cases, the condensation of a small amount of the metal precursor occurs before the complete hydrolysis, which leads to the formation of particles with bigger sizes [10].

iii. Role of the precursor: generally, metal alkoxides or metal inorganic salts represent the most commonly used classes of precursors. Depending on the used precursor, hydrolysis and condensation reaction characteristics can vary [10]. The choice of the precursor depends on several things, including the electron-donating property where several studies demonstrated that faster hydrolysis occurs when the organic group is more electron donor which helps in decreasing the metal-oxygen (M-O) bond strength [10]. Besides, the electronegativity between the metal and oxygen could affect the M-O bond which has a direct influence on the hydrolysis and condensation steps. Moreover, the viscosity and volatility of the precursor can affect the suitability of the precursor for a sol-gel process [7].

iv. Reaction temperature: it is well known that raising the temperature increases the mobility of atoms, molecules, and particles, resulting in increasing the kinetic energy of the system. Therefore, increasing the temperature can shorten the formation time of the gel but on another hand, it could lead to higher agglomeration of the particles [10]. Several works reported that raising the temperature from room temperature to sub-ambient temperatures results in higher particle sizes and short gel time [10].

v. The pH: the pH of the solution has a clear effect on the hydrolysis and condensation processes. The hydrolysis rate is found to be higher under acidic conditions compared to the condensation rate resulting in weakly branched gel formation. Otherwise, under basic conditions, a highly branched gel is formed where the condensation rate is found to be greater than the hydrolysis rate [5].

II.2 Characterization Techniques

During the realization of this work, several characterization techniques were used:

- X-ray Diffraction spectroscopy (XRD)
- Thermogravimetric Analysis (TGA)

- Scanning Electron Microscopy (SEM)
- Brunauer-Emmett-Teller analysis (BET)
- Fourier Transform Infrared spectroscopy (FTIR)
- UV-Visible spectroscopy (UV-Vis)

II.2.1 X-ray Diffraction (XRD)

XRD analysis is one of the most widely used techniques for the determination of the crystalline phase and structural properties (lattice parameters, crystallite size, residual stress, texture, and peak density…) [11]. This non-destructive technique consists of generating an X-ray beam using a cathode ray tube (T), filtering it to produce monochromatic radiation and then concentrating it in a single ray which will be then directed to the crystal (C), as illustrated in Figure II.2., the diffracted rays from the crystal are then collected through the detector (D). Generally, the θ - 2θ geometry is adapted, where θ and 2θ represents the rotation angle of the sample and detector, respectively.

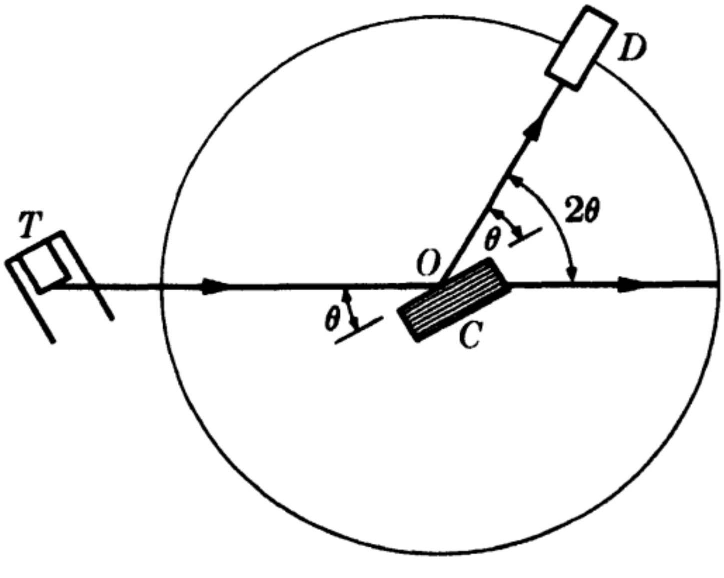

Figure II.2: A simplified Schematic diagram of an X-ray diffractometer system [12].

As illustrated in Figure II.3, the diffracted rays are detected only if the constructive diffractions satisfy the Bragg low [11]:

$$n\lambda = 2d_{hkl}sin\theta \quad \text{(II.4)}$$

Where n is the order of diffraction (1,2,3, …), λ(nm) is the wavelength of the incident X-ray, d_{hkl}(nm) submits to the distance between the diffracting plans and θ is the angle between the incident beam and the crystal.

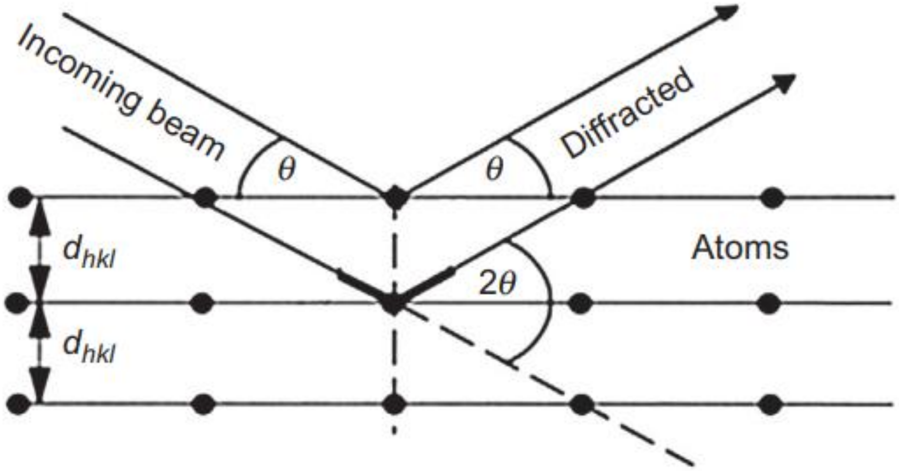

Figure II.3: Illustration of the Bragg law diffraction by crystal planes [13].

The calculation of the crystallite size (D) and lattice strain (ε), could be obtained using the Debye-Scherrer and Williamson-Hall equations, respectively [12]:

$$D = \frac{0.9\,\lambda}{\beta cos\theta} \qquad \text{(II.5)}$$

$$\varepsilon = \frac{\beta}{4tan\theta} \qquad \text{(II.6)}$$

Where β refers to the full width at half-maximum (FWHM) of the peak.

In this work, structural characterizations were carried out using the X-ray diffraction (XRD) technique for 2θ between 10 and 80° via an X'Pert diffractometer (PANalytical) using Cu $K_{\alpha 1}$ radiation (λ = 1.54 Å) operating at tube voltage and current of 40 kV and 40 mA, respectively. This characterization was carried out at the Nuclear Research Center of Birine in Djelfa.

II.2.2 Thermogravimetric Analysis (TGA)

Thermogravimetric analysis (TGA) is considered to determine the thermal stability of such a compound by measuring its weight changes with temperature change under a controlled atmosphere such as argon (Ar) or nitrogen (N_2) to avoid any diverse reaction or oxidation [11].

During a TGA, several information could be obtained such as phase transition, moister and solvent loss, the decomposition of the biomass, pyrolysis and decarboxylation [14]. A typical TG instrument is illustrated in Figure II.4. The sample is placed on a pan inside a furnace and then heated under a controlled environment. Changes in the required properties are monitored by a transducer while the change of mass is restrained through a balance and the measurements are collected and displayed as TG curves where the mass/percent mass is plotted against temperature [14,15].

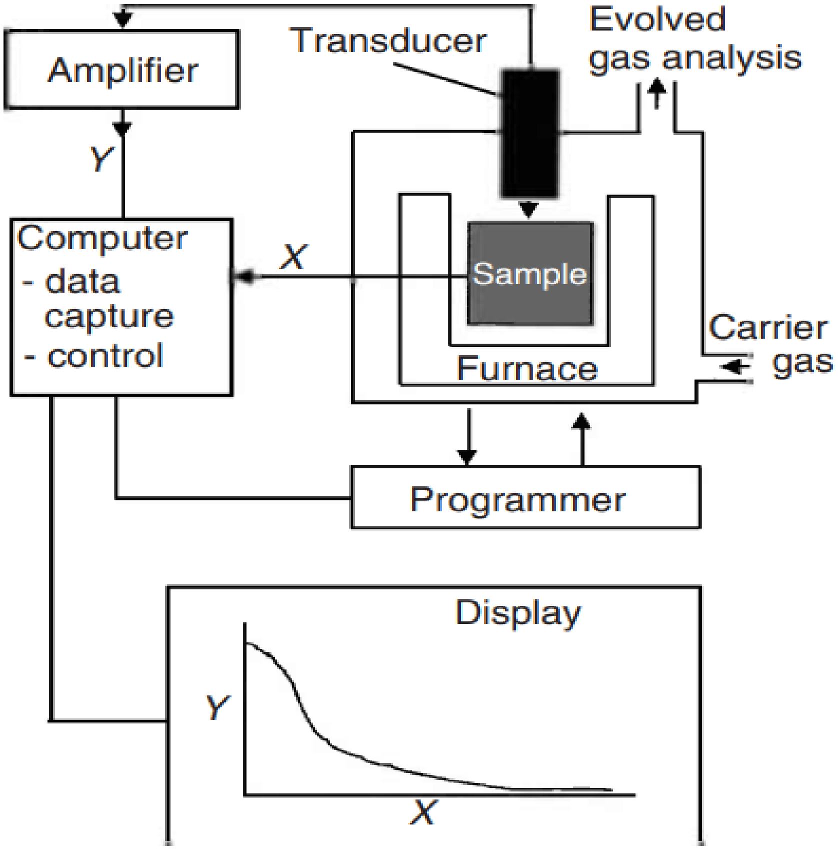

Figure II.4: Thermogravimetric instrument [15].

The first derivative of the thermogravimetric analysis (DTG) illustrates the ratio of the change in mass of the sample as a function of temperature. Typically, this method does not provide any additional information than those of TGA, otherwise, it provides information about the temperature at which the greatest mass loss occurs [15].

Thermogravimetric analysis (TGA) of the synthesized samples was performed using an SDT Q600 instrument at the Emergent Materials Research Unit (EMRU) at the university of Ferhat

Abbas Sétif-1. A powder mass of 10 mg was placed onto a platinum pan and heated up from ambient temperature to 1000°C at a scan rate of 10°C/min under nitrogen purge (100 mL/min).

II.2.3 Scanning Electron Microscopy (SEM)

Scanning electron microscopy is a characterization technique used for the visualization and imaging of the morphology and micro or nanostructure of nanomaterials. An SEM instrument consists of three major parts: an electron column, a sample chamber, and an electronic control system as shown in Figure II.5.

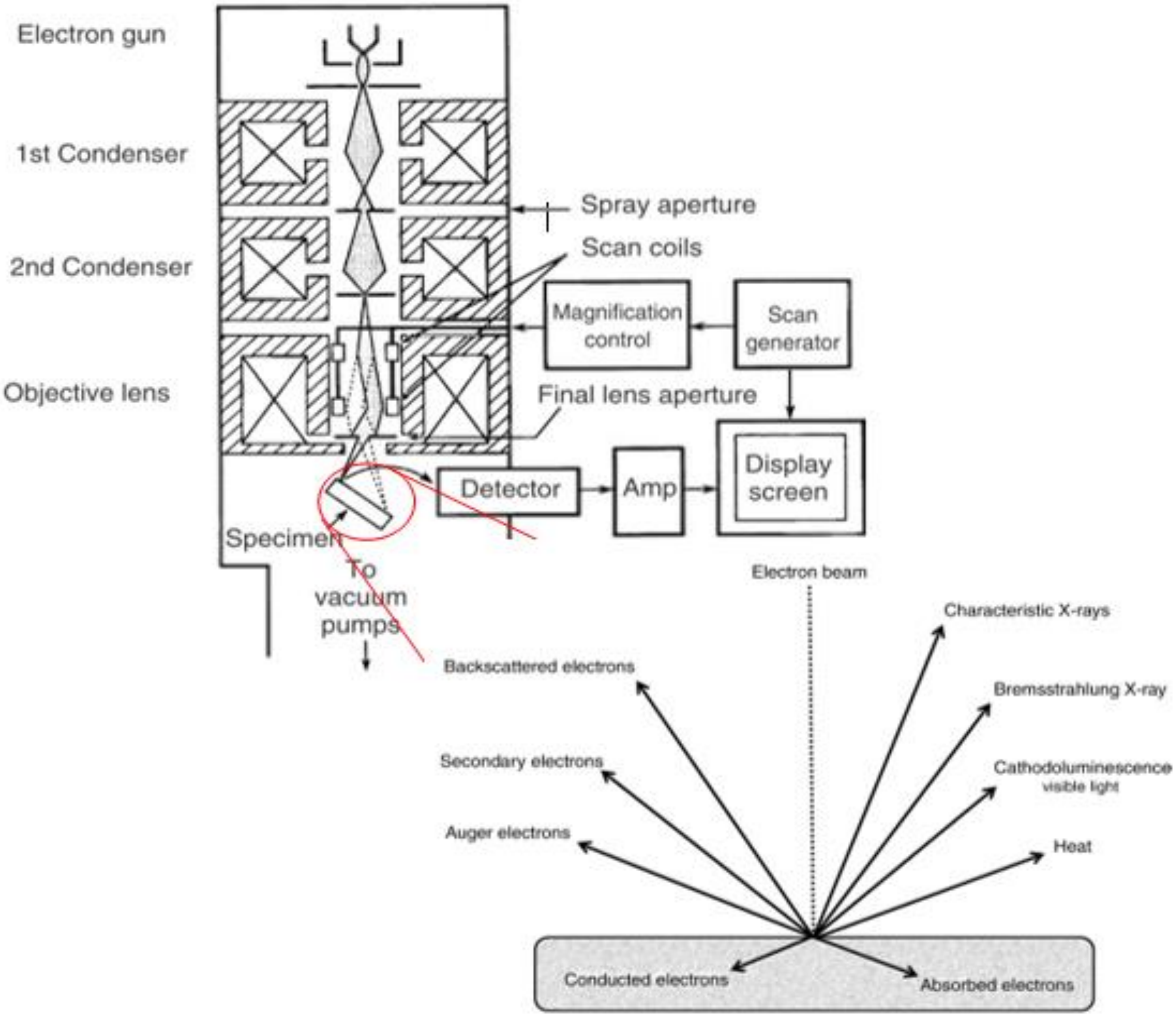

Figure II.5: Schematic representation of a scanning electron microscope [15].

Starting from the electron gun, an emitted electron beam with an accelerated voltage of 0.1-30 keV is focused and shaped through a series of electromagnetic lenses on the surface of the sample that was maintained under vacuum to prevent the electrons from being scattered or absorbed by air. During the interaction of the electron beam with the electrons of the sample's surface, electrons are released in the form of the signal as illustrated in the in-set image in Figure II.5 [16]. Depending on the desired type of information, different modes of SEM exist according to the type of electrons detected.

Energy dispersive X-ray spectroscopy (EDX, EDS, or XEDS) helps to study the elemental composition besides the chemical characterization of a sample. Qualitative and quantitative analyses could be performed through EDX analysis where the elements present in the sample and their relative abundance are determined. An electron beam with an energy of 10-20 keV bombards the surface of the sample, therefore, X-rays are emitted and examined through an energy-dispersive detector [11]. Generally, EDS could be coupled with scanning or transmission electron microscope (SEM / TEM).

The powder morphologies were viewed with a scanning electron microscope (SEM), model "JEOL JSM-7001F", at an accelerating voltage of 15 kV. A few mg of each sample were deposited on a conductive carbon wafer far away from the electron gun with 8 mm. The elemental composition was analyzed by an energy-dispersive X-ray (EDX) spectrometer associated with the SEM instrument, at an accelerating voltage of 15 kV. This characterization was performed at the Dosing, Analysis and Characterization with High Resolution (DAC-hr) laboratory at the University of Ferhat Abbas Sétif-1.

II.2.4 Brunauer-Emmett-Teller Analysis (BET)

The Brunauer- Emmett-Teller method is widely used to calculate the specific surface area of solid samples. During a BET analysis, the surface area is determined through the determination of the physical adsorption, at the boiling temperature, of a non-polar gas (generally N_2) under a high vacuum environment [17,18]. By performing the adsorption at different pressures and using the BET equation (Eq II.7), it is possible to determine the amount of adsorbed gas required to form a monolayer [18]

$$\frac{P/P_0}{V(1-P/P_0)} = \frac{1}{V_m c_{BET}} + \frac{P/P_0(c_{BET}-1)}{V_m c_{BET}} \tag{II.7}$$

With: P/P_0: relative pressure

V: volume of the adsorbed gas molecules

V_m: the monolayer volume

C_{BET}: the BET constant

By plotting the $\frac{P/P_0}{V(1-P/P_0)}$ against P/P_0, the volume of the monolayer is determined by Eq (II.8), through the determination of the slope $(\frac{(c_{BET}-1)}{V_m c_{BET}})$ and intercept $(\frac{1}{V_m c_{BET}})$ of the resulting linear plot [19].

$$V_m = \frac{1}{slope+intercept} \tag{II.8}$$

The specific surface area (S_{BET}) could be then calculated using Eq (II.9) [19]

$$S_{BET} = \frac{V_m N_A a_m}{v_m m_s} \tag{II.9}$$

Where N_A is the Avogadro number, a_m and v_m represent the cross-section area and the molar volume of one nitrogen molecule, respectively, while m_s is the mass of the substrate or adsorbent.

In this work, the Brunauer- Emmett-Teller (BET) surface area measurements were carried out by N_2 physisorption using an ASAP micrometrics 2010, where the samples were outgassed at 300 °C. this characterization was performed at the Nuclear Research of Draria (CRND) in Algiers.

II.2.5 Fourier Transform Infrared spectroscopy (FTIR)

The Fourier transform infrared spectroscopy is considered one of the most widely used vibrational spectroscopy. This technique is based on the identification of the chemical bonds present in the studied molecule where each vibration produces a characteristic vibrational peak that corresponds to a specific functional group [20,21]. In such a typical FTIR instrument as shown in Figure II.6, an infrared IR split beam is emitted from the light source and passed through a series of moving mirrors in order to generate a light interference between the split beams by changing the optical path length [15]. The process is continuous until all wavelengths are generated. When the IR radiations pass through the sample, sample molecules absorb light with specific wavelengths according to their chemical properties due to the interaction between those radiations and the vibration of the chemical bonds of the sample [15,17]. Those selected radiations are then detected and generated as an electrical signal to give the final spectrum where the intensity of the vibrations given as a percentage (%) of transmittance is plotted against the frequency of light.

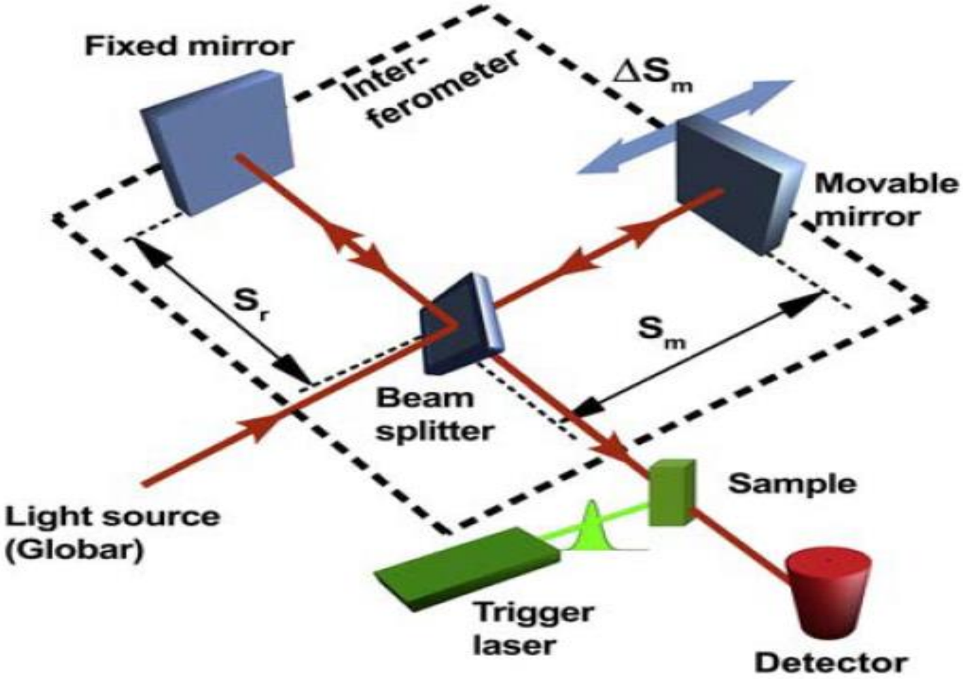

Figure II.6: Schematic illustration of the Fourier transform infrared spectrometer [11].

The PerkinElmer Spectrum™3 FT-IR spectrometer at the faculty of science, university of Ferhat Abbas Sétif-1 was used to record the transmission spectra of the powders to identify the functional groups present. The FTIR spectroscopy analysis was performed at room temperature in the range of 4000-400 cm^{-1} using KBr pellets.

II.2.6 UV-Visible Spectroscopy

Ultraviolet-visible spectroscopy (UV-Vis) represents one of the characterization techniques that study the optical properties through the absorption, reflection, or transmission of UV-visible light by the molecule. It is considered a non-destructive technique that provides quantitative information about different types of organic, inorganic and biological materials [22]. Figure II.7 illustrates a representative schema of a UV-Vis spectrometer, a light beam in a wavelength range of 200 – 800 nm passed through a monochromator that splits the light into individual wavelengths which are then passed by the sample, the passed light is detected and recorded. During the interaction of the emitted light and the molecules, absorption of light, electrons from occupied molecular orbitals are excited to unoccupied or singularly occupied molecular orbitals [4,22]. These transitions with a characteristics peak give information about the different spices present in the molecules, the number of spices, and their orientation [23,24]. Therefore, different molecules absorb different radiation with a specific wavelength giving rise to different UV-Vis spectra.

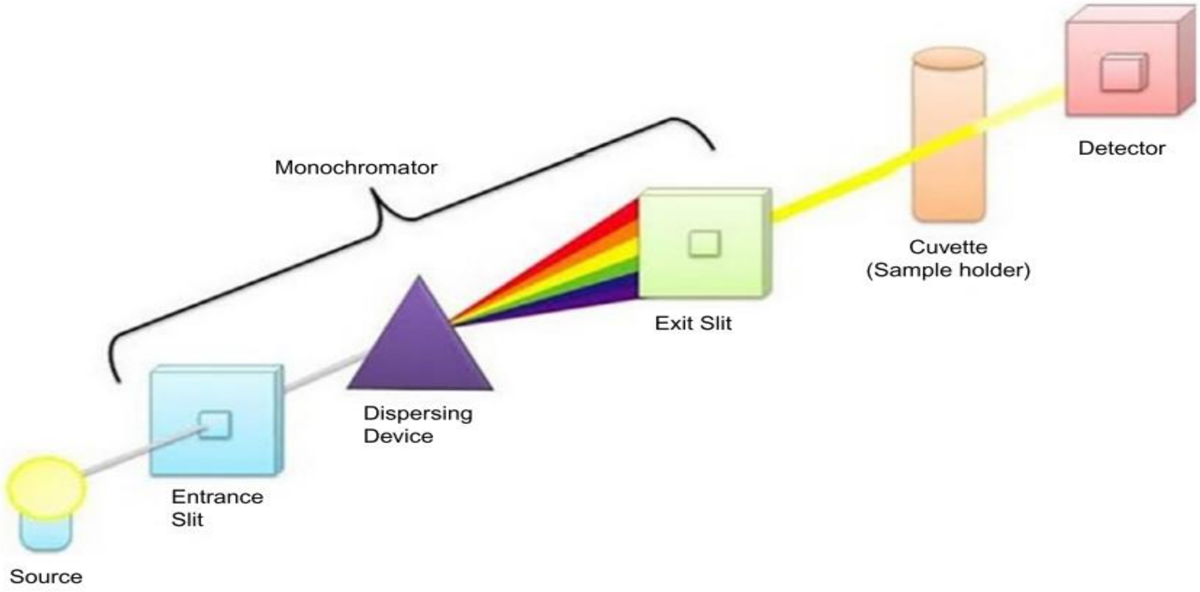

Figure II.7: Schema of a UV-Vis spectrometer [22].

The absorbance of a sample is known to be proportional to the intensity of the light beam, where an increase in the electronic beam guarantees an increase in the absorbance. The amount of absorbed light (A) is related to the elemental concentration (C in mol L^{-1}) of the sample in solution given by the Bee-Lambert law:

$$A = \varepsilon l C \qquad \text{(II.10)}$$

Where ε and l represent the molar absorption coefficient (L mol^{-1} cm^{-1}) and the path length (cm), respectively.

The band gap energy E_g of the molecules could be also estimated through the UV-Vis analysis, by using the Tauc formula given by:

$$\alpha h\upsilon = A(h\upsilon - E_g)^n \tag{II.11}$$

Where α represents the absorption coefficient, hυ corresponds to the incident photon energy while n depends on the transition process (1/2 allowed direct, 1/2 allowed forbidden, 2/3 forbidden direct and 1/3 forbidden indirect transitions) [24]. The extrapolation of the $(\alpha h\upsilon)^{1/n}$ versus hυ plot along the straight-line portion at y=0 reveals the value of the energy band gap of the material.

In the present work, the absorption spectra measurements of $LaFeO_3$ powders were carried out on a UviLine 9400 spectrophotometer in a wavelength range of 300-800 nm. This characterization was performed at the faculty of science, university of Ferhat Abbas Sétif-1.

References

[1] Corriu, R., & Anh, N. T. (2009). *Molecular chemistry of sol-gel derived nanomaterials*. John Wiley & Sons. DOI: 10.1002/9780470742778.

[2] Nayak, A. K., & Sahu, N. K. (Eds.). (2021). *Nanostructured materials for visible light photocatalysis*. Elsevier. DOI: 10.1016/C2019-0-05075-3.

[3] D'Arienzo, M., Scotti, R., Di Credico, B., & Redaelli, M. (2017). Synthesis and characterization of morphology-controlled TiO2 nanocrystals: opportunities and challenges for their application in photocatalytic materials. *Studies in Surface Science and Catalysis*, *177*, 477-540. DOI: 10.1016/B978-0-12-805090-3.00013-9.

[4] Ahmed, W., & Jackson, M. J. (2014). *Emerging nanotechnologies for manufacturing*. William Andrew. DOI: 10.1016/C2013-0-13991-8.

[5] Lončarević, D., & Čupić, Ž. (2019). The perspective of using nanocatalysts in the environmental requirements and energy needs of industry. In *Industrial Applications of Nanomaterials* (pp. 91-122). Elsevier. DOI: 10.1016/B978-0-12-815749-7.00004-9.

[6] Zaleska-Medynska, A. (2018). *Metal oxide-based photocatalysis: fundamentals and prospects for application*. Elsevier. DOI: 10.1016/C2016-0-01872-7

[7] Danks, A. E., Hall, S. R., & Schnepp, Z. J. M. H. (2016). The evolution of 'sol–gel'chemistry as a technique for materials synthesis. *Materials Horizons*, *3*(2), 91-112. DOI: 10.1039/C5MH00260E

[8] Cividanes, L. S., Campos, T. M., Rodrigues, L. A., Brunelli, D. D., & Thim, G. P. (2010). Review of mullite synthesis routes by sol–gel method. *Journal of Sol-Gel Science and Technology*, *55*(1), 111-125. DOI: 10.1007/S10971-010-2222-9.

[9] Hebda, E., & Pielichowski, K. (2018). Polyurethane/POSS hybrid materials. *Polymer/POSS Nanocomposites and Hybrid Materials: Preparation, Properties, Applications*, 167-204. DOI: 10.1007/978-3-030-02327-0_5

[10] Borlaf, M., & Moreno, R. (2021). Colloidal sol-gel: A powerful low-temperature aqueous synthesis route of nanosized powders and suspensions. *Open Ceramics*, *8*, 100200. DOI: 10.1016/j.oceram.2021.100200

[11] Ghasemi, A. (2022). *Magnetic ferrites and related nanocomposites*. Elsevier. DOI: 10.1016/B978-0-12-824014-4.00001-2

[12] Cullity, B. D., & Smoluchowski, R. (1957). Elements of X-ray Diffraction. *Physics Today*, *10*(3), 50-50. DOI: 10.1063/1.3060306

[13] Epp, J. (2016). X-ray diffraction (XRD) techniques for materials characterization. In *Materials characterization using nondestructive evaluation (NDE) methods* (pp. 81-124). Woodhead Publishing. DOI: 10.1016/B978-0-08-100040-3.00004-3

[14] Basu, P. (2018). *Biomass gasification, pyrolysis and torrefaction: practical design and theory*. Academic press. DOI: 10.1016/B978-0-12-813603-3.00001-2.

[15] Leng, Y. (2013). *Materials characterization: introduction to microscopic and spectroscopic methods*. John Wiley & Sons. DOI: 10.1002/9781118653767.

[16] de Oliveira Jr, O., Marystela, F. L., de Lima Leite, F., & Da Róz, A. L. (Eds.). (2017). *Nanocharacterization techniques*. William Andrew.

[17] Wypych, F., & de Freitas, R. A. (Eds.). (2022). *Clay Minerals and Synthetic Analogous as Emulsifiers of Pickering Emulsions*. Elsevier. DOI: 10.1016/B978-0-323-91858-9.00001-2.

[18] Worsfold, P., Townshend, A., Poole, C. F., & Miró, M. (2019). *Encyclopedia of analytical science*. Elsevier.

[19] Naderi, M. (2015). Surface area: brunauer–emmett–teller (BET). In *Progress in filtration and separation* (pp. 585-608). Academic Press. DOI: 10.1016/B978-0-12-384746-1.00014-8.

[20] Otitoju, T. A., Okoye, P. U., Chen, G., Li, Y., Okoye, M. O., & Li, S. (2020). Advanced ceramic components: Materials, fabrication, and applications. *Journal of industrial and engineering chemistry*, *85,* 34-65. DOI: 10.1016/j.jiec.2020.02.002.

[21] Kumar, P. S. (2020). *Modern treatment strategies for marine pollution*. Elsevier. DOI: 10.1016/B978-0-12-822279-9.00001-2.

[22] Oluwafemi, O. S., Parani, S., & Lebepe, T. C. (2021). *Ternary quantum dots: Synthesis, properties, and applications*. Woodhead Publishing. DOI: 10.1016/B978-0-12-818303-8.09992-5.

[23] Wandelt, K. (2018). *Encyclopedia of interfacial chemistry: surface science and electrochemistry*. Elsevier. DOI: 10.1016/B978-0-12-809739-7.00001-2.

[24] Thambiratnam, K., Reduan, S. A., Tiu, Z. C., & Ahmad, H. (2020). Application of two-dimensional materials in fiber laser systems. In *Nano-Optics* (pp. 227-264). Elsevier. DOI: 10.1016/B978-0-12-818392-2.00009-3.

Chapter III:
Theoretical Methods

Modeling methods based on quantum theory represent a powerful tool for studying materials and their properties. The complication of the many-body systems is replaced by an equivalent single electrons problem. Density functional theory is then successfully introduced to the determination of different material properties. The first section of this chapter is an introduction to basic molecular quantum mechanics. Then, a presentation of the density functional theory (DFT) is provided starting from the Hohenberg-Kohn theorem to the plane-wave pseudopotential approach. The last section is dedicated to the DFT codes used during the realization of this thesis.

III.1 The Schrödinger Equation

The description of any quantum system (atom, molecules…) passed through the resolution of the Schrödinger equation [1]:

$$\hat{\mathrm{H}}\Psi_i(\boldsymbol{r}_1,\boldsymbol{r}_2,\dots\boldsymbol{r}_N,\boldsymbol{R}_1,\boldsymbol{R}_2,\dots\boldsymbol{R}_M)=E\Psi_i(\boldsymbol{r}_1,\boldsymbol{r}_2,\dots\boldsymbol{r}_N,\boldsymbol{R}_1,\boldsymbol{R}_2,\dots\boldsymbol{R}_M), \qquad \text{(III.1)}$$

where $\hat{\mathrm{H}}$ represents the Hamiltonian operator, Ψ (**r**, **R**) is the wavefunction, **r** and **R** are the electron and nuclei positions respectively and E is the total energy.

The Hamiltonian operator for a system of N electron and M nuclei of charge Z is given as [1]:

$$\hat{\mathrm{H}}=-\frac{1}{2}\sum_{i=1}^{N}\nabla_i^2-\frac{1}{2}\sum_{k=1}^{M}\frac{1}{M_k}\nabla_k^2-\sum_{i=1}^{N}\sum_{k=1}^{M}\frac{Z_k}{r_{ik}}+\sum_{i=1}^{N}\sum_{j>i}^{N}\frac{1}{r_{ij}}+\sum_{k=1}^{M}\sum_{l>k}^{M}\frac{Z_kZ_l}{R_{kl}} \qquad \text{(III.2)}$$

$$\hat{\mathrm{H}}=\hat{T}_e+\hat{T}_n+\hat{V}_{e-n}+\hat{V}_{e-e}+\hat{V}_{n-n} \qquad \text{(III.3)}$$

with $\hat{T}_e$ and $\hat{T}_n$ are the electrons and nucleus kinetic energy operators, respectively. $\hat{V}_{e-e}$, $\hat{V}_{n-n}$ and $\hat{V}_{e-n}$ are the electron-electron, nucleus-nucleus and electron-nucleus interaction operators, respectively.

The prediction of the structure and properties of such material requires the resolution of the Schrodinger equation which is quite complicated, thus, the introduction of some approximations is necessary. The first approximation adopted is known as the Born-Oppenheimer approximation [1].

This approximation raises on the assumption that the nuclei move much slower than the electron which is justified by the much greater velocities behavior of the electrons compared to the heavier nuclei [2]. Therefore, the nuclei are considered to be fixed with zero kinetic energy and a constant nucleus-nucleus potential energy [2]

$$\Psi_{system}=\Psi_{electrons}(\boldsymbol{r},\boldsymbol{R})\Psi_{nuclei}(\boldsymbol{R}) \qquad \text{(III.4)}$$

Thus, the Hamiltonian is then written as [1]:

$$\hat{\mathrm{H}}=-\frac{1}{2}\sum_{i=1}^{N}\nabla_i^2-\sum_{i=1}^{N}\sum_{k=1}^{M}\frac{Z_k}{r_{ik}}+\sum_{i=1}^{N}\sum_{j>i}^{N}\frac{1}{r_{ij}}=\hat{T}+\hat{V}_{ext}+\hat{V}_{e-e} \qquad \text{(III.5)}$$

with $\hat{V}_{ext}=-\sum_{i=1}^{N}\sum_{k=1}^{M}\frac{Z_k}{r_{ik}}$ represents the interaction with the external potential.

The Schrödinger equation (III.3) still cannot be solved for complicated systems even with fixed positions of the nuclei, for this reason, additional approximations are necessary.

III.2 Hartree-Fock Approximation

Hartree-Fock theory consists of considering that there is no interaction between the electrons of the system, i.e. the movement of the electron is considered uncorrelated [3]. Thus, the wavefunction Ψ is approximated with a product of all N electrons wavefunctions [4],

$$\Psi(\boldsymbol{x}_1, \boldsymbol{x}_2, \dots, \boldsymbol{x}_3) = \psi_1(\boldsymbol{x})\psi_2(\boldsymbol{x}) \dots \psi_N(\boldsymbol{x}) \tag{III.6}$$

However, taking the electron spin into account by the separation of electrons that have the same spin, each wavefunction is replaced with a spin-orbital function φ_i, therefore, introducing the anti-symmetry principle [5]. Fock illustrates the multi-electronic wavefunction as a determinant of single-particle states called the Slater determinant [6]:

$$\psi_{HF}(\boldsymbol{x}_1, \boldsymbol{x}_2 \dots \boldsymbol{x}_N) = \frac{1}{\sqrt{N!}} \begin{vmatrix} \varphi_1(\boldsymbol{x}_1) & \dots & \varphi_1(x_N) \\ \dots & \dots & \dots \\ \varphi_N(\boldsymbol{x}_1) & \dots & \varphi_N(\boldsymbol{x}_N) \end{vmatrix} \tag{III.6}$$

with $\varphi(\boldsymbol{x}_i) = \varphi(\boldsymbol{r}s) = \begin{pmatrix} \varphi_\uparrow(\boldsymbol{r}) \\ \varphi_\downarrow(\boldsymbol{r}) \end{pmatrix}$, $\varphi_\uparrow(\boldsymbol{r})$ spin up and $\varphi_\downarrow(\boldsymbol{r})$ spin down.

The introduction of the anti-symmetry of the wavefunction leads to the reduction of the Coulomb energy of the electronic system. Thus, the Hartree-Fock formulation introduces the exchange term into the Schrodinger equation which makes it solvable with an overestimation of the energy attributed to the neglection of the correlation term [7]. Accurate solutions require a flexible description of the wavefunction, consequently, an alternative method has been developed: Density Functional Theory DFT, taking into account the correlation between electrons.

III.3 Density Functional Theory

Instead of using wave functions of N electrons with 3N coordinates, density functional theory assumes that the electron density ρ(r), which is a function of 3 spatial coordinates (x, y, z), is the fundamental variable to describe the state of a system with N particles [8]. Therefore, a direct relationship between the total energy of the system and its density $E = E[\rho(\boldsymbol{r})]$ is constructed, where $\rho(\mathbf{r})$ is given by [8]

$$\rho(\boldsymbol{r}) = N \int \dots \int |\psi(\boldsymbol{x}_1, \boldsymbol{x}_2, \dots, \boldsymbol{x}_N|^2 ds_1 d\boldsymbol{x}_{\mathbf{1}} \dots d\boldsymbol{x}_N \tag{III.7}$$

$\rho(\mathbf{r})$ represents the probability of finding an electron of arbitrary spin within volume element d**r**.

III.3.1 Hohenberg-Kohn Theorem

In 1964, a major step into the quantitative modeling of the electronic structure was established known as the Hohenberg and Kohn theorems. The two theorems are the following [5]:

- *The external potential is a functional of the electron density within an arbitrary additive constant.* $n(\boldsymbol{r}) \xrightarrow{Hohenberg-Kohn} v(\boldsymbol{r}) + Constant$
- *The true electron density corresponds to the full solution of the Schrödinger equation is the one minimizing the energy of the overall functional.* $E[\rho_0] = minE[\rho]$

The formulation of the Hohenberg and Kohn theorems is based on the assumption that the electron density of the ground state, ρ(**r**), cannot be governed by two different external potentials V_{ext}(**r**), and hence all properties. Thus, the total energy is written as [5] :

$$E[\rho(\boldsymbol{r})] = F_{HF}[\rho(\boldsymbol{r})] + \int \rho(\boldsymbol{r}) V_{ext}(\boldsymbol{r}) d\boldsymbol{r} \tag{III.8}$$

with
$$F_{HK}[\rho(\boldsymbol{r})] = T[\rho(\boldsymbol{r})] + E_{e-e}[\rho(\boldsymbol{r})] \tag{III.9}$$

T[ρ(**r**)] submits to the total kinetic energy, E[ρ(**r**)] is the electron-electron interaction energy, while $F_{HK}[\rho(\boldsymbol{r})]$ is the Hohenberg-Kohn functional.

However, it is still not possible to determine the ground state energy of a system since we do not know the exact term of F[ρ(r)].

III.3.2 The Kohn-Sham Method

In 1965, Kohn and Sham put in work the HK theorem with the suggestion of the Kohn-Sham equation [1]. The idea was to replace the interacting N-particle problem with an auxiliary system of N non-interacting particles. Kohn and Sham reformulated the Schrödinger equation by introducing an effective potential given as the following [1]:

$$\left[-\frac{1}{2}\nabla^2 + V_{eff}(\boldsymbol{r})\right] \varphi_i(\boldsymbol{r}) = \varepsilon_i \varphi_i(\boldsymbol{r}) \tag{III.10}$$

with
$$V_{eff}(\boldsymbol{r}) = V_{ext} + V_H + V_{xc}(\boldsymbol{r}) \tag{III.11}$$

Where $\varphi_i(\boldsymbol{r})$ submits to the nongenerated single-electron wavefunction known as Kohn-Sham orbitals with $\rho(\boldsymbol{r}) = \sum_{i=1}^{N} |\varphi(\boldsymbol{r})|^2$, V_{ext}[ρ(**r**)] is the interaction with the external potential, V_H

represents the Hartree potential with $V_H = \frac{\partial E_H[\rho(\boldsymbol{r})]}{\partial \rho(\boldsymbol{r})} = \int \frac{\rho(\boldsymbol{r}_1)}{\boldsymbol{r}_{12}} d\boldsymbol{r_j}$ and $V_{xc}[\rho(\mathbf{r})]$ is the exchange-correlation potential defined by $V_{xc} = \frac{\partial E_{xc}}{\partial \rho(\boldsymbol{r})}$.

Kohn and Sham suggested that the kinetic energy of the auxiliary system could be determined using the kinetic energy of the real system [5], N-particle interacting, as a function of the ground state density, with $T \neq T_{real}$. The method consists of considering that the kinetic energy of the system contains two parts, T_s and T_c, $T[\rho] = T_s[\rho] + T_c[\rho]$; where T_s represents the kinetic energy of the non-interacting system and T_c is the correlation kinetic energy, with [5]:

$$T_s[\rho(\boldsymbol{r})] = -\frac{1}{2}\sum_{i=1}^{N}\langle\varphi_i|\nabla^2|\varphi_i\rangle \tag{III.12}$$

Therefore, the total energy functional can be written as follows,

$$E_{KS} = T_s[\rho(\boldsymbol{r})] + J[\rho(\boldsymbol{r})] + \int \rho(\boldsymbol{r})V_{ext}(\boldsymbol{r})d\boldsymbol{r} + E_{xc}[\rho(\boldsymbol{r})] \tag{III.13}$$

$J[\rho(\mathbf{r})]$ (Hartree energy) is the classical Coulomb self-repulsion term with $J = \frac{1}{2}\int\int \frac{\rho(\boldsymbol{r}_1)\rho(\boldsymbol{r}_2)}{\boldsymbol{r}_{12}} d\boldsymbol{r}_1 d\boldsymbol{r}_2$ representing the $\rho(\mathbf{r})$ self-interaction energy and $E_{xc}[\rho(\mathbf{r})]$ is the exchange-correlation energy.

More accurate energy $E_{KS}[\rho(\mathbf{r})]$ values require exact exchange-correlation $E_{xc}[\rho(\mathbf{r})]$ functional, thus it must be approximated.

III.3.3 Exchange-Correlation Functional

The idea behind the exchange-correlation term is that it covers the non-classic kinetic and electrostatic terms resulting from the difference between the real $T[\rho(\mathbf{r})]$ and non-interacting $T_S[\rho(\mathbf{r})]$ kinetic energy, and the self-interaction corrections as well as the Colombian exchange and correlation effects, respectively [3,9]. The exchange-correlation energy is given as following [3,9]:

$$E_{xc}[\rho(\boldsymbol{r})] = \left[T[\rho(\boldsymbol{r})] - T_S[\rho(\boldsymbol{r})]\right] + \left[E_{ee}[\rho(\boldsymbol{r})] - J[\rho(\boldsymbol{r})]\right] \tag{III.14}$$

The main usual approximations of the exchange-correlation energy are cited in the next section.

III.3.3.1 The Local Density Approximation (LDA)

The first and most standard approximation is known as the Local Density Approximation LDA. It is based on the assumption that the exchange-correlation functional in an inhomogeneous system could be approximated as an integral over a local function of the homogeneous charge density given by [10]:

$$E_{xc}^{LDA}[\rho(\boldsymbol{r})] = \int \rho(\boldsymbol{r})\varepsilon_{xc}^{unif}[\rho(\boldsymbol{r})]d\boldsymbol{r} \tag{III.15}$$

Where $\varepsilon_{xc}[\rho(\mathbf{r})]$ represents the XC energy per electron of the uniform electron gas of density $\rho(\mathbf{r})$. It is written as a sum of exchange and correlation terms [10],

$$\varepsilon_{xc}^{unif}[\rho(\boldsymbol{r})] = \varepsilon_{x}^{unif}[\rho(\boldsymbol{r})] + \varepsilon_{c}^{unif}[\rho(\boldsymbol{r})] \tag{III.16}$$

The $\varepsilon_x[\rho(\boldsymbol{r})]$ term was calculated by Dirac and Slater [3] as $\varepsilon_x[\rho(\boldsymbol{r})] = -\frac{3}{4}\left(\frac{3\rho(r)}{\pi}\right)^{1/3}$, while there is no analytical expression to calculate the $\varepsilon_c[\rho(\boldsymbol{r})]$ correlation terms. However, it has been estimated using Monte Carlo calculations.

For the case of parallel and antiparallel spins, the $E_{KS}[\rho(\mathbf{r})]$ energy is a functional of the electron spin densities known as Local Spin Density Approximation LSDA [11]

$$\rho(\boldsymbol{r}) = \rho_{\uparrow}(\boldsymbol{r}) + \rho_{\downarrow}(\boldsymbol{r}) \tag{III.17}$$

$$E_{xc}^{LDA}[\rho(\boldsymbol{r})] = \int \varepsilon_{xc}^{unif}\rho\{(\boldsymbol{r})](\rho_{\uparrow}(\boldsymbol{r}),\rho_{\downarrow}(\boldsymbol{r})\}d\boldsymbol{r} \tag{III.18}$$

The accuracy of the LDA approximation can be clearly seen in the crystalline, atomic and small molecular interacting systems [12] when the electron density shows a low spatial variation which is not always the case. Therefore, alternative exchange-correlation functional approximations have been developed.

III.3.3.2 Generalized Gradient Approximation (GGA)

In fact, the idea of taking the electron density $\rho(\mathbf{r})$ at a particular point $\mathbf{r}$ to calculate the XC energy gives less accurate results when considering the systems as inhomogeneous. GGA comes up with the assumption that the $\varepsilon_x[\rho(\boldsymbol{r})]$ energy is a function of both electron density $\rho(\mathbf{r})$ supplemented with its gradient $\nabla\rho(\mathbf{r})$[3]:

$$E_{xc}^{GGA}[\rho(\boldsymbol{r})] = \int \varepsilon_{xc}^{GGA}[\rho(\boldsymbol{r}),\nabla\rho(\mathbf{r})]\mathrm{d}\mathbf{r} \tag{III.19}$$

The GGA is a semi-local approximation by introducing a non-local term - gradient of the density $\nabla\rho(\mathbf{r})$ - into the XC functional energy. In order to determine the $\varepsilon_x[\rho(\boldsymbol{r})]$ and $\varepsilon_c[\rho(\boldsymbol{r})]$ contributions, many GGA functionals have been proposed; PW91, PB and PBE are the most common ones [1,4].

Alternatively, GGA functionals are combined with the Hartree-Fock exchange energy E_{xc}^{HF} approximation constituting the class of hybrid functionals that are widely used in chemical applications [1]. The most commonly used functionals are B3LYP and PBE0.

III.3.4 DFT+U

III.3.4.1 Hubbard Parameter

One of the most well-known cases of DFT failure involves highly correlated systems comprising compounds containing rare earth elements or *d* and *f* transition metal oxides. In fact, *d/f* electrons are considered to be localized at metal ions where the Coulomb correlation between these *d*/*f* electrons prevents them from forming an incompletely filled *d*/*f* band. This strong coulomb energy cannot be treated correctly using conventional DFT calculations [13]. As a solution, the electronic interactions are divided into localized (called on-site interactions) and delocalized states, where each state is treated with an appropriate functional known as the DFT+U approach [14,15], the Hamiltonian and total energy are then written as follows [14]:

$$H = H_{DFT} + H_U \tag{III.20}$$

$$E[\rho(\boldsymbol{r})] = E_{DFT}[\rho(\boldsymbol{r})] + E_U[\rho(\boldsymbol{r})] \tag{III.21}$$

where, H_{DFT} is the DFT Hamiltonian based on total electron density, H_U is the Hamiltonian resulting from the Hubbard correction corresponding to the coulomb and exchange interactions between electrons localized on the same atom with similar angular momentum.

The DFT+U energy correction is given by [16]

$$E_U[\rho(\boldsymbol{r})] = E_{Hub}[\rho(\boldsymbol{r})] - E_{dc}[\rho(\boldsymbol{r})] \tag{III.22}$$

with $E_{hub}[\rho(\mathbf{r})]$ representing the on-site interactions and $E_{dc}[\rho(\mathbf{r})]$ is a double containing term representing the correction of the fact that the on-site interactions are included in both $E_{DFT}[\rho(\mathbf{r})]$ and $E_{hub}[\rho(\mathbf{r})]$. DFT+U approach showed more accurate results specifically for band structure calculation for a variety of transition metal oxides as well as the rare earth compound [17,18].

III.3.4.2 Spin Polarization

Spin-polarized DFT was introduced to model systems containing unpaired electrons. In such a system, if the numbers of spin-up and spin-down electron states are different where the same spatial orbital is no longer shared, spin polarization may occur. This case is clearly remarkable when the electrons are strongly localized, which means the presence of magnetism. The majority of spin-polarized systems can be studied using the collinear-spin approximation. Consequently, a set of spin-polarized KS equations is then obtained, one for each spin [19,20]. The total energy of the system is then written as [19,20]

$$E\left[\rho(\boldsymbol{r})_\alpha, \rho(\boldsymbol{r})_\beta\right] = T_s\left[\rho(\boldsymbol{r})_\alpha, \rho(\boldsymbol{r})_\beta\right] + J\left[\rho(\boldsymbol{r})_\alpha, \rho(\boldsymbol{r})_\beta\right] + E_{xc}\left[\rho(\boldsymbol{r})_\alpha, \rho(\boldsymbol{r})_\beta\right] + \int v_{ext}^{\alpha}\rho(\boldsymbol{r})_\alpha d\boldsymbol{r} + \int v_{ext}^{\beta}\rho(\boldsymbol{r})_\beta d\boldsymbol{r} \qquad \text{(III.23)}$$

Where $\rho(\boldsymbol{r})_\alpha = \sum_i^{N\alpha} n_\alpha |\varphi_{i\alpha}(\boldsymbol{r})|^2$ and $\rho(\boldsymbol{r})_\beta = \sum_i^{N\beta} n_\alpha \left|\varphi_{i\beta}(\boldsymbol{r})\right|^2$ are the electron spin-up and spin-down functional densities [6], respectively.

The KS approach then implies solving $N=N_\alpha+N_\beta$ one-electron equations [21]

$$\left[-\frac{1}{2}\nabla^2 + V_{eff}^{\alpha}(\boldsymbol{r})\right]\varphi_{i\alpha}(\boldsymbol{r}) = \varepsilon_{i\alpha}\varphi_{i\alpha}(\boldsymbol{r}) \text{ and } \left[-\frac{1}{2}\nabla^2 + V_{eff}^{\beta}(\boldsymbol{r})\right]\varphi_{i\beta}(\boldsymbol{r}) = \varepsilon_{i\beta}\varphi_{i\beta}(\boldsymbol{r}) \qquad \text{(III.24)}$$

where the normalization constraints are $\langle\varphi_{i\alpha}|\varphi_{i\alpha}\rangle = 1$ and $\langle\varphi_{i\beta}|\varphi_{i\beta}\rangle = 1$.

III.3.5 Self-Consistent Procedure

A variety of methods have been developed to obtain an approximate solution of the Kohn-Sham equation. The most known one is the self-consistent field approximation (SCF). This technique consists of starting with an initial guess for the overall electron density. Using this density, the effective potential is then determined followed by solving the KS equation. A new electron density is then calculated, if this new electron density does not match with the first one then a second iteration is requested where the two densities are mixed and considered as a new starting electron density. The simplest mixing scheme is the linear mixing [19]:

$$\rho_{in}^{i+1} = (1-\alpha)\rho_{in}^{i} + \alpha\rho_{out}^{i} \qquad \text{(III.25)}$$

Where α is the mixing parameter and *i* refers to the iteration number.

The iterative process is stopped once the input and output densities satisfy certain accuracy criteria leading to a self-consistent solution. The process is illustrated in Figure III.1.

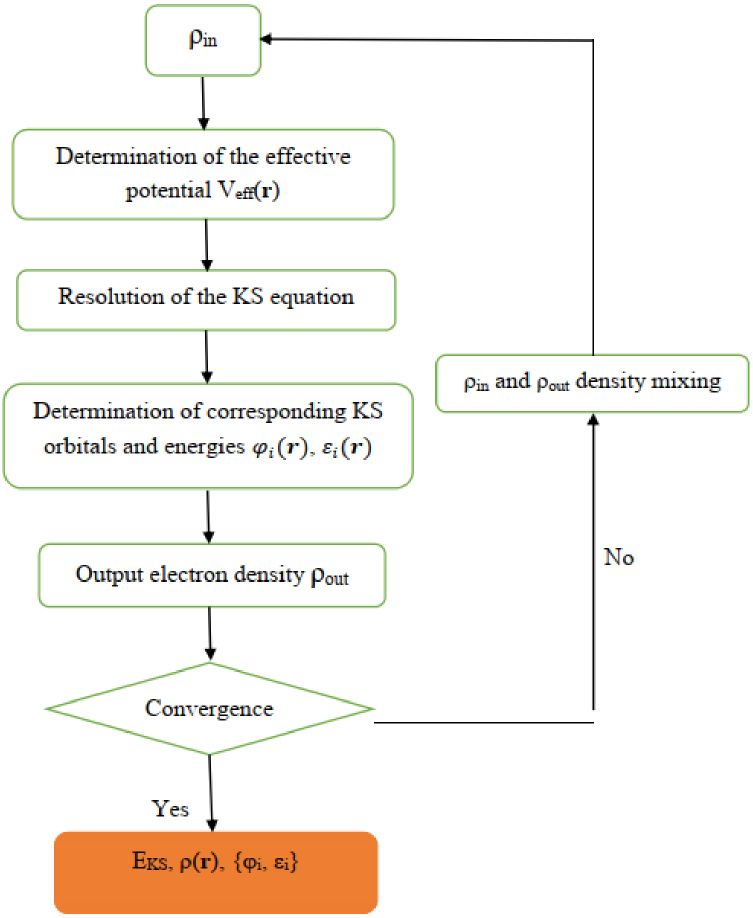

Figure III.1: Diagram of the self-consistent resolution of the Kohn-Sham equation.

III.3.6 Plane Waves Approach

The solution of the Schrödinger equation must satisfy a fundamental property known as Block's theorem [22], which states that the wave function should be written as the product of a plane wave with a function $u_j(\mathbf{r})$ [22]

$$\varphi_j(\boldsymbol{r}) = u_j(\boldsymbol{r})e^{\boldsymbol{ikr}} \qquad \text{(III.26)}$$

Where $\varphi_j(\boldsymbol{r})$ is the wave function, $u_j(\mathbf{r})$ is a periodic function in space with $u_j(\boldsymbol{r}) = u_j(\boldsymbol{R} + \boldsymbol{r})$, **k** and **R** are the wave vector and translator vector, respectively.

Since the electronic wavefunction of a set of **k**-points that are very close is the same, it is possible to represent the electronic wave functions over a region of **k** space by the wave functions at a single **k**-point [8,23]. Thus, each KS wave function is a sum of plane waves and the periodic function, which means that for each value of **k**, a solution for the KS equation is found. Due to the periodicity of the system, the number of electron orbitals treated are limited into a primitive cell - Brillouin Zone- with d$\mathbf{k}^3$ volume where $\mathbf{k}<\mathbf{k}_{max}$ with associated cut-off energy of $E_{cut-off} = \frac{\hbar^2 k_{max}{}^2}{2m_e}$ which is the energy that controls the number of plane waves used in the calculation process, the plan waves with energy above E_{cut} are not considered. The **k**-point set is chosen based on the Monkhorst-Pack scheme, where the general rule is then that the number of points chosen along each axis of the reciprocal space should be in inverse proportion to the dimensions of the unit cell in real space [4]. The accuracy of the results improves with dense **k-**mesh.

III.3.7 Pseudopotential Concept

For solids and molecules, electrons are distinguished according to their contribution to the chemical bonding and physical properties of the materials into valence electrons and core electrons. The core electrons are those considered to be strongly localized around the nucleus, thus, a large number of plane waves and very high energy cutoff are needed to expand these tightly bound core orbitals and the large oscillations of the wave function near the nucleus which means an extremely large plane-wave basis set would be required to solve the KS equation. Therefore, the core electrons are considered to be fixed.

The pseudopotential approximation raises on the fact of using an effective interaction, pseudopotential to replace the strong ionic potential [24]. The valence wavefunctions oscillate rapidly in the core region, thus, the PP is constructed so that its scattering properties or phase shifts for the pseudo-wave functions are identical to the scattering properties of the ion and the core electrons for the valence wave functions [4,19]. As well as, the pseudopotential matches the true potential outside a given radius, designated the core radius, r_c [4,19];

$r > r_c$

$$\Psi^{PP}(\boldsymbol{r}) = \Psi(\boldsymbol{r}) \tag{III.27}$$

$$V^{PP}(\boldsymbol{r}) = V(\boldsymbol{r}) \tag{III.28}$$

where $\Psi^{PP}(\mathbf{r})$ and $\Psi(\mathbf{r})$ are the ground state pseudo- and all-electron wavefunctions, respectively. $V^{PP}(\mathbf{r})$ and $V(\mathbf{r})$ are the pseudo- and all-electron potentials, respectively.

The ionic potential, valence wavefunction besides to the corresponding pseudopotential and pseudo wavefunction are illustrated schematically in Figure III.2. The pseudo wavefunction is constructed in such a way that it has no radial nodes in the core region.

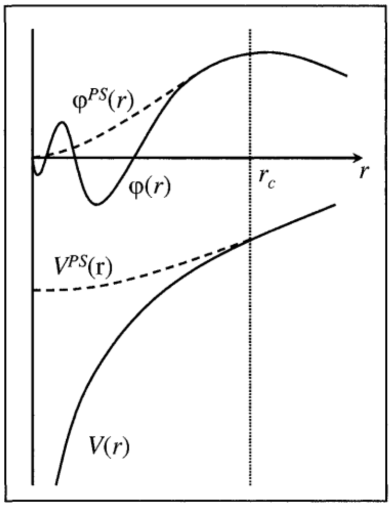

Figure III.2: Schematic illustration of the replacement of the all-electron wavefunction and core potential by a pseudo-wavefunction and pseudopotential [24].

III.3.7.1 Norm Conserving Pseudopotential

The concept of the norm-conserving pseudopotential is based on the adjustment of the pseudopotential to ensure that the integrals of the squared amplitudes of the real and the pseudo wave functions inside the core regions are identical which guarantees the equality of the wave function and pseudo wave function outside the core region [8,19]:

$$\Psi^{PP}(\boldsymbol{r}) = \Psi(\boldsymbol{r}) \qquad \text{if } r > r_c \qquad \text{(III.29)}$$

$$\int_0^{r_c} dr|\Psi^{PP}(\boldsymbol{r})|^2 r^2 = \int_r^{r_c} dr|\Psi(\boldsymbol{r})|^2 r^2 \qquad \text{if } r < r_c \qquad \text{(III.30)}$$

Besides, there is another condition imposed on the PP is that the pseudo-energy-eigenvalues (ε_l^{PP}) should match the true valence eigenvalues (ε_l) [19]:

$$\varepsilon_l^{PP} = \varepsilon_{nl} \qquad \text{(III.31)}$$

l represents the angular momentum and *n* denotes the principal quantum number.

The norm-conserving pseudopotentials are known as hard PP, i.e., the pseudopotentials require high cutoff energies. Methods for constructing norm-conserving pseudopotentials were basically developed by Hamann et *al*. and first applied by Bachelet, Hamann and Schlüter (BHS) who tabulated accurate pseudopotentials for all the elements of the periodic table [24].

III.3.7.2 Ultrasoft Pseudopotential

The norm-conserving condition, inside the core, is the main factor responsible for the hardness of the PP. Vanderbilt comes out with the proposition that the pseudo-wave functions are considered to be equal to the all-electron wavefunctions outside r_c, but inside r_c the pseudo-wavefunctions are considered to be as soft as possible omitting the norm-conserving condition. For this loss, some complications are introduced. The pseudo-wave functions are not necessarily normalized inside r_c, besides, it could lead to wrong density charge values where the density is not determined by calculating $\sum \varphi^{*}\varphi$ as with norm-conserving PP. However, the ultrasoft PP are constructed for use in large scale calculations, especially first-row elements and elements with shallow d-shells, when the cost of the calculation is much more important than that of generating pseudopotentials [19].

III.4. DFT Programs

III.4.1 Cambridge Sequential Total Energy Package Code (CASTEP)

Quantum mechanical calculations of the bulk $LaFeO_3$ perovskite were performed using the CASTEP code. This code is part of the Material Studio modeling software environment developed by Payne in 1986 [25,26]. CASTEP uses the density functional theory to solve the Schrödinger equation through the plane-wave pseudo-potential (PW-PP) method. This code is widely used to explore the properties of systems with periodic boundary conditions such as semiconductors, metals, ceramics and minerals. The electronic wave-functions are expanded in a plane wave basis sets defined based on periodic boundary conditions (PBC) and Bloch’s theorem. The ion-electron potential is described through the norm-conserving or ultrasoft pseudopotentials. The combination of pseudopotentials and plane waves basis sets makes it extremely easy to calculate the forces on the atoms which allows an efficient optimization of the ionic configurations.

III.4.2 Dmol^3 Code

Surface properties were investigated using the Dmol^3 package from the material studio software. Dmol^3 code employs the DFT to simulate different properties of solids, molecules and surfaces and also predict chemical processes. Dmol^3 is used on a broad range of systems including molecular structures, organic and inorganic molecules, surfaces of solids and especially for large systems with over 500 atoms [27]. This package is widely used because of its highly accurate results at the same time with low computational costs. The atomic basis functions in Dmol^3 are carried out by solving the Schrödinger equation for an isolated atom. Numerical orbitals are used for the basis function where each function corresponds to an atomic orbital (AO). As a consequence, the use of these atomic orbitals improves the molecular polarizabilities description and minimizes the basis set superposition effects [28]. Both all-electron and pseudo-potential calculations can be performed using Dmol^3. The core electrons are treated in different ways; DFT semi-local pseudo-potentials (DSPP) or the Effective Core Potentials (ECP), which is more conventional, can be used. Using Dmol^3, the charge density is fitted to multipolar densities attached to the atoms; atomic-centered partial densities.

References

[1] Engel, E. (2011). *Density functional theory*. Springer-Verlag Berlin. DOI: 10.1007/978-3-642-14090-7.

[2] Freyss, M. (2015). Density functional theory (NEA-NSC-R--2015-5). Nuclear Energy Agency of the OECD (NEA)

[3] Koch, W., & Holthausen, M. C. (2015). *A chemist's guide to density functional theory*. John Wiley & Sons. DOI: 10.1002/9781119015625.

[4] Sholl, D. S., & Steckel, J. A. (2022). *Density functional theory: A practical introduction*. John Wiley & Sons. DOI: 10.1002/9781119015625.

[5] Patterson, J. D. (1989). Density-functional theory of atoms and molecules: Robert G. Parr and Weitao Yang. Oxford University Press, New York, and Clarendon Press, Oxford (1989). US $55. 333 pages. DOI: 10.1093/oso/9780195092769.001.0001.

[6] Eschrig, H. (1996). *The fundamentals of density functional theory* (Vol. 32). Stuttgart: Teubner. DOI: 10.1007/978-3-322-97620-8.

[7] Spellmeyer, D. (Ed.). (2006). *Annual reports in computational chemistry*. Elsevier.

[8] Bechstedt, F. (2016). *Many-body approach to electronic excitations*. Springer-Verlag Berlin Heidelberg. DOI: 10.1007/978-3-662-44593-8.

[9] Keller, J., & Gázquez, J. L. (Eds.). (1983). *Density functional theory (Vol. 187)*. Springer-Verlag Berlin Heidelberg. DOI: 10.1007/3-540-12721-6.

[10] Harrison, N. M. (2003). An introduction to density functional theory. *Nato Science Series Sub Series III Computer and Systems Sciences*, *187*, 45-70.

[11] Gonis, A., Kioussis, N., & Ciftan, M. (Eds.). (2012). *Electron correlations and materials properties*. Springer Science & Business Media. DOI: 10.1007/978-1-4615-4715-0.

[12] Argaman, N., & Makov, G. (2000). *Density functional theory: An introduction*. American Journal of Physics, 68(1), 69-79. DOI: 10.1119/1.19375.

[13] Mosey, N. J., & Carter, E. A. (2007). Ab initio evaluation of Coulomb and exchange parameters for DFT+U calculations. *Physical Review B*, *76*(15), 155123. DOI: 10.1103/PhysRevB.76.155123.

[14] Cococcioni, M., & De Gironcoli, S. (2005). Linear response approach to the calculation of the effective interaction parameters in the LDA+U method. *Physical Review B*, *71*(3), 035105. DOI: 10.1103/PhysRevB.71.035105.

[15] Mosey, N. J., Liao, P., & Carter, E. A. (2008). Rotationally invariant ab initio evaluation of Coulomb and exchange parameters for DFT+U calculations. *The Journal of Chemical Physics*, *129*(1), Article 014103. DOI: 10.1063/1.2943142.

[16] Gómez-Ortiz, F., Carral-Sainz, N., Sifuna, J., Monteseguro, V., Cuadrado, R., García-Fernández, P., & Junquera, J. (2023). Compatibility of DFT+U with non-collinear magnetism and spin-orbit coupling within a framework of numerical atomic orbitals. *Computer Physics Communications*, *286*, 108684. DOI: 10.1016/j.cpc.2023.108684.

[17] Lambert, D. S., & O'Regan, D. D. (2023). Use of DFT+U+J with linear response parameters to predict non-magnetic oxide band gaps with hybrid-functional accuracy. *Physical Review Research*, *5*(1), 013160. DOI: 10.1103/PhysRevResearch.5.013160.

[18] Varignon, J., Bibes, M., & Zunger, A. (2019). Origin of band gaps in 3d perovskite oxides. *Nature Communications*, *10*(1), 1658. DOI: 10.1038/s41467-019-09698-6

[19] Singh, D. J., & Nordstrom, L. (2006). *Planewaves, pseudopotentials, and the LAPW method*. Springer Science & Business Media. DOI: 10.1007/978-3-662-02315-9.

[20] Liu, S. (2022). *Conceptual density functional theory: Towards a new chemical reactivity theory*. John Wiley & Sons. DOI: 10.1002/9783527348435.

[21] Khaetskii, A. V. (2017). *Spin physics in semiconductors (Vol. 1)*. M. I. Dyakonov (Ed.). Berlin: Springer. DOI: 10.1007/978-3-319-65436-2.

[22] Bloch, F. (1929). On the quantum mechanics of electrons in crystal lattices. *Z. Physik*, *52*, 555–600.

[23] Perdew, J. P., & Kurth, S. (2003). Density functionals for non-relativistic Coulomb systems in the new century. In *A primer in density functional theory* (pp. 1-55). Berlin, Heidelberg: Springer Berlin Heidelberg. DOI: 10.1007/3-540-37072-2_1.

[24] Payne, M. C., Teter, M. P., Allan, D. C., Arias, T. A., & Joannopoulos, A. J. (1992). Iterative minimization techniques for ab initio total-energy calculations: molecular dynamics and conjugate gradients. *Reviews of Modern Physics*, *64*(4), 1045. DOI: 10.1103/RevModPhys.64.1045.

[25] Clark, S. J., Segall, M. D., Pickard, C. J., Hasnip, P. J., Probert, M. I., Refson, K., & Payne, M. C. (2005). First principles methods using CASTEP. *Zeitschrift für Kristallographie-Crystalline Materials*, *220*(5-6), 567-570. DOI: 10.1524/zkri.220.5.567.65075.

[26] Segall, M. D., Lindan, P. J., Probert, M. A., Pickard, C. J., Hasnip, P. J., Clark, S. J., & Payne, M. C. (2002). First-principles simulation: ideas, illustrations and the CASTEP code. *Journal of Physics: Condensed Matter*, *14*(11), 2717. DOI: 10.1088/0953-8984/14/11/301.

[27] Delley, B. (2000). From molecules to solids with the DMol3 approach. *The Journal of Chemical Physics*, *113*(18), 7756-7764. DOI: 10.1063/1.1316015.

[28] Delley, B. (1990). An all-electron numerical method for solving the local density functional for polyatomic molecules. *The Journal of Chemical Physics*, *92*(1), 508-517. DOI: /10.1063/1.458452.

Chapter IV:

Synthesis and Characterization of $LaFeO_3$ Perovskite

The first part of this chapter presents the experimental procedure for the synthesis of $LaFeO_3$ nanoparticles by the sol-gel method. These powders were developed from two different precursors, nitrate and chloride salts. The second part of this chapter highlights the results and discussion of the different properties of the two types of powders, including crystallinity, specific surface area, morphology, porosity, optical properties and functional groups.

IV.1 Experimental Procedure

IV.1.1 Chemicals

Chemicals used for the synthesis of $LaFeO_3$ nanoparticles are listed in Table IV.1. All chemicals were used without any further purification.

Table IV.1: The chemicals used in this study, their formula, purity and source.

Name of the chemical	Source
Lanthanum nitrate hexahydrate $La(NO_3)_3·6H_2O$, 99.9%	Sigma-Aldrich, USA
Lanthanum chloride hexahydrate $LaCl_3·7H_2O$, 64.5-70%	Sigma-Aldrich, USA
Iron nitrate nonahydrate $Fe(NO_3)_3·9H_2O$, 98%	Prolabo, France
Iron chloride hexahydrate $FeCl_3·7H_2O$	
Citric acid $C_6H_8O_7·7H_2O$, 99.5%	Georgia, USA
Methanol CH_3OH, 100%	VWR chemicals, EC

IV.1.2 Synthesis of $LaFeO_3$ Based on Nitrate Salts

Lanthanum ferrite nanoparticles were synthesized using nitrate salts where 2.15 g of lanthanum nitrate and 2.02 g of ferrite nitrate with a molar ratio of 1:1 were dissolved separately in 25 mL of methanol. The two solutions are mixed once the salts are completely dissolved, followed by the addition of 2.08g of citric acid dissolved in 31 mL of methanol with respect to the $nLa + nFe = 2nCA$ law. The mixture was magnetically stirred to obtain a homogenous solution. The resulting sol was heated at 80°C under magnetic stirring for 4h to ensure the complete evaporation of the solvent and the formation of the gel. The drying of the gel was performed at 100°C for 2h. The solid dry gel was then grounded to obtain a powder. The powder was calcined at 600°C and 800°C for 5h and named NLF1 and NLF2, respectively. The whole process is schematically represented in Figure VI.1.

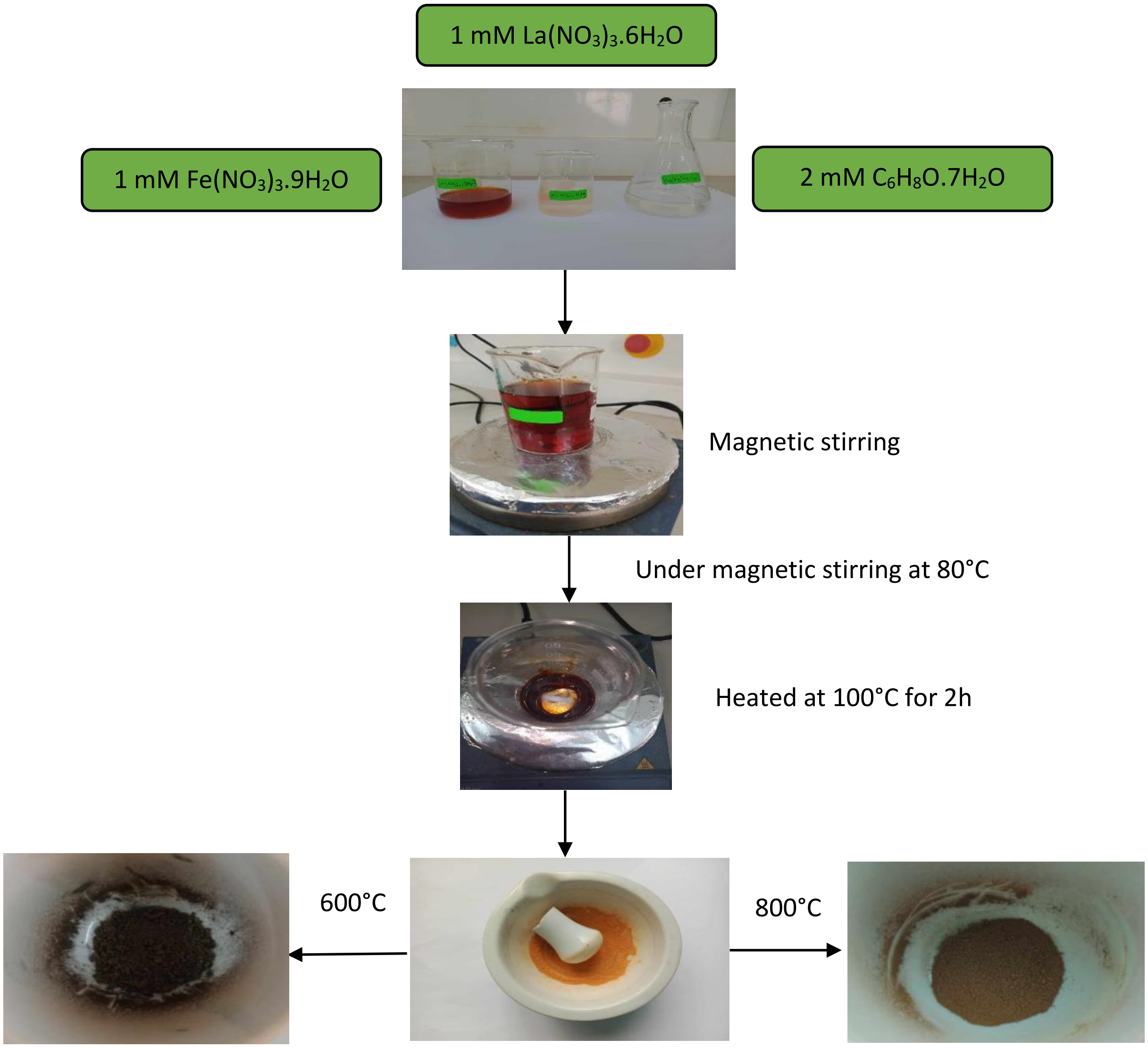

Figure IV.1: Schematic representation of the $LaFeO_3$ synthesis using nitrate salts.

IV.1.3 Synthesis of $LaFeO_3$ based on chloride salts

To synthesize the $LaFeO_3$ powders via chloride salts, 1.86 g of lanthanum chloride and 1.25 g of iron chloride were separately dissolved in 25 mL of methanol under magnetic stirring and once the salts were completely dissolved, the two obtained homogeneous solutions were mixed. After that, solution of citric acid dissolved in 31 mL of methanol with a molar ratio of 1:1:2 was added to the mixture. The resulting solution was heated at 80°C for 10h under magnetic stirring until the sol was completely transformed into a dark brown gel. This gel was dried by heating at 100°C for 4h and then grounded to obtain the powder. The synthesized powder was calcined at three temperatures 600, 800 and 1000°C, denoted as CLF1, CLF2 and CLF3, respectively. The synthesis procedure is summarized in Figure IV.2.

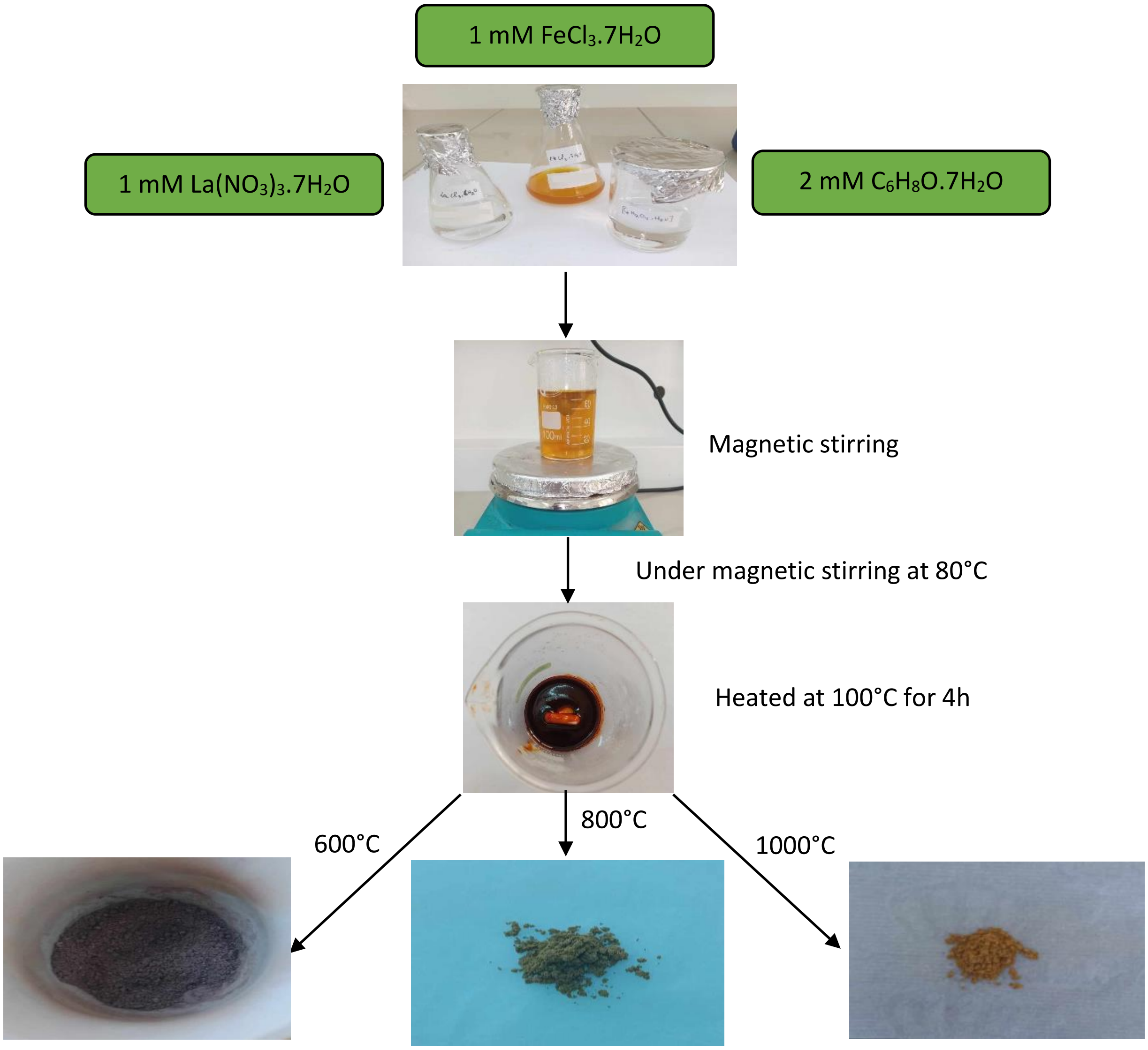

Figure IV.2: schematic representation of the $LaFeO_3$ synthesis using chloride salts.

IV.2 Results and Discussion

IV.2.1 Thermal Analysis (TGA and DTG)

The TGA and its first derivative DTG of the synthesized powders using nitrate and chloride salts are illustrated in Figure IV.3. According to Figure IV.3.a, the thermal decomposition and the final formation of the perovskite phase of the sample synthesized using chloride salts indicate weight loss within four steps. A first weight loss of 1.79 % occurred from room temperature to

180°C which may be due to water loss. Weight loss of 1.07 %, accompanied by a peak at 340°C, is related to the vaporization of volatile organic matter. At around 670°C, a minor weight gain of 0.22% is detected, which could be attributed to the oxidation of the powder, this oxidation is the result of the removed moisture during the first stage of the decomposition process. The mass gain of the sample indicates that there is a formation of an oxy-complex solid due to the adsorption and absorption of oxygen on powder after moisture removal from their pores [1]. The final stage is characterized by a major weight loss of about 9.5% starting directly after the powder oxidation, connected to the large peak centered at 900°C, and is representative of the final stage of the powder decomposition and the formation of the perovskite $LaFeO_3$ phase. This result is in good agreement with that reported by Koferstein et al. [2].

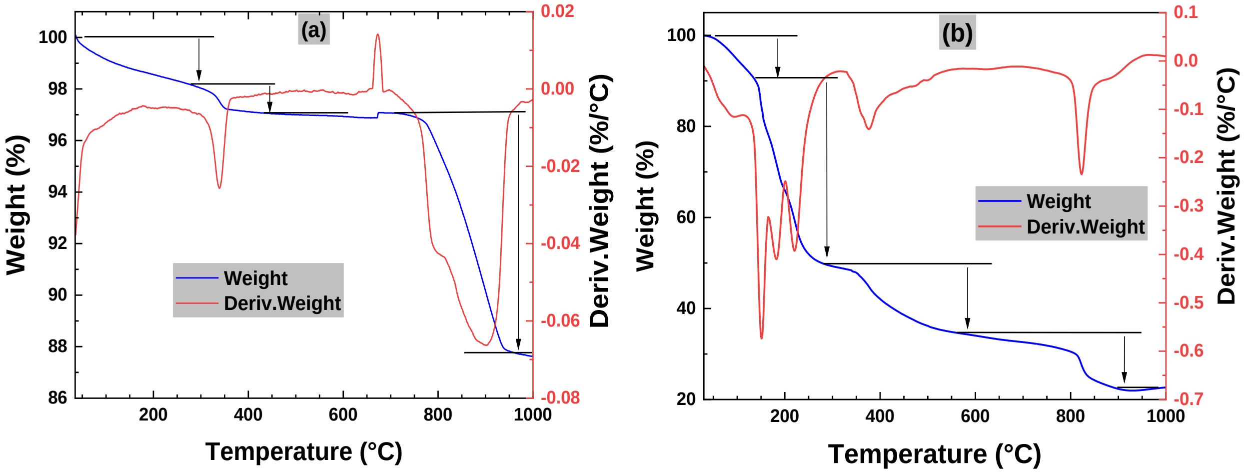

Figure IV.3: TGA and DTG curves for $LaFeO_3$ powders: (a) powder prepared by chloride salts and (b) powder prepared by nitrate salts.

The TG and DTG diagrams, obtained for the powder synthesized with nitrate salts, are presented in Figure IV.3.b. It can be seen that the thermal decomposition of this powder occurred through six stages. The first stage, from room temperature to 120°C, is characterized by a weight loss of ~9 %, where the maximum weight loss occurs at 90°C, and could be attributed to the dehydration process, i.e. removal of water from the powder. During the second stage, in the temperature range 135 - 562°C, the weight loss can be separated into four steps characterized by the corresponding DTG peaks at 150, 180, 220, and 375°C. The major weight loss of ~45 % between 135 and 280°C originated from the vaporization of volatile organic matter. The mass loss of 14% in the temperature range 280 - 562°C results from the removal of reaction products and the beginning of $LaFeO_3$ phase formation. The small DTG peak appearing at 820 °C characterized by a weight loss of 11 % is linked to the final crystallization of the $LaFeO_3$ perovskite phase.

IV.2.2 X-ray Diffraction Analysis

The XRD patterns of the powder synthesized using the two considered routes and calcined at different temperatures are illustrated in Figures IV.4 and IV.5. Starting from the powder prepared by chloride precursor, the first sample CLF1 calcined at 600°C (Figure IV.4.a) shows the total absence of any characteristic peaks of the $LaFeO_3$ phase. Except for the peak presented at 2θ = 36°, which was assigned to the Fe_2O_3 phase (JCPDS-98-020-1101), all the other diffracted peaks were assigned to the LaOCl phase (JCPDS-00-008-0477). The XRD spectrum of the powder calcined at 800°C (sample CLF2) reveals also the presence of typical peaks of the LaOCl phase and the appearance of seven low-intensity peaks of the $LaFeO_3$ perovskite phase at 2θ = 23.3°, 32.9°, 40.4°, 46.7°, 58°, 67.96° and 77.20° which correspond to the diffracted planes (101), (121), (220), (202), (321), (242) and (402), respectively (JCPDS-98-015-3536). This result agrees well with that reported by Hessien and Mersal [3].

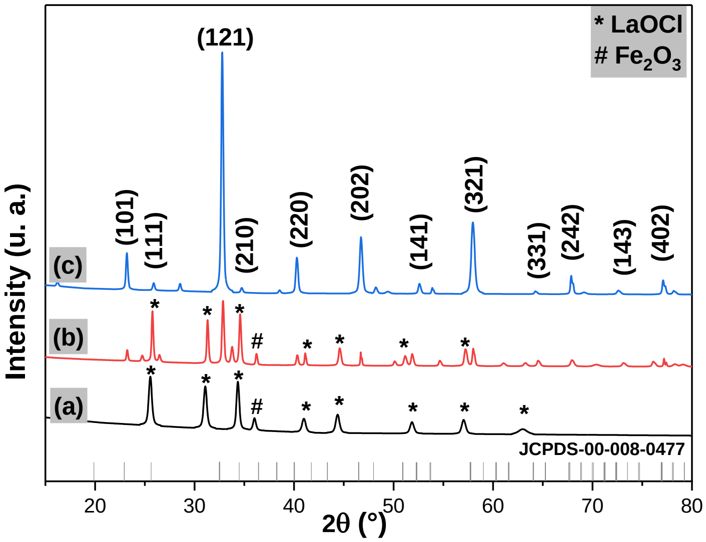

Figure IV.4: X-ray diffraction patterns of $LaFeO_3$ powders: (a) CLF1, (b) CLF2, and (c) CLF3.

Raising the calcination temperature to 1000 °C (CLF3 sample) leads to the total disappearance of the LaOCl phase and the complete formation of the pure $LaFeO_3$ perovskite phase (see Figure

IV.4.c). All diffracted peaks were assigned to the orthorhombic structure (JCPDS-98-015-3536) of the $LaFeO_3$ (space group Pnma, #62).

Figure IV.5 depicts the XRD patterns of the powders prepared by nitrate precursors. Dissimilarly to the powders prepared using chloride precursors (CLF1 and CLF2 samples), the XRD pattern recorded for those synthesized using nitrate precursors, NLF1 calcined at 600°C (Figure IV.5.a) and NLF2 calcined at 800°C (Figure IV.5.b), display the formation of the pure $LaFeO_3$ perovskite phase. For both samples, all the diffracted peaks correspond to those of the orthorhombic structure (Pnma #62) of $LaFeO_3$ according to JCPDS-98-015-3536 file. A similar result was reported by Jia et al. [4]. The above results demonstrate clearly the important effect of precursor type and annealing temperature on the formation of $LaFeO_3$ perovskite and its crystallinity quality.

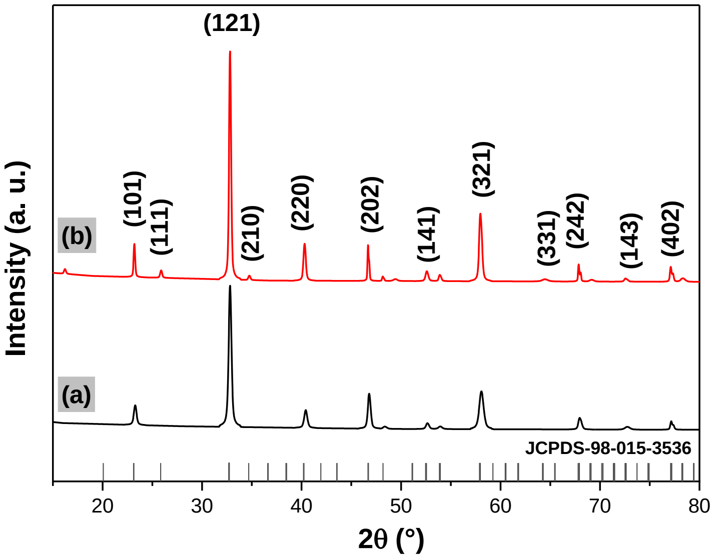

Figure IV.5: X-ray diffraction patterns of $LaFeO_3$ powders: (a) NLF1 and (b) NLF2.

The three samples NLF1, NLF2 and CLF3, for which the pure perovskite phase was formed, were selected for the rest of the study.

For an orthorhombic structure, the lattice parameters were calculated using the following equation [5]

$$d_{hkl} = \frac{1}{\sqrt{\frac{h^2}{a^2}+\frac{k^2}{b^2}+\frac{l^2}{c^2}}} \qquad \text{(IV.1)}$$

Where a, b and c represent the lattice parameters, h, k and l are the Miller indices, d_{hkl} is the interplanar distance.

The crystallite size and microstrain of the three samples have been calculated using Eq (II.5) and Eq (II.6). The variation of the lattice parameters, crystallite size and the microstrain with precursor and calcination temperature is depicted in Table IV.2.

Table IV.2: Variation of the lattice parameters, crystallite size and microstrain with precursor and calcination temperatures.

Parameter	NLF1	NLF2	CLF3	Reference
a (Å)	5.54	5.55	5.57	5.56
b (Å)	7.81	7.83	7.86	7.85
c (Å)	5.52	5.549	5.53	5.551
V (Å^3)	238.84	241.14	242.12	242.28
D (nm)	52	55	86	
ε	0.0018	0.0012	0.0008	

The obtained lattice parameters are in good agreement with the previously reported ones [6]. Besides, the values of the lattice parameters and volume were increased with increasing the calcination temperature, as well as, when changing the precursor from chloride to nitrate. Regarding the estimated values of the average crystallite size, one can see that the crystallite size increases in the same sequence of increasing annealing temperature, i.e., NLF1 (600°C) → NLF2 (800°C) → CLF3 (1000°C). In addition, the results of the microstrain calculations of the selected samples show that high crystallite size values correspond to small microstrain. These results are in agreement with the well-known relation between the volume of single crystal (and therefore the volume of crystallite) and the applied temperature ($V \alpha T$). Besides the effect of temperature, the large difference between the particle size of NLF samples and CLF3 can be attributed to the type of precursor used. The use of different precursors introduces different anions like (Cl^-, NO^{3-}) which could affect the grain size (crystallinity) of the final compounds, as demonstrated in many previous studies [7 - 9].

IV.2.3 BET Analysis

The results of the BET analysis demonstrated that the values of the surface area for the three samples are equal to 11.56, 8.90 and 5.94 m^2/g for NLF1, NLF2 and CLF3, respectively. These values are in agreement with those given by Parida et *al.* [10]. The obtained values are consistent with the well-known relationship between crystallite size and surface area: smaller crystallites contain a higher density of surface atoms or molecules, leading to greater surface area per unit mass or volume. The divergence of the values of the specific surface area for the three samples is attributed to the difference in the calcination temperatures as well as the considered precursor for each sample.

IV.2.4 Powders Morphology and Composition

Figure IV.6 illustrates the SEM micrographs of the NLF1, NLF2, CLF2 and CLF3 samples. These images highlight the effect of the used precursor-type on the morphology of the prepared $LaFeO_3$ nanoparticles where the morphology of CLF powders differs significantly from those of NLF. As outlined in Figure IV.6.a, the morphology of the CLF2 sample exhibits small-sized particles forming tightly knit compact agglomerates. The white spots observed on the SEM image could be attributed to chlorine components. The SEM image of the CLF3 sample, shown in Figure IV.6.b, describes the significant effect of increasing annealing temperature on the surface morphology of the sample; where nanopores with nanometric size (~10 nm) are formed and distributed over the structure of the grains. These nanopores are the result of chlorine (Cl^-) liberation from the powder which was confirmed by the corresponding EDX spectra in Figure IV.7.a and 7.b. At high resolutions, the inset in Figure IV.6.b, the structure revealed large grains well-defined with a nanoporous rice shape.

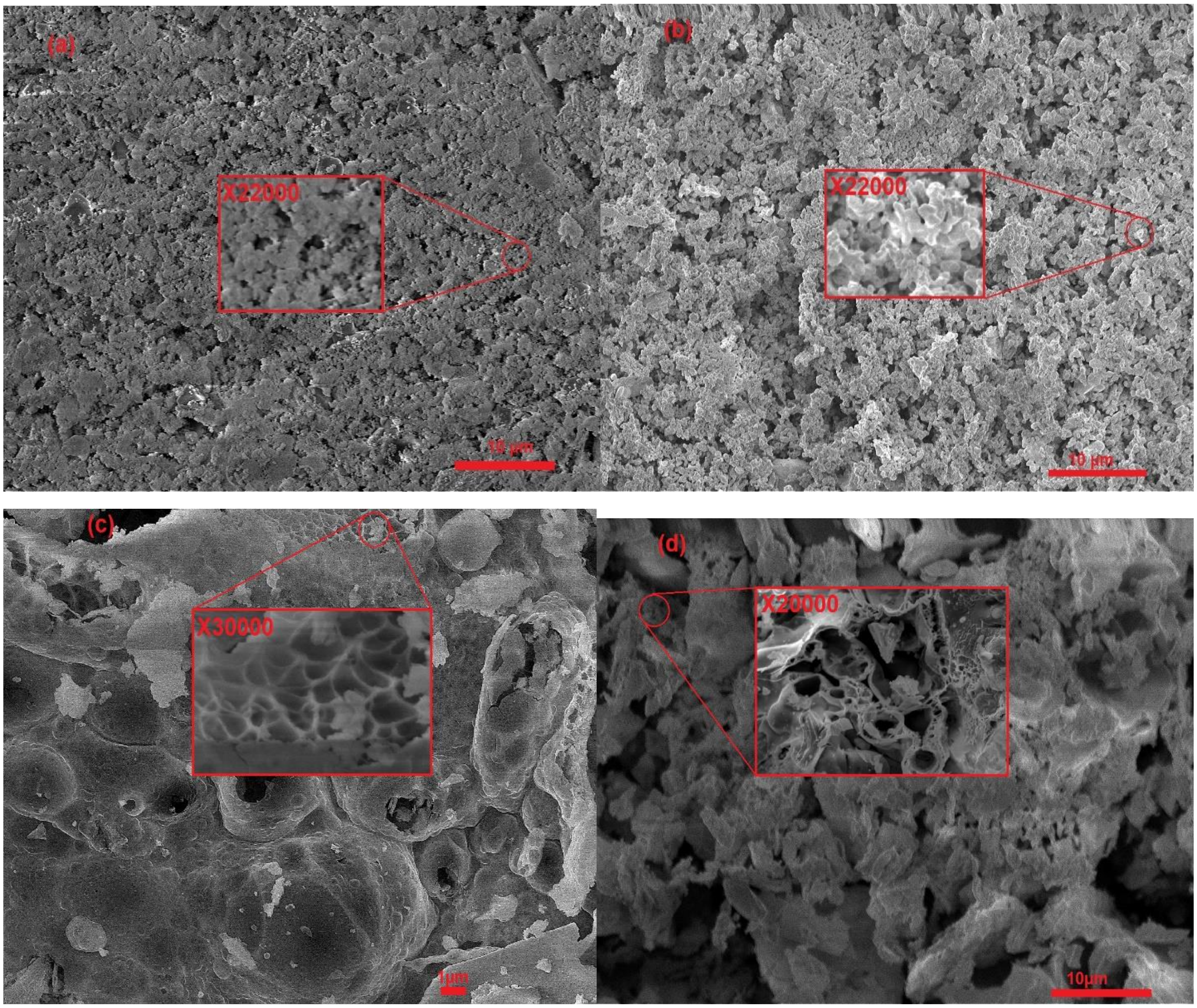

Figure IV.6: SEM images of the (a) CLF2, (b) CLF3, (c) NLF1 and (d) NLF2 samples.

As displayed in Figure IV.6.c and 6.d, a very different surface morphology of the NLF1 and NLF2 could be obviously seen compared to that of the CLF2 and CLF3 samples. The porous morphology of the NLF1 sample is clearly noticeable as illustrated in Figure IV.6.c. The micrographs of the NLF2 powder depicted in Figure IV.6.d illustrate a structure morphology that consists of large crumbly grains with flattened surfaces. At high resolution, exposed by the inset image of Figures IV.6.c and 6.d, multiple cavities of variable dimensions in the range of 5 - 20 µm are detected, these cavities are surrounded by porous walls where the pore size range between 1- 5 µm. The release of NO_x, CO_2 and H_2O gases by the combustion reactions of the used nitrate salts and citric acid could be attributed as the main reason for these created cavities [11].

The elemental composition of the $LaFeO_3$ samples was investigated through the energy dispersive X-ray spectroscopy (EDX) and the relative elemental concentrations of the La, Fe, O and Cl elements are depicted in Figure IV.7. The EDX spectrum of the CLF2 sample is shown in Figure IV.7.a, the presence of an important amount of chlorine of about 12% is demonstrated, which could be attributed to the incomplete burning of Cl during the combustion reaction of chloride salts. Otherwise, the obtained results for CLF3 shown in Figure IV.7.b revealed the disappearance of the chlorine from the $LaFeO_3$ matrix. In contrast, the EDX spectrum of NLF2, plotted in Figure IV.7.c, indicates the absence of any impurities.

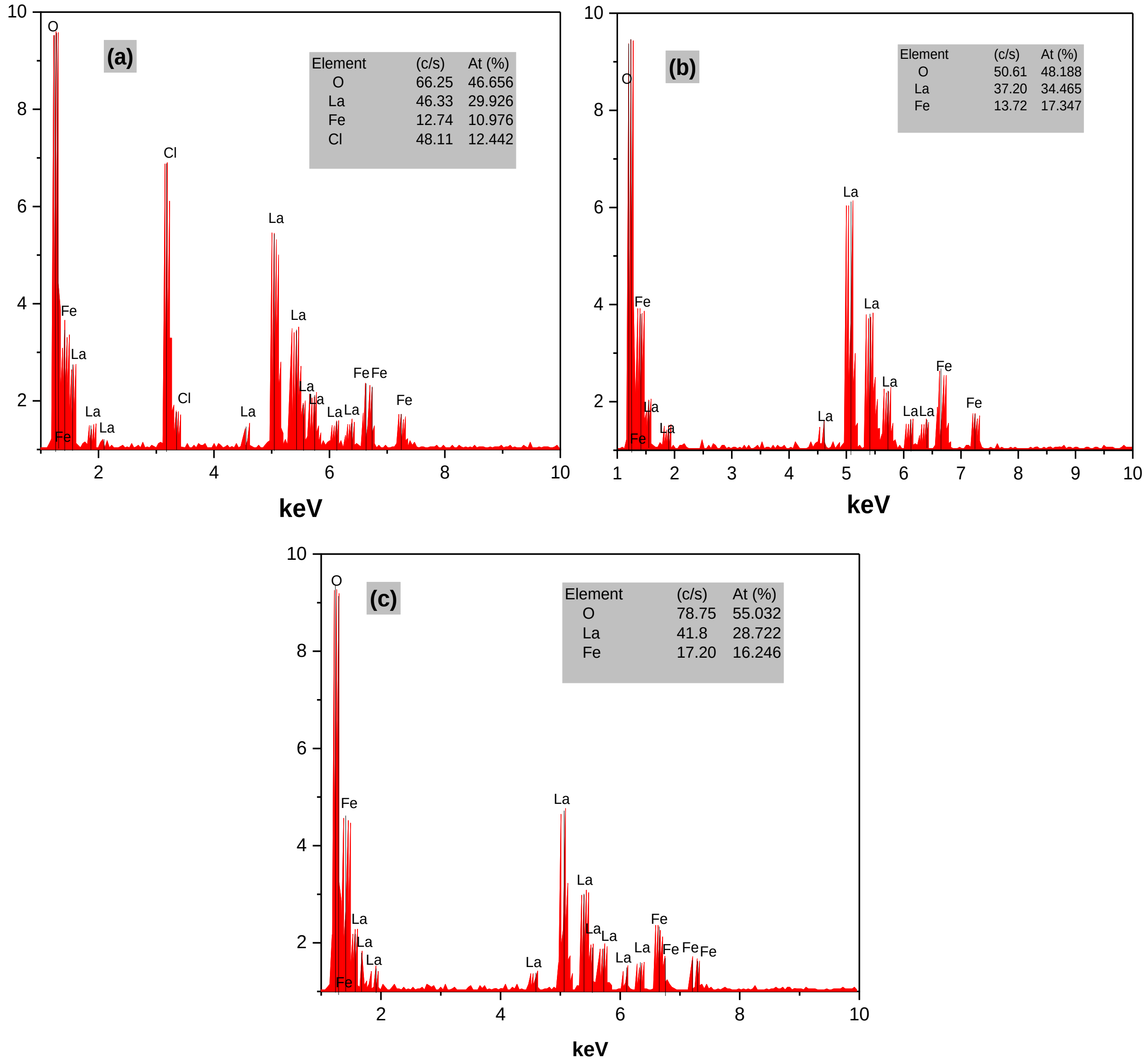

Figure IV.7: EDX spectra of the (a) CLF2, (b) CLF3 and (c) NLF2.

The catalytic and photocatalytic performance of a material can be significantly influenced by the porosity of the studied material. Porosity can also affect the particle surface area, accessibility of active sites and mass transfer of reactants and products. High porosity could be an indication of a high surface area or a low surface area with a large number of pores, results in more sites for photocatalytic reactions and increases the photocatalyst absorption of light by scattering and trapping more incident light, thus leading to an increase in the number of electron-holes generated pairs, which is a critical factor in photocatalytic reactions. The porosity of the $LaFeO_3$ samples, in percentage, is calculated using equation (IV.2) [12-14]:

$$P(\%) = \left(1 - \frac{P_d}{P_{th}}\right) \times 100, \qquad \text{(IV.2)}$$

where P_{th} refers to the theoretical density and P_{d} is the bulk density.

The Archimedes method was used to determine the bulk density of the selected samples while the theoretical density was calculated using the following formula [12-14]:

$$P_{th} = \frac{ZM}{NV} \qquad \text{(IV.3)}$$

in which; Z represents the number of formula units per unit-cell (equal to 4 for the $LaFeO_3$ orthorhombic structure), M is the atomic mass (g), N is the Avogadro number and V is the lattice volume in (cm^3).

The calculated values of theoretical density, bulk density and porosity are summarized in Table IV.3. It is easily remarkable that the porosity increases in the sequence of increasing crystallite size: NLF1 → NLF2 → CLF3.

Table IV.3: Calculated XRD density, bulk density and porosity of the NLF1, NLF2 and CLF3 samples.

Sample	**XRD density ($g.cm^{-3}$)**	**Bulk density ($g.cm^{-3}$)**	**Porosity P (%)**
NLF1	6.69	5.00	25.19
NLF2	6.65	4.70	29.24
CLF3	6.40	3.82	40.21

IV.2.5 Optical Properties

The UV-Vis absorption spectra of $LaFeO_3$ nanoparticles are exposed in Figure IV.8. All three samples NLF1, NLF2, and CLF3 exhibit strong absorption bands around wavelengths of 360 nm and 470 nm in the UV and visible light region, respectively. These absorption bands are in accordance with those reported by Phokha et *al*. [15]. The values of the optical band gap of the three selected samples were calculated using Tauc's relation given by Eq (II.11). The $LaFeO_3$ orthorhombic perovskite is considered to have a direct band gap semiconductor [16], therefore, the *n* value was selected as 1/2.

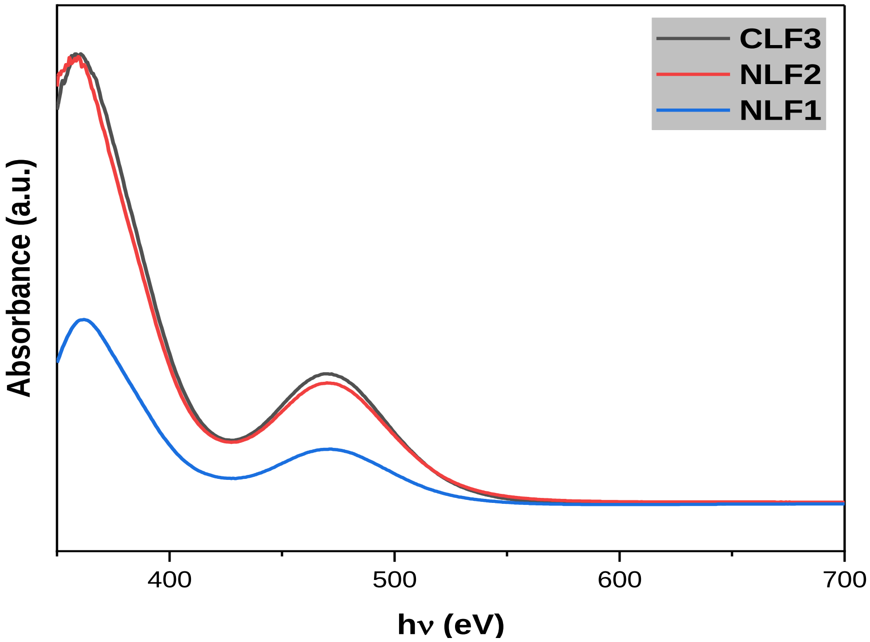

Figure IV.8: UV-Vis absorbance spectra of the prepared samples.

Figure IV.9 illustrates the plots of $(\alpha h\nu)^2$ versus $h\nu$ of the three samples. The optical band gap of the NLF1, NLF2 and CLF3 was found to be equal to 2.25, 2.27 and 2.19 eV, respectively. The relatively low CLF3 band gap compared to that of NLF1 and NLF2 can be attributed to the high crystallite size of the powder prepared by the chloride precursor. These band gap values are consistent with those reported in previous studies [17 - 19].

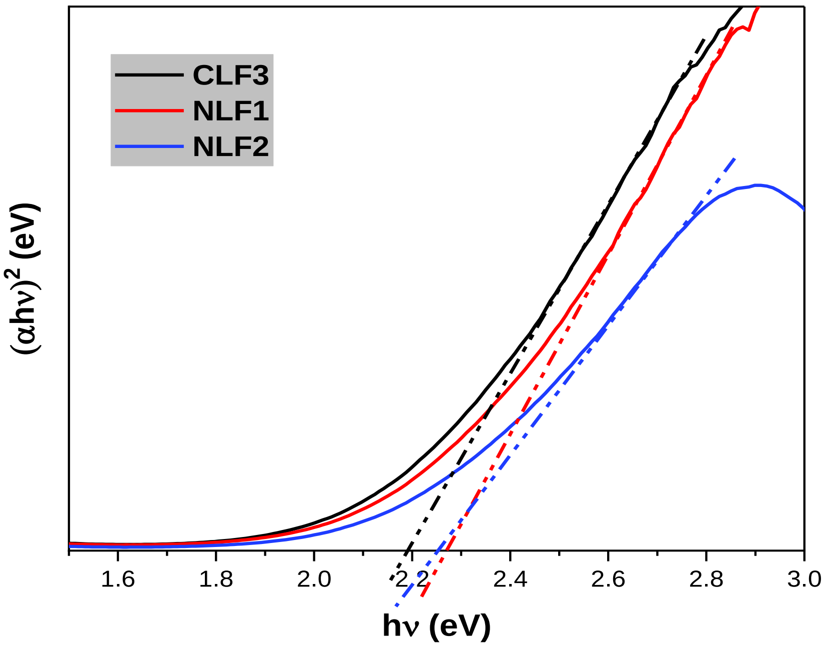

Figure IV.9: The Tauc plots of the NLF1, NLF2 and CLF3 samples.

IV.2.6 FTIR Spectroscopy

Figure IV.10 illustrates the results of the FTIR analysis of the NLF1, NLF2 and CLF3 samples. The spectra of the three samples look very similar, thus, we can say that the effect of the precursor on the chemical bonds and vibrational modes is considered negligible. The spectra reveal a strong absorption band at 560 cm^{-1}, which is attributed to the stretching vibration Fe-O characteristic of FeO_6 octahedra in perovskite (υ_1 mode) [20]. It is noticeable that this characteristic Fe-O peak improves and becomes sharper with the increase of the calcination temperature, which indicates the development of the perovskite phase formation. The band that appears at 700 cm^{-1} results from the bending vibrations of the La-O bonds [16,21]. The La-O peak also becomes sharper, indicating the improvement of crystallinity of $LaFeO_3$ with increasing calcination temperature. The small peak at around 1016 cm^{-1} is assigned to the vibration of the CO_3^{-2}. The bonds observed at 1500-1700 cm^{-1} originated from the stretching vibrations of the carboxylic group C=O and C-O-C whereas the peak at 2355 cm^{-1} could be attributed to the symmetric and asymmetric stretching vibrations of the carboxyl root [16,22]. The slight peak at 2905 cm^{-1} corresponds to the C-H vibrations resulting from the low amount of residual citric acid. The large band at around 3450 cm^{-1} is assigned to the combination of the H-O bending mode of both water molecules and the hydroxyl group [16,21].

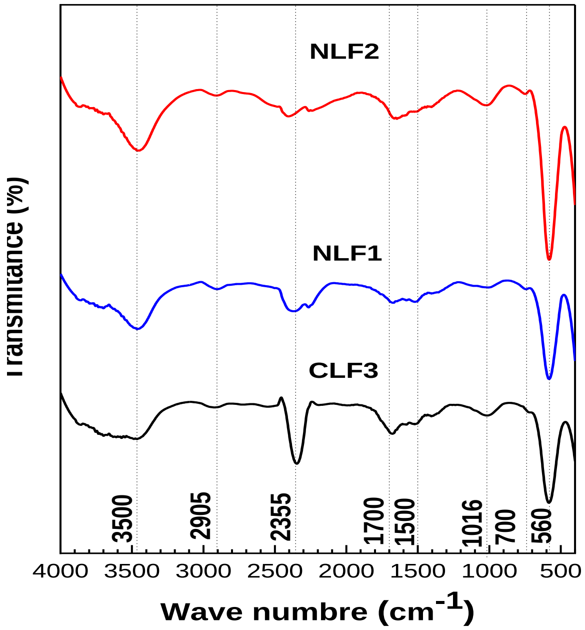

Figure IV.10: FTIR spectra of the NLF1, NLF2 and CLF3 samples.

References

[1] Mohalik, N. K., Mandal, S., Ray, S. K., Khan, A. M., Mishra, D., & Pandey, J. K. (2022). TGA/DSC study to characterise and classify coal seams conforming to susceptibility towards spontaneous combustion. *International Journal of Mining Science and Technology*, *32*(1), 75-88. DOI: 10.1016/j.ijmst.2021.10.005

[2] Köferstein, R., & Ebbinghaus, S. G. (2013). Synthesis and characterization of nano-LaFeO3 powders by a soft-chemistry method and corresponding ceramics. *Solid State Ionics*, *231*, 43-48. DOI: 10.1016/j.ssi.2012.11.018.

[3] Hessien, M. M., Ali, M. A., El-Sayed, A. S., Awad, F. S., & El-Sadek, M. S. (2017). Structural, magnetic and sensing properties of lanthanum ferrite via facile sol gel oxalate precursor route. *Journal of Materials Science: Materials in Electronics*, *28*, 4170-4178. DOI: 10.1007/s10854-016-5914-9

[4] Jia, L., Lloyd, M. D., Lees, M. R., Huang, L., & Walton, R. I. (2023). Limits of solid solution and evolution of crystal morphology in (La1–xREx)FeO3 perovskites by low temperature hydrothermal crystallization. *Inorganic Chemistry*, *62*(11), 4503-4513. DOI: 10.1021/acs.inorgchem.3c00621

[5] Cullity, B. D. (1956). *Elements of X-ray diffraction*. Addison-Wesley Publishing.

[6] Taguchi, H., Masunaga, Y., Hirota, K., & Yamaguchi, O. (2005). Synthesis of perovskite-type (La1− xCax) FeO3 (0≤ x≤ 0.2) at low temperature. *Materials research bulletin*, *40*(5), 773-780. DOI: 10.1016/j.materresbull.2005.02.009.

[7] Kumar, A., & Sahay, P. P. (2022). Precursor-dependent spray-pyrolyzed Co3O4 thin films: Comparative results on their structural, optical, and electrical properties. *Brazilian Journal of Physics*, *52*(3), Article 101. DOI: 10.1007/s13538-021-01023-5.

[8] Narasimharao, K., & Kamaluddin, H. S. (2023). Adsorption of methylene blue and metachromasy over analcime zeolites synthesized by using different Al precursors. *Materials Today Chemistry*, *32*, 101675. DOI: 10.1016/j.mtchem.2023.101675

[9] Sarkar, P., Niranjan, N. K., Srivastava, A., Tripathy, S. K., Baishnab, K. L., & Chinnaiah, M. C. (2022). Comparative study on the role of different precursor salts on structural, morphological,

and optoelectronic characteristics of CH3NH3PbCl3 perovskite semiconductor: An experimental study. *Journal of Electronic Materials, 51*(12), 7105-7112. DOI: 10.1007/s11664-022-09561-7.

[10] Parida, K. M., Reddy, K. H., Martha, S., Das, D. P., & Biswal, N. (2010). Fabrication of nanocrystalline LaFeO3: An efficient sol–gel auto-combustion assisted visible light responsive photocatalyst for water decomposition. *International Journal of Hydrogen Energy, 35*(22), 12161-12168. DOI: 10.1016/j.ijhydene.2010.06.015.

[11] Hao, X., & Zhang, Y. (2017). Low temperature gel-combustion synthesis of porous nanostructure LaFeO3 with enhanced visible-light photocatalytic activity in reduction of Cr (VI). *Materials Letters, 197*, 120-122. DOI: 10.1016/j.matlet.2017.02.070.

[12] Andreola, F., Leonelli, C., & Romagnoli, M. (2000). Techniques used to determine porosity. *American Ceramic Society Bulletin, 79*(7), 49-52.

[13] Ahmad, I., Akhtar, M. J., & Siddique, M. (2016). Effects of Ni doping on the structural properties and collapse of magnetic ordering in NdFe1−xNixO3 (0.1≤ x≤ 0.7) orthoferrites. *Chinese Physics B, 25*(2), 028101. DOI: 10.1088/1674-1056/25/2/028101.

[14] Li, Q., & Yin, X. (2011). Effects of phase composition on microstructure and mechanical properties of Lu2O3-doped porous silicon nitride ceramics. *Journal of Materials Science & Technology, 27*(6), 529-533. DOI: 10.1016/S1005-0302(11)60098-1.

[15] Phokha, S., Pinitsoontorn, S., Maensiri, S., & Rujirawat, S. (2014). Structure, optical and magnetic properties of LaFeO 3 nanoparticles prepared by polymerized complex method. *Journal of sol-gel science and technology*, *71*, 333-341. DOI: 10.1007/s10971-014-3383-8.

[16] Khalil, K. M. S., Mahmoud, A. H., & Khairy, M. (2022). Formation and textural characterization of size-controlled LaFeO3 perovskite nanoparticles for efficient photocatalytic degradation of organic pollutants. *Advanced Powder Technology*, *33*(1), 103429. DOI: 10.1016/j.apt.2021.09.016.

[17] Phan, T. T. N., Dao, T. P., Luan, V. H., Tran, N. C., & Vu, T. Q. (2018). Optimizing photocatalytic performance of hydrothermally synthesized LaFeO3 by tuning material properties and operating conditions. *Journal of Environmental Chemical Engineering*, *6*(1), 1209-1218. DOI: 10.1016/j.jece.2017.11.044.

[18] Xu, Y. J., Liu, J., Wei, X., & Chen, S. (2021). Magnetic behavior, photocatalytic activity and gas-sensing performance of porous lanthanum ferrites powders. *Materials Chemistry and Physics*, *267*, 124628. DOI: 10.1016/j.matchemphys.2021.124628.

[19] Wiranwetchayan, O., Kaewkhao, J., Kothan, S., & Limsuwan, P. (2019). Characterization of perovskite LaFeO3 synthesized by microwave plasma method for photocatalytic applications. *Ceramics International*, *45*(4), 4802-4809. DOI: 10.1016/j. ceramint.2018.11.177.

[20] Shivakumara, C. (2006). Low temperature synthesis and characterization of rare earth orthoferrites LnFeO3 (Ln= La, Pr and Nd) from molten NaOH flux. *Solid State Communications*, *139*(4), 165-169. DOI: 10.1016/j.ssc.2006.05.011.

[21] Ismael, M., & Wark, M. (2019). Perovskite-type LaFeO3: photoelectrochemical properties and photocatalytic degradation of organic pollutants under visible light irradiation. *Catalysts*, *9*(4), 342. DOI: 10.3390/catal9040342.

[22] Manzoor, S., Bashir, M. S., Kausar, R., Rauf, A., & Khan, M. I. (2020). Structural, thermal, dielectric and multiferroic investigations on LaFeO3 composite systems. *Journal of Materials Science: Materials in Electronics, 31*, 7811-7830. DOI: 10.1007/s10854-020-03286-5.

Chapter V:

Adsorption and Photocatalytic Activities

The prepared $LaFeO_3$ powders were used as catalysts and photocatalysts for the degradation of the methylene blue dye. The first part of this chapter is devoted to the adsorption activity of the synthesized powders. The kinetic, isotherm, and thermodynamic adsorption studies were discussed in detail. The second part is dedicated to outlining the photocatalytic activity of the powders, where the obtained results were fitted to the first-order kinetic model. A proposed reaction mechanism was also investigated. The influence of the used precursor on the adsorption and photocatalytic activities was highlighted.

V.1 Experimental Procedure

V.1.1 Methylene Blue Preparation

Methylene blue dye was chosen to test the effectiveness of the prepared $LaFeO_3$ samples for adsorption and photocatalytic applications. A solution of 15 $mg.L^{-1}$ of methylene blue was prepared by dissolving 15 mg of methylene blue powder in 1 L of deionized water. This solution was diluted to the required concentrations during the elaboration of the MB calibration curve. The absorption measurements were performed at a maximum wavelength of 660 nm. A standard calibration curve of MB is illustrated in Figure V.1.

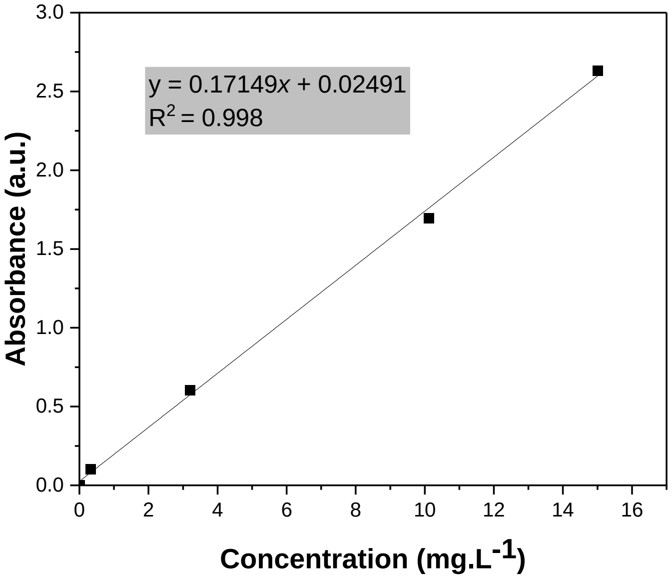

Figure V.1: Standard calibration curve of MB solution.

V.1.2 Determination of the Optimum Adsorbent Mass

The optimum adsorbent mass was obtained by varying the mass of the NLF2 and CLF3 samples from 5 to 80 mg. At ambient temperature, a fixed amount of the adsorbent (5, 15, 20, 40, 60, and 80 mg) was added to 100 mL of methylene blue with a concentration of 4.43 $mg.L^{-1}$ and pH of 6.47. The mixture was kept under magnetic stirring for 2h.

V.1.3 Point of Zero Charge (pH_{pzc})

In a given aqueous solution, the pH at a point of zero charge (pH_{PZC}) is described as the pH at which the net charge of the particle's surface is equal to zero [1], where the contribution of anions is equal to that of the cations. The determination of the PZC value is quite important and could help to assume the possible interactions between the adsorbent and the chemical spices of the adsorbate in the solution. The pH_{PZC} of our samples was determined by adding separately 20 mg of NLF2 and CLF3 powders to 100 mL of MB solution with pH adjusted between 3 and 11 using hydrochloric acid (HCl) and sodium hydroxide (NaOH). After 24h, the final pH of each sample was measured. Then we drew the graph (pH_i versus pH_f) and determined the pH_{pzc} value from the intersection between the initial pH and the final pH. The pH measurements of the different solutions were carried out using HI 2211 pH/ORP Meter by HANNA instruments.

V.1.4 Influence of the Contact Time

The influence of the contact time on the potential of the NLF1, NLF2 and CLF3 catalysts during the adsorption of MB dye was investigated by mixing, at room temperature, 20 mg of the catalyst with 100 mL of methylene blue solution with an initial concentration of 4.43 $mg.L^{-1}$ and pH 12 under magnetic stirring at constant stirring speed of 200 rpm. Each sample was centrifuged at 3000 rpm for 15 min and then the concentration of MB was analyzed by a UV-vis spectrometer.

The dye removal percentage R (%) and the adsorption capacity q_e ($mg.g^{-1}$) were determined using the following equations [2,3];

$$R(\%) = \frac{C_0 - C_e}{C_0} \times 100 \tag{V.1}$$

$$q_e = \frac{(C_0 - C_e)V}{m}, \tag{V.2}$$

where C_0 and C_e are the initial and equilibrium concentrations of MB (in $mg.L^{-1}$), respectively. m (g) is the adsorbent mass and V (L) is the volume of the used solution.

V.1.5 Adsorption Kinetics

To study the adsorption kinetics, the obtained data about MB molecules adsorption on $LaFeO_3$ surface were fitted to the pseudo-first-order (PFO), pseudo-second-order (PSO), Elovich, and intraparticle diffusion kinetic models. The corresponding mathematical equations of these four kinetic models are given in Table V.1 [2,3].

Table V.1: Linear equations of the pseudo-first-order “PFO”, pseudo-second-order “PSO”, Elovich, and intraparticle diffusion models.

Kinetics models	Linear form Equations	Parameters
PFO	$Ln\,(q_e - q_t) = -k_1 \cdot t + lnq_e$	q_e (mg.g^{-1}): Adsorption capacity at equilibrium, q_t (mg.g^{-1}): Capacity at time t (min). k_1 (min^{-1}): Rate constant
PSO	$\frac{t}{q_t} = \frac{1}{k_2 \cdot q_e^2} + \frac{1}{q_e} \cdot t$	k_2 (g.mg^{-1}.min^{-1}): Rate constant.
Elovich	$q_t = \frac{1}{\beta} \cdot ln\beta \cdot \alpha + \frac{1}{\beta} \cdot lnt$	α (mg.g^{-1}.min^{-1}): Initial adsorption β (g.mg^{-1}): Desorption rate constant.
Intraparticle diffusion	$q_t = k_{id} \cdot t^{0.5} + C_{id}$	k_{id} (mol.g^{-1}min$^{-1/2}$): Rate factor constant. C_{id} (mg.g^{-1}): Intraparticle diffusion constant.

V.1.6 Adsorption Isotherm

The adsorption isotherm of Methylene Blue (MB) on $LaFeO_3$ surfaces was studied at 297K by adding 20 mg of $LaFeO_3$ powder to 100 mL of MB solution of several initial concentrations (3.289, 6.619, 11.564 and 19.419 mg.L^{-1}). The pH of the solution was adjusted to 12. The dye concentrations before and after adsorption were measured using a UV-visible spectrometer at 660 nm. The obtained adsorption results were fitted to the well-known models; Langmuir and Freundlich models. The Langmuir isotherm model assumes monolayer adsorption with homogenous adsorption sites in terms of energy where the energetic properties of the adsorption sites are equivalent. Unlike the Langmuir isotherm, the Freundlich empirical model can be used for multilayer adsorption on heterogeneous sites. This model assumes that the adsorption heat distribution and affinities toward the heterogeneous surface are not uniform. The equations of both considered isotherm models are given in Table I.2 [4].

Table V.2: Mathematical formula of Langmuir and Freundlich models.

Isotherm model	Linear equation	Parameters description
Langmuir	$\frac{C_e}{q_e} = \frac{C_e}{q_m} + \frac{1}{q_m K_L}$	C_e: Concentration of adsorbate at equilibrium (mg.L^{-1}). K_L: Langmuir isotherm constant (L.mg^{-1}). q_m: Maximum adsorption capacity (mg.g^{-1}). q_e: Adsorption capacity at equilibrium (mg.g^{-1}).
Freundlich	$Log(q_e) = LogK_f + \frac{1}{n} LogC_e$	K_F: Freundlich isotherm constant. n: Adsorption intensity.

V.1.7 Adsorption Thermodynamics

The thermodynamics of MB adsorption on $LaFeO_3$ nanoparticles was studied for solution temperatures of 298, 308, 318 and 328K and MB concentration of 4.43 $mg.L^{-1}$. The thermodynamic parameters, including the standard Gibbs free energy (ΔG°), enthalpy (ΔH°), and entropy (ΔS°) were calculated using the equations (V.3) and (V.4) [4]:

$$\Delta G° = \Delta H° - T \cdot \Delta S° \qquad (V.3)$$

$$lnK_d = \frac{\Delta S°}{R} - \frac{\Delta H°}{RT}, \qquad (V.4)$$

where R is the gas constant (8.314 $J.mol.K^{-1}$), K_d is the thermodynamic equilibrium constant and T(K) is the absolute temperature.

The thermodynamic equilibrium constant, K_d, is determined using Eq (V.5) [2]

$$K_d = \frac{q_e}{C_e} \qquad (V.5)$$

V.1.8 Photocatalytic Study

The photodegradation tests of MB pigment by $LaFeO_3$ nanoparticles were performed by dispersing 20 mg of catalyst powder in 100 mL of MB solution at a pH of 12 and using a 120 W tungsten lamp as a source of visible light irradiation. Before starting the photodegradation experiment, the mixture (catalytic powder + MB solution) was kept in the dark at room temperature for 30 min under magnetic stirring to ensure the adsorption/desorption equilibrium. The photocatalytic experiment was carried out at room temperature using continuous circulation of cold water. At equal time intervals, samples were centrifuged at 3000 rpm for 15 min and analyzed with a UV–visible spectrometer.

The kinetics of MB photodegradation by $LaFeO_3$ nanoparticles were fitted to the pseudo-first-order rate equation given as follows [5]:

$$ln\left(\frac{C}{C_0}\right) = -k_{app} \times t \qquad (V.6)$$

where C represents the dye concentration at time t, C_0 is the initial dye concentration, and k_{app} is the first-order rate constant.

V.2 Results and Discussion

V.2.1 Determination of the Optimum Adsorbent Mass

The variation of adsorption capacity as a function of the $LaFeO_3$ samples is illustrated in Figure V.2. From this Figure, it can be seen that the adsorption rate increases rapidly with increasing catalyst mass, which can be attributed to the existence of additional adsorption sites thus allowing the adsorption of more MB molecules on the catalyst surface, and therefore the adsorption efficiency improved. It is found that the adsorption saturation is reached for 20 mg of $LaFeO_3$ powder. This optimal mass of $LaFeO_3$ powder was considered in all the adsorption and photocatalytic experiments.

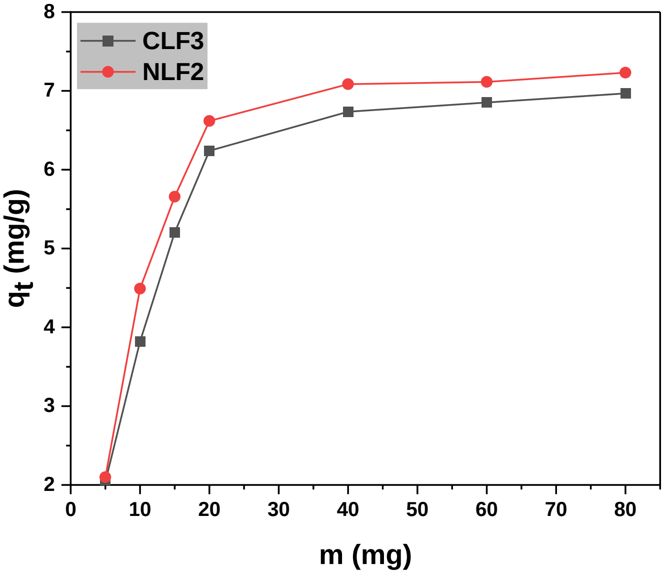

Figure V.2: Adsorbent mass effect on the adsorption capacity of the NLF2 and CLF3 samples (MB concentration is 4.43 $mg.L^{-1}$ at pH of 6.47).

V.2.2 pH_{PZC} Determination

Figure V.3 displays the pH_i versus pH_f plots for the NLF2 and CLF3 samples. The value of pH_{pzc} is found to be equal to 6.78 for NLF2 and 6.33 for CLF3. Note here that the surface of the $LaFeO_3$ powders is negatively charged for $pH > pH_{PZC}$, which could be attributed to the dominance of the hydroxyl group OH^-. The presence of OH^- can provide a strong interaction of the catalyst surface with the MB^+ cation, which promotes the adsorption of the dye. Otherwise, if pH is lower than pH_{PZC}, the surface of the adsorbent becomes negatively charged, which prevents the attraction between the pollutant and the catalyst surface containing oxygenated functional groups (C-O, C=O, and O-H) thus leading to low adsorption [5].

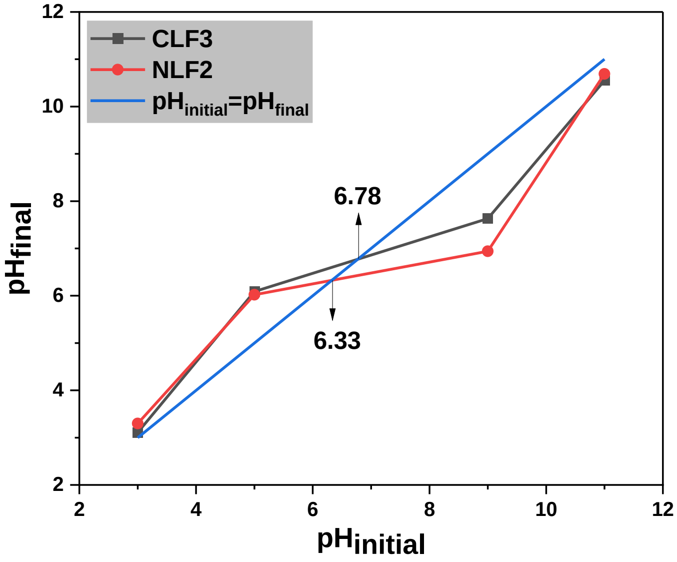

Figure V.3: The pH_{pzc} of the NLF2 and CLF3 samples using 20 mg of the catalyst, 100 mL of 4.43 mg.L^{-1} MB solution at pH of 12.

V.2.3 Effect of Contact Time

The evolution of the capacity of samples NLF1, NLF2 and CLF3 to adsorb MB molecules in a contact time interval of 0 to 60 min is illustrated in Figure V.4.a. A rapid increase in adsorption capacity is observed during the first 30 minutes of contact time for the three considered samples, then the variation becomes moderate. The reason for this rapid increase in the adsorption capacity between 0-30 min of the contact time is that all the adsorbent sites are vacant, where there is a significant difference in solute concentration between the adsorbent surface and the bulk solution that leads to high mass transfer onto the adsorbent surface. The adsorption process reaches saturation after 30 min of contact time. Figure V.4.b depicts the dye removal efficiency as a function of contact time for the three considered samples, where the inset highlights the values reached within 60 min of contact time. The maximum adsorption efficiency R (%) is reached after 60 min of contact time, approximately 42.3, 45.7, and 47.8% for NLF1, NLF2, and CLF3, respectively. The removal efficiency of MB dye increases in the same order as the porosity of the powder.

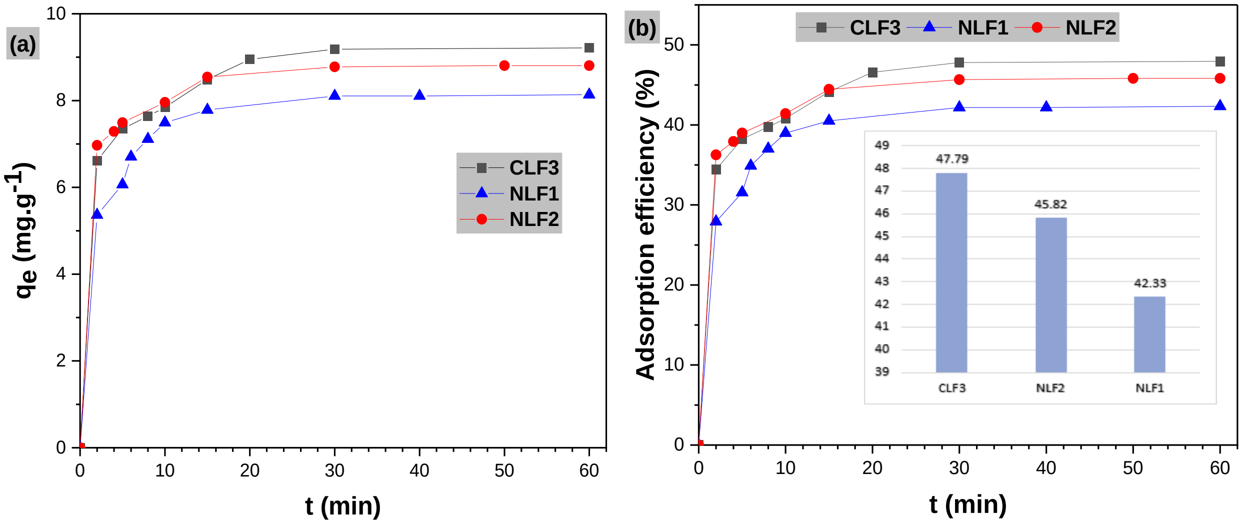

Figure V.4: (a) Effect of contact time on the adsorption of MB on NLF1, NLF2 and CLF3 samples and (b) adsorption efficiency.

V.2.4 Adsorption Kinetics

The importance of the adsorption kinetics study lies in determining the efficiency of the adsorption process as well as identifying the type of adsorption mechanism involved. As previously mentioned, four kinetic models are considered to model the adsorption kinetics. The adsorption kinetic plots of the NLF1, NLF2, and CLF3 samples are displayed in Figure V.5.

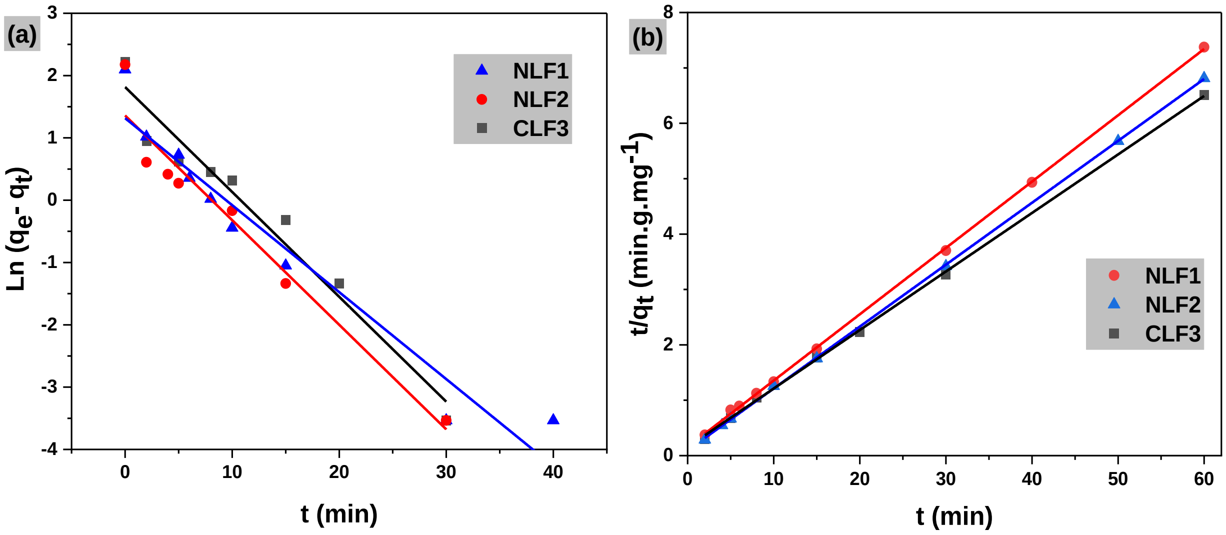

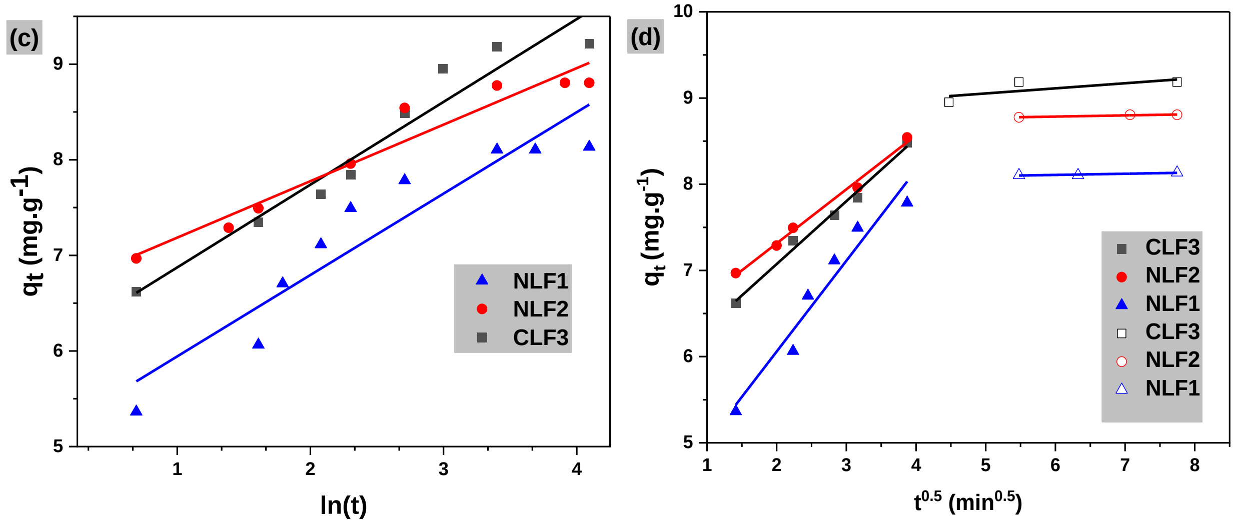

Figure V.5: (a) Pseudo-first-order, (b) pseudo-second-order (c) Elovich and (d) intraparticle diffusion models for the adsorption of MB on NLF1, NLF2 and CLF3 powders.

From the plots illustrated in Figure V.5 and the numerical data given in Table V.3, it can be seen that the pseudo-second-order model fits the experimental results better than the pseudo-first-order model, giving the highest correlation coefficient R^2 (equal to 0.99977, 0.9999 and 0.99943 for NLF1, NLF2, and CLF3, respectively). The pseudo-second-order kinetic model revealed a superlative fit to the experimental data. In addition, the experimental values of the adsorption capacity (q_e = 8.135, 8.834, and 9.213 mg.g^{-1} for NLF1, NLF2, and CLF3, respectively) agree well with those obtained from the PSO model (8.351, 8.947 and 9.465 mg.g^{-1} for NLF1, NLF2, and CLF3, respectively). Therefore, from the above results, it can be concluded that the adsorption of MB on $LaFeO_3$ samples follows the pseudo-second-order model, which means that the adsorption capacity is proportional to the number of active sites located on the surface of the $LaFeO_3$ adsorbent [3]. The high adsorption capacity of the CLF3 sample compared to that of NLF1 and NLF2 can be attributed to its special surface morphology and higher porosity.

On the other hand, the Elovich model is widely used to describe the chemical adsorption process and is more appropriate for systems with heterogeneous adsorbing surfaces [6]. Considering the low values of R^2 and the non-linearity of the Elovich plots, we can note that this model does not agree well with our experimental results and therefore the adsorption of MB is not completely dominated by the chemisorption process.

Table 3: The estimated kinetic parameters of the MB dye adsorption on NLF1, NLF2, and CLF3 samples.

Kinetics model	**Parameters**		
	NLF1	**NLF2**	**CLF3**
PFO	R^2= 0.93888 k_1=0.13961 q_e=3.73079	R^2= 0.94567 k_1=0.16791 q_e=3.8921	R^2= 0.95751 k_1=0.16832 q_e=6.14581
PSO	R^2= 0.99977 k_2=0.0912 q_e=8.3514	R^2= 0.9999 k_2=0.1323 q_e=8.9469	R^2= 0.99943 k_2=0.0721 q_e=9.4652
Elovich	R^2= 0.88524 α=336.7014 β=1.1744	R^2= 0.9436 α=41450.2938 β=1.6921	R^2= 0.94203 α=893.6741 β=1.15501
Intraparticle diffusion	R_1^2= 0.9889 k_{id1}=0.72938 C_{id1}=5.61502 R_2^2= 0.54248 k_{id2}=0.05914 C_{id2}=8.75754	R_1^2=0.99212 k_{id1}=0.62713 C_{id1}=6.05948 R_2^2= 0.9161 k_{id2}=0.01383 C_{id2}=8.70188	R_1^2= 0.94365 k_{id1}=1.05309 C_{id1}=3.95268 R_2^2= 0.86343 k_{id2}=0.01364 C_{id2}=8.02622

Figure V.5.d illustrates the intraparticle diffusion kinetic model, which is represented by the relation between q_t and $t^{0.5}$ and is considered to highlight the type of diffusion mechanism occurring during the adsorption process. The plots in Figure V.5.d exhibit two types of linearity, signifying two successive stages of diffusion during the adsorption process. The first stage, considered the fastest, indicates the adsorption or mass transfer of MB molecules onto the external surface of the adsorbent (external diffusion). In the second step, a slow and progressive intraparticle diffusion occurs where the adsorbed molecules diffuse into the internal pores of the catalyst [7]. This indicates that the adsorption process is not limited to the surface of the catalyst but also reaches deeper levels when adsorbing MB molecules in $LaFeO_3$ powders. The adsorption takes place at different adsorption rates, where k_{id1} is greater than k_{id2}, which can be explained by the resistance to diffusion leading to the decrease of the rate constant. We can therefore say that the adsorption is predominantly due to the porous structure and the existence of nanopores dispersed over the whole of the catalyst surface, signifying that porous diffusion was involved in the adsorption of MB on CLF3 powder. In conclusion, based on the four considered models, the adsorption process of MB molecules on $LaFeO_3$ nanoparticles depends more on the vacant active sites and the intraparticle diffusion.

V.2.5 Adsorption Isotherms

The study of adsorption isotherm provides information about the adsorption system and process, the surface properties of the adsorbent, and also the way the adsorbate is adsorbed on the adsorbent surface could be interpreted through this study [8,9]. The isotherm plots and corresponding parameters for MB adsorption on the $LaFeO_3$ surface are displayed in Figure V.6 and Table V.4, respectively.

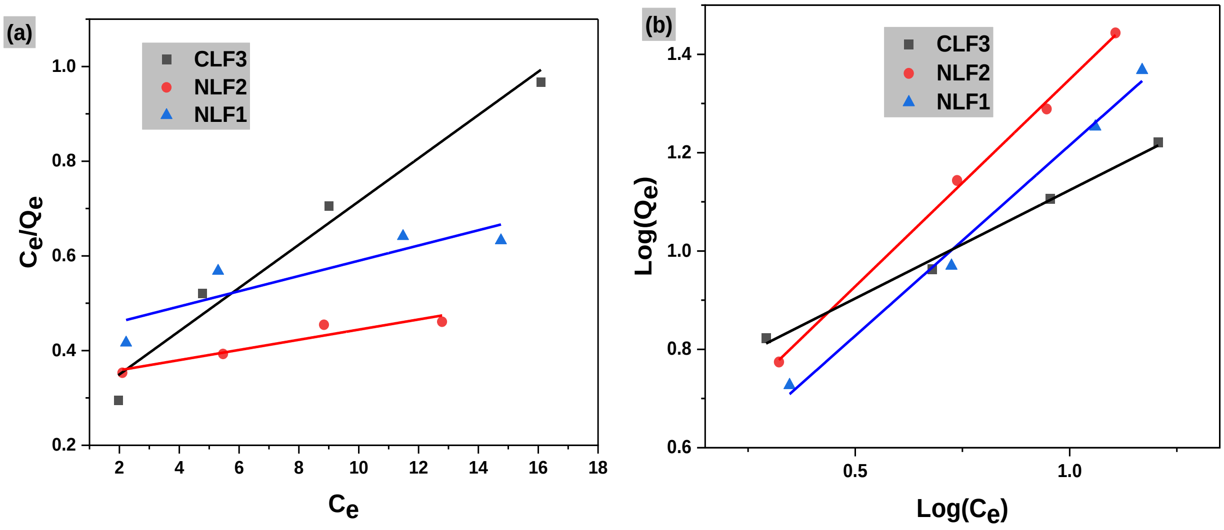

Figure V.6: Linear isotherms of the NLF1, NLF2 and CLF3 samples: (a) Langmuir and (b) Freundlich.

According to the plots of Figure V.6 together with the collected data in Table V.4, one can deduce that the adsorption process follows the Freundlich isotherm due to the high values of the correlation coefficient (0.99223, 0.99799, and 0.99391 for the NLF1, NLF2 and CLF3 samples, respectively). Therefore, this is an indicating that the adsorption of MB molecules on $LaFeO_3$ occurred in a multilayer. The estimated values of the adsorption intensity, *n*, are 1.2908, 1.187, and 2.2702 for the NLF1, NLF2, and CLF3, respectively, which is greater than unit, proposing favorable adsorption [10]. The heterogeneity of the adsorbent surface, according to the Freundlich model, is defined by the value of *n*; where larger values of *n* refer to more heterogenous systems [11,12]. The obtained values of *n* suggest that the surfaces are slightly heterogeneous which is consistent with the non-suitability of the Elovich model.

Table V.4: Isotherm parameters for the adsorption of MB on the $LaFeO_3$ surface.

Isotherm model	Parameters		
	NLF1	NLF2	CLF3
Langmuir	Q_{max}= 62.112 K_L= 0.0367 R^2= 0.77991	Q_{max}=93.1966 K_L=0.0318 R^2= 0.90627	Q_{max}= 21.901 K_L= 0.1767 R^2= 0.97228
Freundlich	n= 1.2908 K_f= 2.7562 R^2= 0.99243	n= 1.1873 K_f= 3.2136 R^2= 0.99799	n= 2.2702 K_f= 4.8227 R^2= 0.99391

V.2.6 Adsorption Thermodynamics

The values of the thermodynamic parameters (ΔH°, ΔS°, and ΔG°), corresponding to the MB adsorption on $LaFeO_3$ samples, are listed in Table V.5. ΔH° and ΔS° were estimated from the slope and intercept of the plot 1/T versus ln(K_d), respectively (see Figure V.7), while ΔG° was calculated using Eq (V.3).

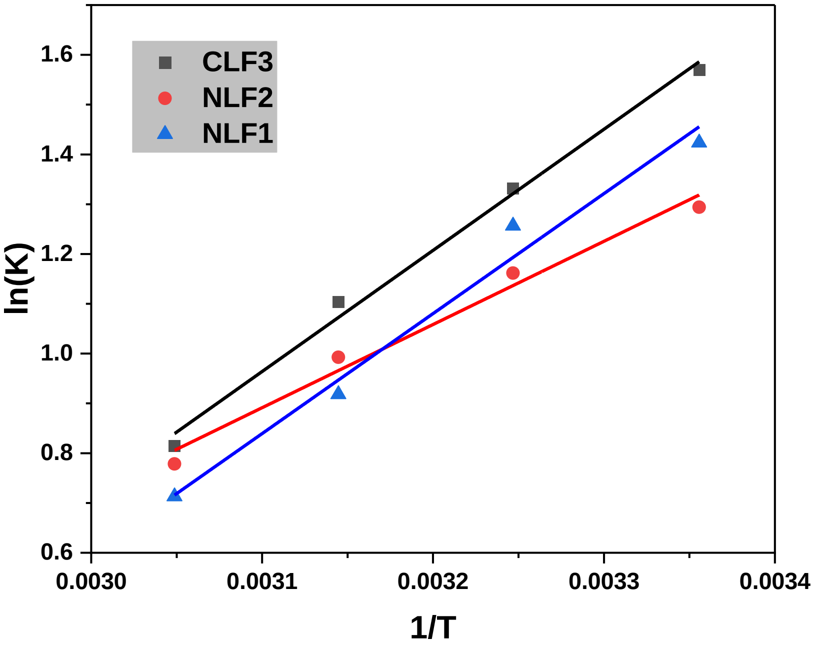

Figure V.7: Graph of 1/T versus ln(K) in the adsorption of MB using NLF1, NLF2 and CLF3 samples.

The negative values of ΔG° (as shown in Table V.5) indicate that the adsorption of MB on $LaFeO_3$ is spontaneous. In addition, the increase of ΔG° with increasing temperature suggests that the adsorption process is more favorable at low temperatures. The ΔH° values (equal to -13.893, -20.036, and -20.228 $kJ.mol^{-1}$ for the NLF1, NLF2, and CLF3 samples, respectively) reveal the exothermic and physical nature of the adsorption process. Moreover, the small negative values of the entropy (ΔS° equal to -0.0357, -0.0551, and -0.0547 $kJ.mol^{-1}$ for the NLF1, NLF2, and CLF3 samples, respectively) indicate a diminution in the randomness/ or irregularity at the solid/solution interface where there is no significant change in the internal structure of the adsorbent during the adsorption process [13,14].

Table V.5: Thermodynamic parameter values of MB adsorption on NLF1, NLF2, and CLF3 samples.

Sample	**ΔH° (kJ/mol)**	**ΔG° (kJ/mol)**				**ΔS° (kJ/mol)**
		298 (K)	308 (K)	318 (K)	328(K)	
NLF1	-13.893	-3.267	-2.910	-2.554	-2.197	-0.0357
NLF	-20.036	-3.606	-3.055	-2.504	-1.952	-0.0551
CLF3	-20.228	-3.930	-3.383	-2.836	-2.289	-0.0547

V.2.7 Photocatalytic Activity Study

The absorbance spectra of the NLF1, NLF2 and CLF3 samples were measured for several selected irradiation times between 0 – 40 min in order to study their efficiency for the photodegradation of MB dye under visible light irradiation. Figure V.8 illustrates the obtained results. The evolution of the MB degradation spectra with time of the three selected samples demonstrates the high dependence of the photocatalytic efficiency of $LaFeO_3$ powders on their preparation route, i.e. precursor choice. After 40 min of the photodegradation experiment, the efficiency of the MB solution discoloration reaches 85.0, 89.2 and 100% in the presence of NLF1, NLF2 and CLF3 powders, respectively (see Figure V.8.d). It was detected that the initial intense blue color of the MB solution gradually disappears and the solution becomes colorless after 40 min, particularly for the case of CLF3 (see the inset in Figure V.10).

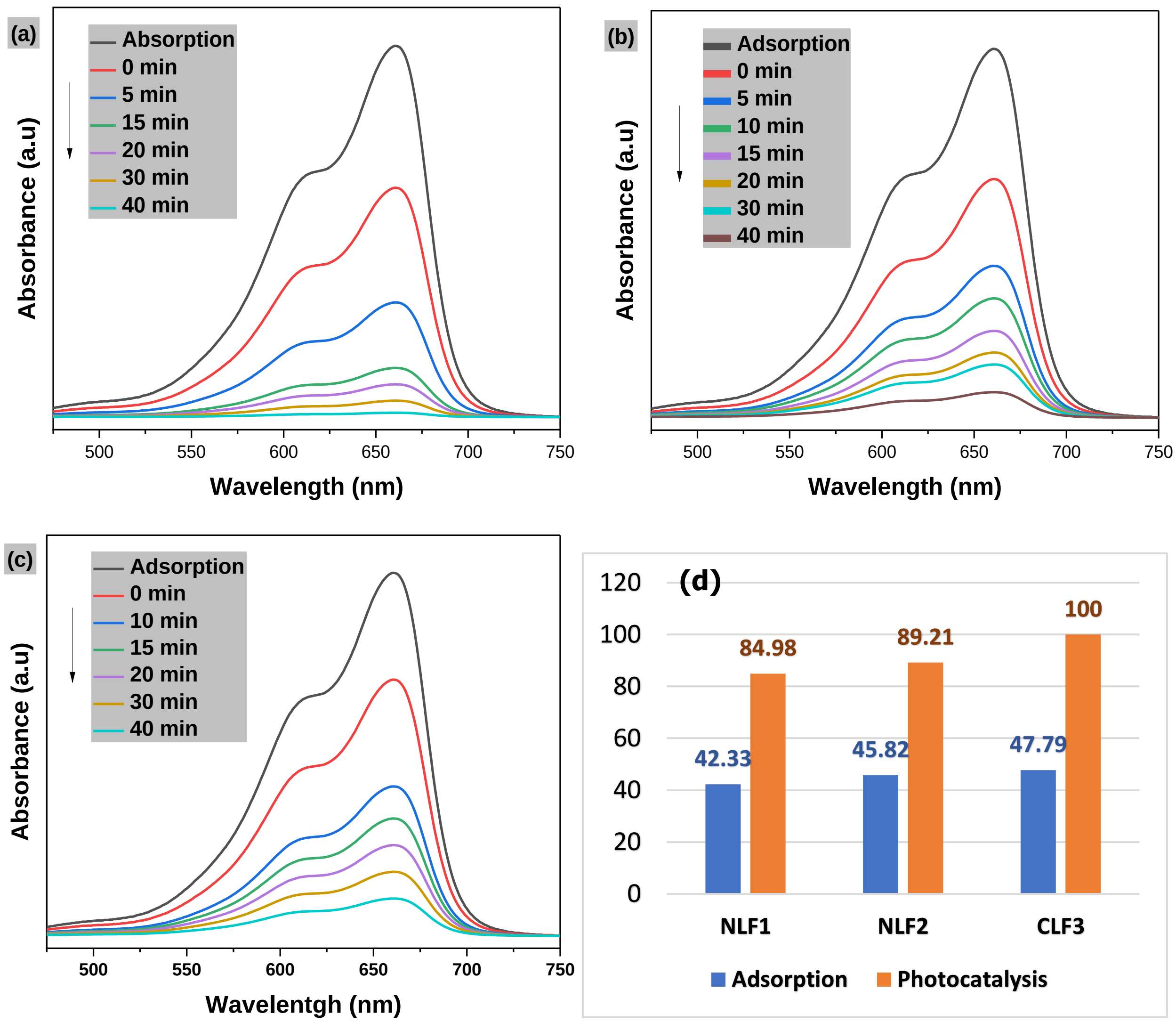

Figure V.8: Absorbance spectra of MB solution for several time irradiation by visible light in the presence of $LaFeO_3$ powders: (a) CLF3, (b) NLF2, (c) NLF1. Panel (d) represents the degradation efficiency of MB in the presence of the $LaFeO_3$ powder.

The CLF3 sample exhibits a high photocatalytic performance compared to the NLF1 and NLF2 samples, which can be mainly attributed to the nanopores that already ensured adsorption in the dark by acting as traps for MB molecules and also to the relatively small band gap ~2.19 eV, which provides a high number of photogenerated electrons under visible light irradiation. Table V.6 demonstrates the strong photocatalytic activity of the as-synthesized samples, NLF1, NLF2 and CLF3, compared to that of other photocatalysts reported in previous studies [15-18].

Table 4: The obtained removal efficiency of MB dye using $LaFeO_3$ powder, compared to those obtained previously using other catalysts.

Catalyst	**Dye concentration**	**Irradiation type**	**Contact time**	**Removal (%)**
Present work	20mg of CLF3, 4.43 $mg.L^{-1}$,100mL	120W lamp	40 min	100
	20mg of NLF1, 4.43 $mg.L^{-1}$,100mL			84.98
	20mg of NLF2, 4.43 $mg.L^{-1}$,100mL			89.21
$LaFeO_3/CeO_2$ [16]	15mg, $10^{-5}mol.L^{-1}$, 15mL	500 W Xe lamp	150min	95.9
$LaFeO_3$ ribbon-like nanofibers [17]	0.1g, 5mg/L, 50mL	High-pressure fluorescent Hg lamp (125 W)	120min	59.79
Cu-doped V_2O_5 [15]	20mg, 10ppm, 100mL	Visible light	90 min	95.4
Mc−Co_3O_4 [18]	10mg, 10 mg/L, 100mL	Natural sunlight irradiation	300 min	88

The plots of C/C_0 and $\ln(C/C_0)$ against irradiation time for the considered samples are depicted in Figure V.9. The modeling of the photocatalytic results of the three samples were all in accordance with the first-order kinetic equation which is validated by the R^2 values (0.99395, 0.98191 and 0.97479 for NLF1, NLF2 and CLF3, respectively). The k_{app} values were determined by fitting the $\ln(C/C_0)$ vs t data to equation (V.6) and they are equal to 0.05757, 0.07005 and 0.16041 min^{-1} for NLF1, NLF2 and CLF3, respectively. The CLF3 sample shows the highest rate, approximately more than twice that of NLF1 and NLF2. This result can be attributed to numerous factors, including; (i) the relatively low band gap of 2.19 eV which provides a larger number of photogenerated electrons under visible light irradiation [18,20], (ii) the high porosity of the CLF3 sample provides more sites for photocatalytic reactions, (iii) the porous structure ensures a high scattering and trapping of the incident light photons, which can consequently result in raising the generation of electron-hole pairs that is the essential factor in photocatalytic reactions, and (iv) the good crystallinity that prevents the rapid recombination of electrons and holes [19,20].

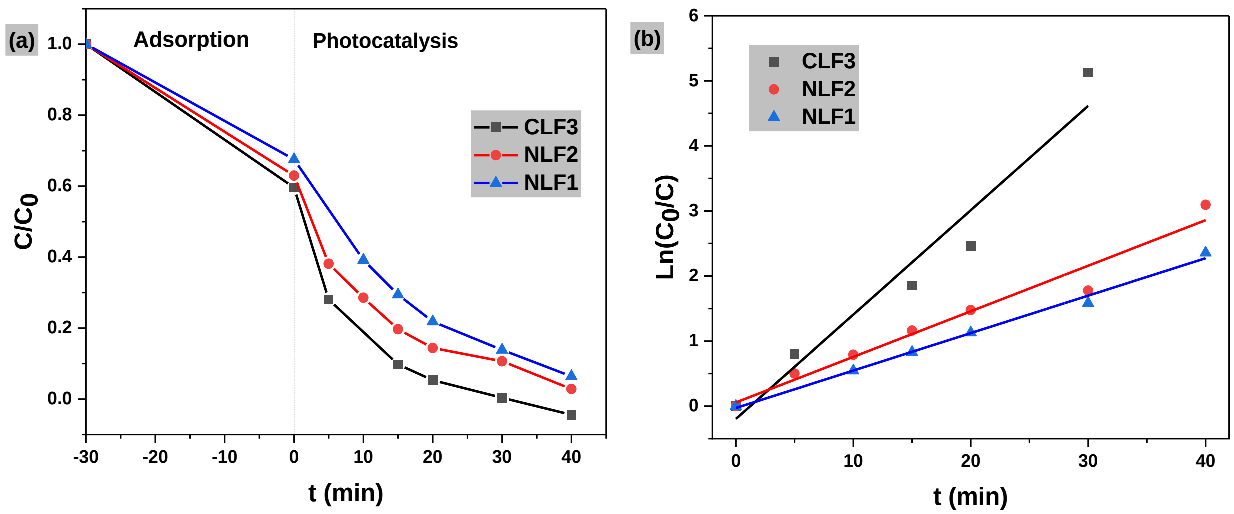

Figure V.9: (a) The photo-degradation activity of $LaFeO_3$ nanoparticles, (b) first-order kinetics of NLF1, NLF2 and CLF3 catalysts.

Figure V.10 illustrates the proposed photodegradation process of methylene blue dye in the presence of $LaFeO_3$ photocatalyst. Upon the visible light irradiation of $LaFeO_3$ powder, electrons (e^-) are released from the valence band (VB) to the conduction band (CB), leaving holes (h^+) in the VB (Eq. V.6) [5,16]. The generated e^- and h^+ are then transferred to the surface of the photocatalyst. Electrons in the CB react with dissolved oxygen molecules O_2 forming superoxide anion radicals ($O^{2-}\bullet$) (Eq. V.7), while h^+ ions react with H_2O to form the hydroxyl radicals •OH (Eq. V.8) [5]. The produced radical species ($\bullet O^{2-}$ and •OH) favor the conversion of MB molecules into non-toxic products (Eq. V.9), such as CO_2, H_2O, SO_4^{2-} and NH^{4+}. Due to the high oxidation potentials of the holes (h^+), they can directly attack the MB dye and degrade it [21], which permits the direct oxidation of the dye (Eq. V.9). Therefore, the MB dye solution converts into a colorless solution due to the degradation of the aromatic rings.

$$\mathrm{LaFeO_3} + hv \rightarrow \mathrm{LaFeO_3(e^- + h^+)} \qquad \text{(V.6)}$$

$$\mathrm{O_2} + \mathrm{LaFeO_3(e^-)} \rightarrow \mathrm{O_2^-}\bullet \qquad \text{(V.7)}$$

$$\mathrm{H_2O} + \mathrm{LaFeO_3(h^+)} \rightarrow OH\bullet + H^+ \qquad \text{(V.8)}$$

$$\mathrm{MB} + \mathrm{OH}\bullet, \mathrm{O_2^-}, \mathrm{h^+} \rightarrow \mathrm{CO_2} + \mathrm{H_2O} + \text{nontoxic products} \qquad \text{(V.9)}$$

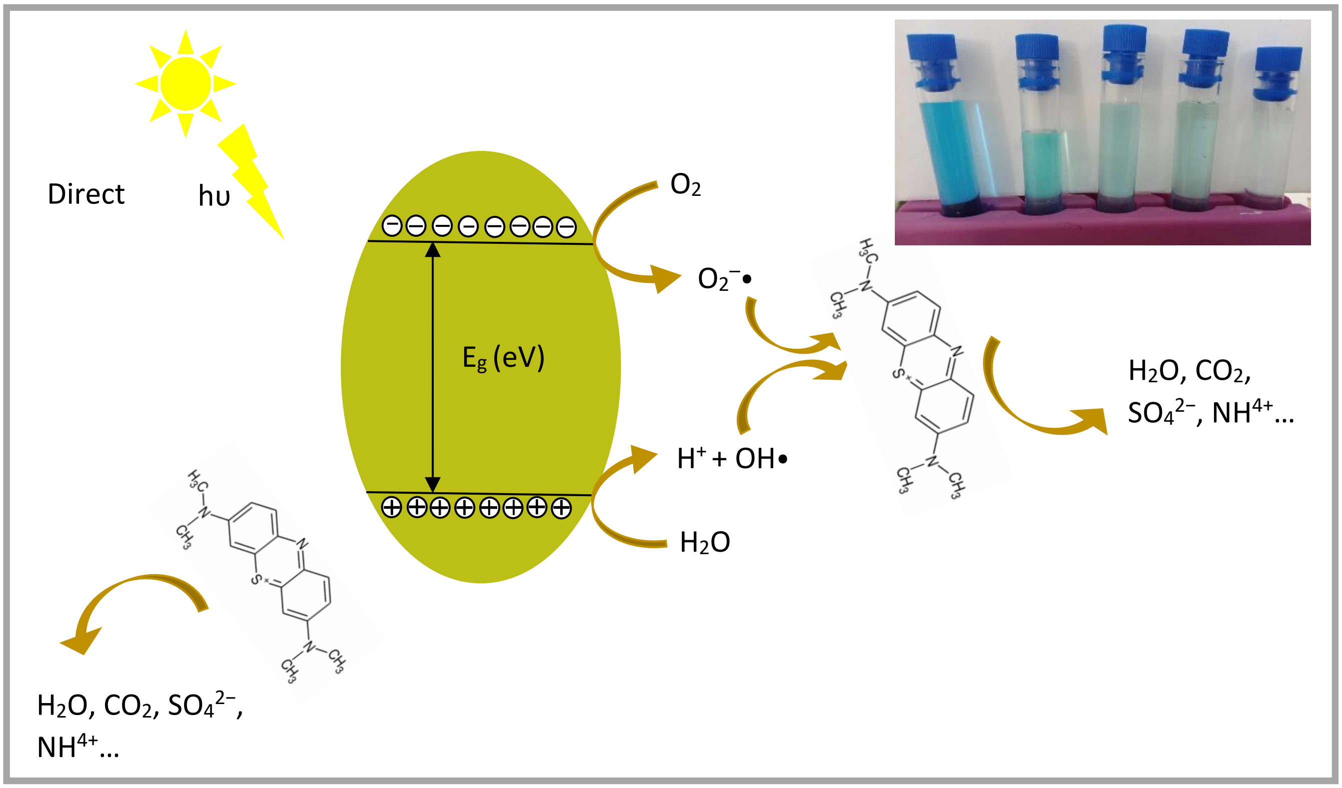

Figure V.10: Possible photocatalytic mechanism of MB degradation under visible light irradiation in the presence of the $LaFeO_3$ nanoparticles.

References

[1] Yusuff, A. S. (2019). Adsorption of hexavalent chromium from aqueous solution by Leucaena leucocephala seed pod activated carbon: Equilibrium, kinetic and thermodynamic studies. *Arab Journal of Basic and Applied Sciences, 26*(1), 89-102. DOI: 10.1080/25765299.2019.1581659.

[2] Neolaka, Y. A. B., Lawa, Y., Naat, N., Riwu, A. A. P., & Darmokoesoemo, H. (2020). The adsorption of Cr (VI) from water samples using graphene oxide-magnetic (GO-Fe3O4) synthesized from natural cellulose-based graphite (kusambi wood or Schleichera oleosa): Study of kinetics, isotherms and thermodynamics. *Journal of Materials Research and Technology, 9*(3), 6544-6556. DOI: 10.1016/j.jmrt.2020.03.071.

[3] Wang, J., & Guo, X. (2020). Adsorption kinetic models: Physical meanings, applications, and solving methods. *Journal of Hazardous Materials, 390*, 122156. DOI: 10.1016/j.jhazmat.2020.122156.

[4] Tran, H. N., You, S. J., Hosseini-Bandegharaei, A., & Chao, H. P. (2021). Thermodynamic parameters of liquid–phase adsorption process calculated from different equilibrium constants related to adsorption isotherms: A comparison study. *Journal of Environmental Chemical Engineering, 9*(6), 106674. DOI: 10.1016/j.jece.2021.106674.

[5] Ismael, M., & Wark, M. (2019). Perovskite-type LaFeO3: photoelectrochemical properties and photocatalytic degradation of organic pollutants under visible light irradiation. *Catalysts, 9*(4), 342. DOI: 10.3390/catal9040342.

[6] Wu, F.-C., Tseng, R.-L., & Juang, R.-S. (2009). Characteristics of Elovich equation used for the analysis of adsorption kinetics in dye-chitosan systems. *Chemical Engineering Journal, 150*(2-3), 366-373. DOI: 10.1016/j.cej.2009.01.014.

[7] Gemeay, A. H., El-Sonbati, A. Z., El-Bindary, A. A., & El-Demerdash, S. H. (2020). Chemical insight into the adsorption of reactive wool dyes onto amine-functionalized magnetite/silica core-shell from industrial wastewaters. *Environmental Science and Pollution Research, 27*, 32341-32358. DOI: 10.1007/s11356-020-09539-4.

[8] Mesbah, M., Belarbi, L., Karima, S., Merabet, D., & Bouzaza, A. (2020). Hydrothermal synthesis of LaFeO3 nanoparticles adsorbent: Characterization and application of error functions for adsorption of fluoride. *MethodsX, 7*, 100786. DOI: 10.1016/j.mex.2020.100786.

[9] Aigbe, U. O., Omoniyi, A. O., Ekebafe, L. O., & Benson, A. U. (2021). Fly ash-based adsorbent for adsorption of heavy metals and dyes from aqueous solution: a review. Journal of Materials Research and Technology, 14, 2751-2774. DOI: 10.1016/j.jmrt.2021.07.030.

[10] Khan, T. A., Chaudhry, S. A., & Ali, I. (2015). Equilibrium uptake, isotherm and kinetic studies of Cd (II) adsorption onto iron oxide activated red mud from aqueous solution. *Journal of Molecular Liquids*, *202*, 165-175. DOI: 10.1016/j.molliq.2014.12.053.

[11] Neolaka, Y. A. B., Lawa, Y., Naat, N., Riwu, A. A. P., Darmokoesoemo, H., & Lawa, Z. (2020). A Cr (VI)-imprinted-poly (4-VP-co-EGDMA) sorbent prepared using precipitation polymerization and its application for selective adsorptive removal and solid phase extraction of Cr (VI) ions from electroplating industrial wastewater. *Reactive and Functional Polymers*, *147*, 104451. DOI: 10.1016/j.reactfunctpolym.2019.104451.

[12] Lesmana, S. O., Febrianto, J., Soetaredjo, F. E., Sunarso, J., & Ismadji, S. (2009). Studies on potential applications of biomass for the separation of heavy metals from water and wastewater. *Biochemical Engineering Journal*, *44*(1), 19-41. DOI: 10.1016/j.bej.2008.12.009.

[13] Sahmoune, M. N. (2019). Evaluation of thermodynamic parameters for adsorption of heavy metals by green adsorbents. *Environmental Chemistry Letters*, *17*(2), 697-704. DOI: 10.1007/s10311-018-00835-w.

[14] Neolaka, Y. A. B., Lawa, Y., Naat, N., Riwu, A. A. P., Darmokoesoemo, H., & Naat, K. (2021). Indonesian Kesambi wood (Schleichera oleosa) activated with pyrolysis and H2SO4 combination methods to produce mesoporous activated carbon for Pb (II) adsorption from aqueous solution. *Environmental Technology & Innovation*, *24*, 101997. DOI: 10.1016/j.eti.2021.101997.

[15] Reddy, C. V., Suresh, P., Pasha, S. R., & Rajasekhar Reddy, G. (2023). Highly efficient photodegradation of toxic organic pollutants using Cu-doped V2O5 nanosheets under visible light. *Chemosphere*, *311*, 137015. DOI: 10.1016/j.chemosphere.2022.137015.

[16] Li, L., Wang, Y., Zhang, H., & Liu, Z. (2022). Ultrasonic-assisted synthesis of LaFeO3/CeO2 heterojunction for enhancing the photocatalytic degradation of organic pollutants. *Materials Science in Semiconductor Processing, 152*, 107058. DOI: 10.1016/j.mssp.2022.107058.

[17] Li, S., Zhang, H., Chen, Y., Wang, X., & Wang, L. (2020). Fabrication and photocatalytic activity of LaFeO3 ribbon-like nanofibers. *Journal of the Chinese Chemical Society*, *67*(6), 990-997. DOI: 10.1002/jccs.202000127.

[18] Vinayagam, R., Swaminathan, M., Arumugam, G., & Karuppasamy, M. (2023). Green synthesized cobalt oxide nanoparticles with photocatalytic activity towards dye removal. *Environmental Research, 216*, 114766. DOI: 10.1016/j.envres.2022.114766.

[19] Wiranwetchayan, O., Kaewkhao, J., Kothan, S., & Limsuwan, P. (2019). Characterization of perovskite LaFeO3 synthesized by microwave plasma method for photocatalytic applications. *Ceramics International, 45*(4), 4802-4809. DOI: 10.1016/j.ceramint.2018.11.177.

[20] Yahya, N., Yusuf, N., Deraman, M. M., Lee, H. S., & Mamat, M. H. (2021). Impacts of annealing temperature on morphological, optical and photocatalytic properties of gel-combustion-derived LaFeO3 nanoparticles. *Arabian Journal for Science and Engineering, 46*, 6153-6165. DOI: 10.1007/s13369-021-05488-3

[21] Khan, I., Ahmad, A., Khan, A., Abro, R., & Bilal, M. (2022). Review on methylene blue: Its properties, uses, toxicity and photodegradation. *Water, 14*(2), 242. DOI: 10.3390/w14020242.

Chapter VI:

DFT Calculation of $LaFeO_3$ Properties and MB Adsorption

The present chapter outlines the details of the methodology used to investigate the bulk and surface properties of $LaFeO_3$ and the obtained results. The first section involves a brief description of the computational details. The second section is devoted to the presentation and the discussion of the obtained results concerning the structural and electronic properties of the bulk $LaFeO_3$ and surface calculations. The MB adsorption on (121) and (100) surfaces was investigated in the last section of the chapter, where a discussion of the adsorption properties, including the adsorption energy, the adsorbent-adsorbate distance, and the estimated interactions involved during the adsorption process are presented.

VI.1 Computational Details

VI.1.1 Computational Method for Bulk $LaFeO_3$

All bulk calculations were performed using the CASTEP code in the Material Studio package. Spin-polarized calculations were performed using OTFG ultra soft pseudopotential via the conjugated gradient approximation GGA. The Perdew-Burke-Ernzerhof (PBE) exchange-correlation functional was used. A cutoff energy of 700 eV with Monkhorst-Pack k-points of 7×7×5 (corresponding to 123 k-points in the Irreducible Brillouin Zone (IBZ)) were considered. For the density of state (DOS) calculations, Monkhorst-Pack k-points of 8×8×6 were used. The equilibrium geometries were obtained by minimizing the total energy and internal forces using the Broyden–Fletcher–Goldfarb–Shanno (BFGS) algorithm. For all calculations, the G-type antiferromagnetic (G-AFM) configuration, illustrated in Figure VI.1, was chosen based on previous results demonstrating that G-AFM is the most energetically stable structure [1-3]. The strong electron correlation of iron atoms was treated using the Hubbard U correction through GGA+U calculation with U = 4.5 eV for all the Fe -*3d* orbitals. The value of Hubbard term was chosen taking into account the previously reported band gap of $LaFeO_3$, ranging between 2.1 and 2.6 eV [4-6], also, this value was consistent with previously used one that provides similar bandgap values [7-9]. The Hubbard correction was not taken into consideration for the La -*5d* electrons because they are deep in the La atoms besides the small influence of these states on the band gap. The considered valence electron configurations are $5s^2$ $5p^6$ $5d^1$ $6s^2$ for La, $3p^6$ $3d^6$ $4s^2$ for Fe, and $2s^2$ $2p^4$ for O atom. Accuracy in determining the equilibrium geometries was ensured by the consideration of the tolerance on the total energy of 10^{-5} eV/atom, maximum force of 0.03 eV/Å and maximum ion displacement less than 0.001 Å and a maximum stress amplitude is 0.05 GPa.

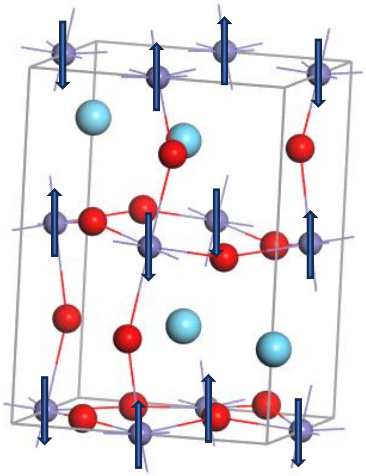

Figure VI.1: Spin directions of Fe atoms for the G-type antiferromagnetic configuration of $LaFeO_3$ (La: blue, Fe: purple, O: red).

VI.1.2 Computational Method for $LaFeO_3$ Surface

The surface properties calculations were performed within spin-polarized generalized gradient approximation within the Perdew-Burke-Ernzerhof *(*PBE*)* functional [10] as implemented within the Dmol^3 package [11]. An all-electron core treatment and double numerical plus d-functions (DND) basis set [12] were employed to extend the atomic wave function with a medium global cutoff energy. Using the standard Monkhorst-Pack special grids, the integration of the Brillouin zone was carried out with 1 × 1 × 1 k-points (at G-point). The tolerance on the total energy, displacement, and maximum force was set as 2×10^{-5} Ha, 0.005 Å and 0.004 Ha/Å, respectively.

In the present study, we have selected two $LaFeO_3$ surfaces: (100) surface with LaFeO terminations and (121) surface, which is the preferred orientation for the explored compound. After the cleaving of the 3D lattice of $LaFeO_3$ across the chosen plans, a supercell of (2×2×1) was constructed. The vacuum was set to 20 Å to prevent the interaction between the atoms of the surface and those laying in the first plane of the second lattice along the Z-axis. Four planes have been considered with 160 atoms, the bottom two layers were fixed and the surface two atomic layers were left free for relaxation.

The adsorption energy (E_{ads}) of methylene blue (MB) on the $LaFeO_3$ surface was calculated using the following equation [18];

$$E_{ads} = E_{adsorbate-surface} - (E_{surface} + E_{adsorbate}) \qquad \text{(VI.2)}$$

where $E_{adsorbate+surface}$ is the total energy of the MB molecule adsorbed on the considered surface, $E_{surface}$ is the total surface energy before adsorption, and $E_{adsorbate}$ is the total energy of the MB molecule.

VI.2 Results and Discussion

IV.2.1 Structural Properties

The orthorhombic structure (SG *Pnma*; # 62) of the perovskite $LaFeO_3$ is illustrated in Figure VI.2.a. The unit cell of $LaFeO_3$ contains four formulas (20 atoms) and can be defined as a distorted FeO_6 corner-sharing network where each one of the four La atoms occupies the gaps between the octahedra as shown in Figure VI.2.b. In Table VI.1, we gathered the optimized equilibrium values of lattice parameters, volume, bond length, and bond angles using both GGA and GGA+U methods.

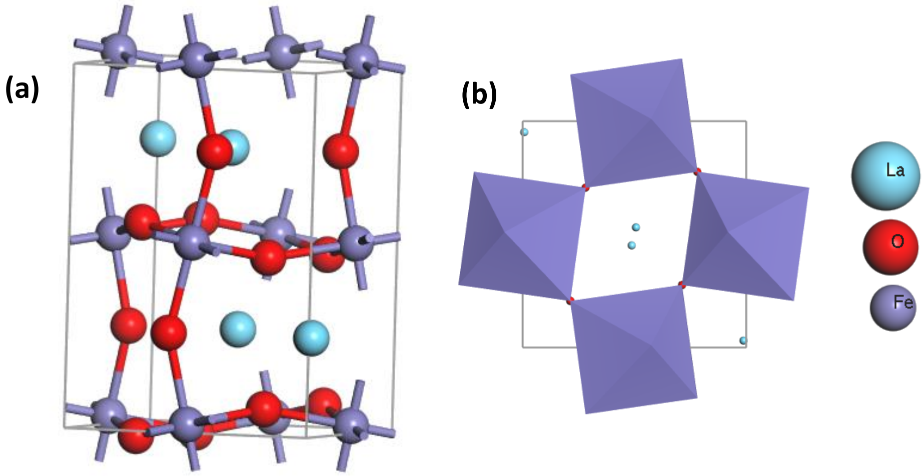

Figure VI.2: (a) A side and (b) onto view of the $LaFeO_3$ unit cell crystal structure.

From Table VI.1, one can observe that the values of the structural parameters obtained within GGA+U agree well with those reported in previous studies. However, GGA+U is known to overestimate the lattice parameters (and thus the unit cell volume) [9,13,14], which is the case compared with the obtained experimental results in Chapter 4.

Table VI.1: Calculated structural parameters of the $LaFeO_3$ orthorhombic structure using GGA and GGA+U, compared to those reported in previous studies.

	Our work		**References**
	GGA	GGA+U	
a (Å)	5.493	5.629	5.611[a], 5.6431[b], 5.551[c]
b (Å)	5.422	5.696	5.689[a],5.5772[b], 5.639[c]
c (Å)	7.716	7.989	7.970[a],7.9146[b], 7.918[c]
V ($Å^3$)	229.81	256.15	247.85[c]
Fe – O (Å)	1.952	2.042	2.041[b]
Fe – O (Å)	1.953	2.048	2.03[b]
Fe – O (Å)	1.959	2.057	2.034[b]
Fe – O – Fe	162.426	155.041	155.36[a], 154.03[b]
Fe – O – Fe	162.436	155.413	155.44[a]

[a] [1], [b][2] and [c][9]

Calculated bond length and angles reveal the non-perfect Fe-O octahedra. The results indicate that the use of GGA+U results (with a deviation of 0.71% and 0.11% for the bond length and angles, respectively) in more reliable results compared to that of the GGA method where a deviation of 3.94% for the bond length and 4.33% for the bond angles were obtained.

VI.2.2 Electronic and Magnetic Properties

The calculated electronic band structures of the G-AFM orthorhombic $LaFeO_3$ using GGA and spin-polarized GGA+U methods are presented in Figure VI.3. The $LaFeO_3$ perovskite shows a metallic behavior when using only GGA approximation as depicted in Figure VI.3.a. Regarding Figure VI.3.b, the distribution of majority and minority spin channels are similar and both of them show a semiconducting behavior with a band gap value of 2.27 eV. This band gap value is in good agreement with the present measured one (2.19 - 2.27 eV) and with the values reported in previous experimental and theoretical studies [7,9,15]. According to Figure VI.3.b, the maximum of the valence band and the minimum of the conduction band are both located at the Q point indicating a direct band gap semiconductor which is in accordance with the obtained experimental values.

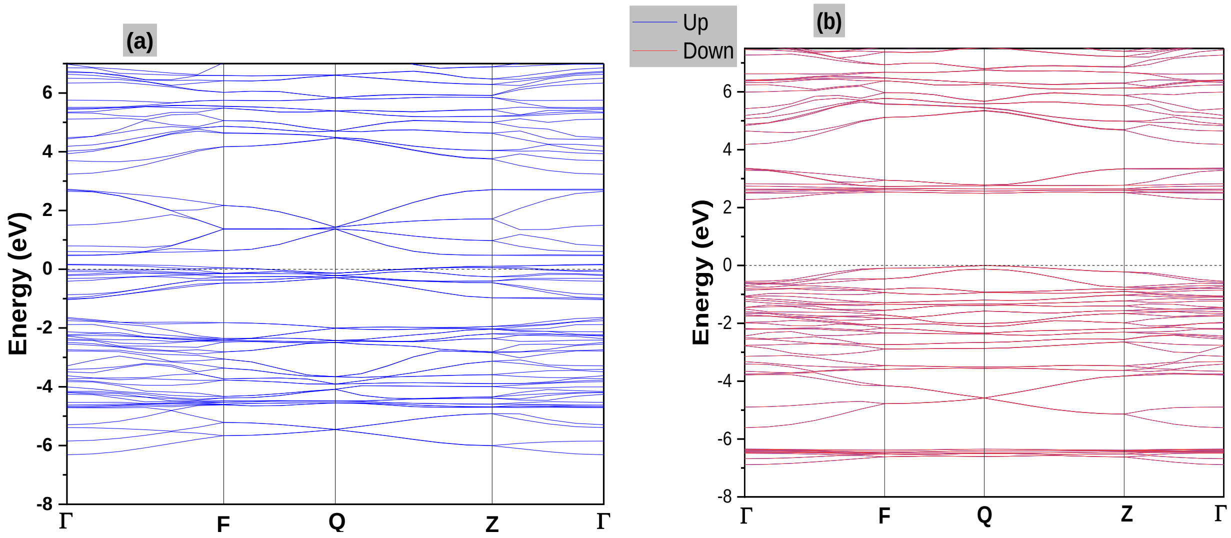

Figure VI.3: Calculated band structure obtained using the (a) GGA and (b) GGA+U methods.

Figure IV.4 illustrates the total spin-dependent density of states of the ferrite lanthanum perovskite. It can be seen that the total density of states appears symmetrical for both spin-up and spin-down states, which justifies the spin degeneracy of the electronic states as observed in the band structure. This similarity means that the net magnetic moment per cell is zero.

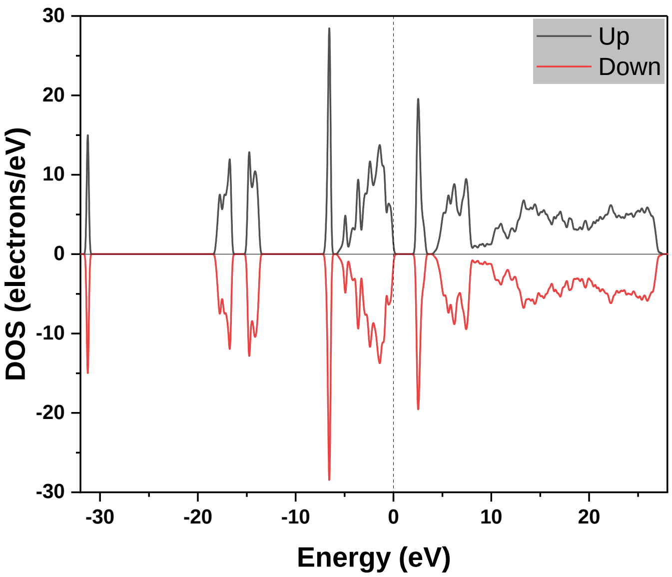

Figure VI.4: Total density of states for both spin-up and spin-down states.

To highlight the individual contribution of each orbital on the density of states, the total and partial densities of states of the La, Fe, and O atoms were calculated and shown in Figure VI.5. The part of the valence band located between -8 eV and -6 eV mainly originates from the localized Fe-3*d* electrons with a minor contribution of the O -2*p* electrons. The upper region of the valence band, -6 - 0 eV, comes essentially from O -2*p* states with a small contribution of the La -5*d*, and Fe -3*d* states. The lowest part of the conduction band, located in the energy window 1.9 - 3.9 eV, is formed principally by the Fe -3*d* states with a relatively small contribution of O -2*p*. The second part, between 4 – 8 eV, is due basically to La -5*d* states with insignificant contributions from other states. The slight shift of the valence band from the Fermi level indicates that $LaFeO_3$ is a p-type semiconductor.

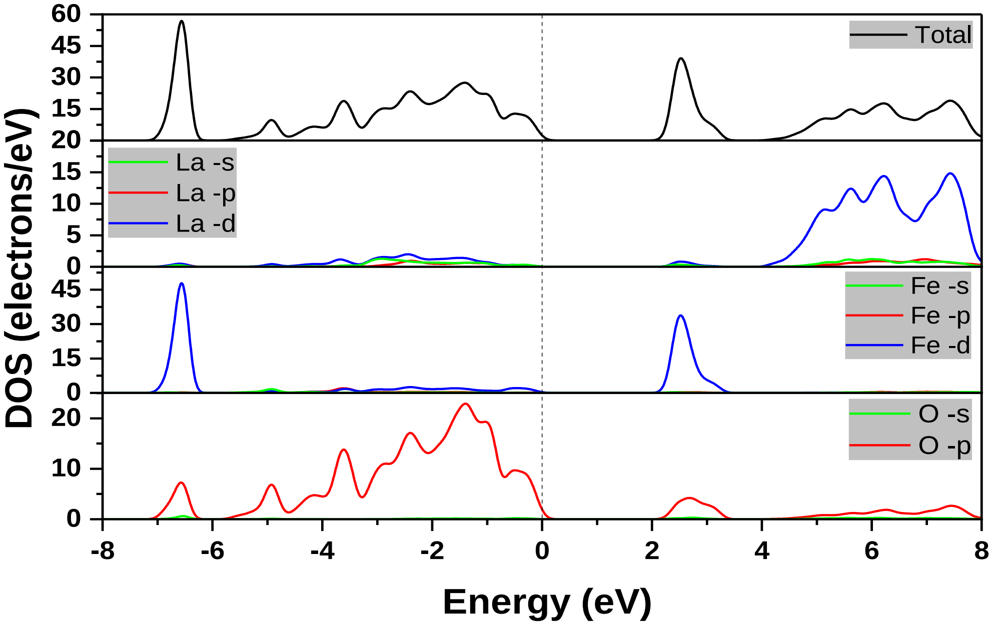

Figure VI.5: Total and partial density of states of the $LaFeO_3$, La, Fe and O orbitals, respectively.

The total and individual magnetic moments of the orthorhombic $LaFeO_3$ compound are illustrated in Table VI.2. The individual magnetic moment of both La and O atoms is equal to zero while it is 4.11 μ_0B for the Fe one, this value is in accordance with previously reported ones [14,16]. Due to the antiparallel of each atom to its neighbor, the contribution of each two Fe atoms cancels out each other which results in zero magnetization. The μ_B total of $LaFeO_3$ perovskite is 0 μB, indicating its antiferromagnetism nature.

Table VI.2: Calculated total and individual atomic magnetic moments (μ_B in μ_0B) of orthorhombic $LaFeO_3$

Compound	**Total**	**La**	**Fe**	**O**
$LaFeO_3$	0	0	4.11	0
Other works			4.07 [11], 4.14 [13]	

The chemical bonding of the considered compound was explored through the charge density maps and Mulliken population analysis given in Figure VI.6 and Table VI.3, respectively. The electronic charge density distributions across the (001) and (110) plans, depicted in Figure VI.6, reveal an overlap between the states of Fe and O atoms, indicating the presence of covalent bonding.

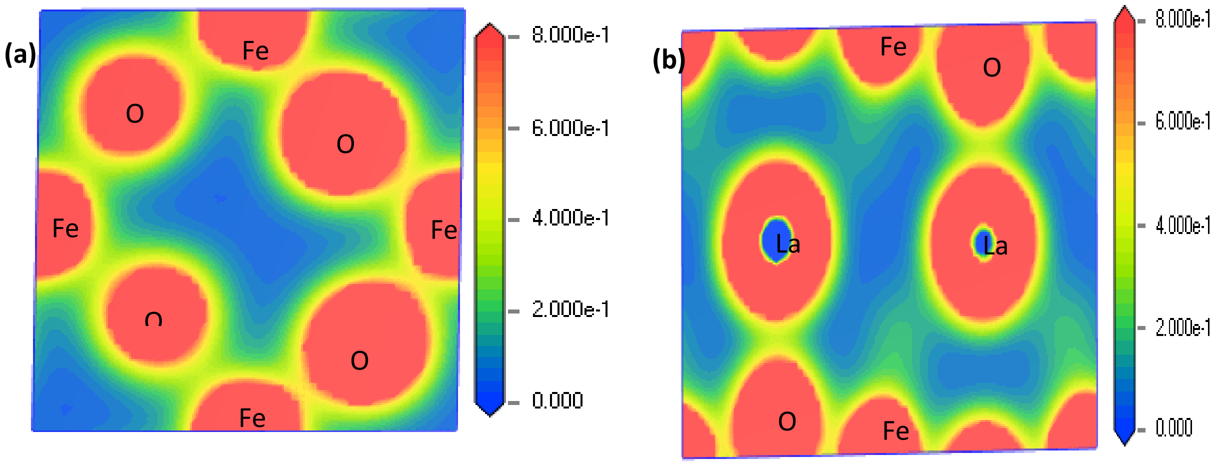

Figure VI.6: Electron charge density along the (a) (001) and (b) (110) plans.

From Table VI.3, it can be seen that the charge transferred from the La atom to the O atoms is twice that transferred from the Fe atom to the O atom. This is an indication that the La-O bond is more ionic, while Fe-O is more covalent. This result is also confirmed by the value of the bond population. Note that our results are consistent with those reported by Yongjun et *al.* [17].

Table VI.3: Charge transfer and bond population obtained from Mullikan population analysis for $LaFeO_3$.

Ion	La	Fe	O	Bond	Population
Total	4.72	5.64	3.40	Fe – O	0.31
Charge (e)	1.57	0.83	-0.8	La – O	0.26

VI.2.3 Surface Optimization

Figure IV.7 illustrates the optimized structure of the clean (121) $LaFeO_3$ surface. In general, the $LaFeO_3$ surfaces present at least two types of possible terminations; i.e. lanthanum termination and iron termination. This is not the case for the (121) surface, where this surface presents only one termination that contains both La and Fe atoms with the formulation LaFeO which was previously confirmed by Blanck et *al.* [18]. After surface optimization, the La and Fe atoms move upward while those of O move downward which indicates an enrichment of lanthanum and iron on the (121) $LaFeO_3$ surface.

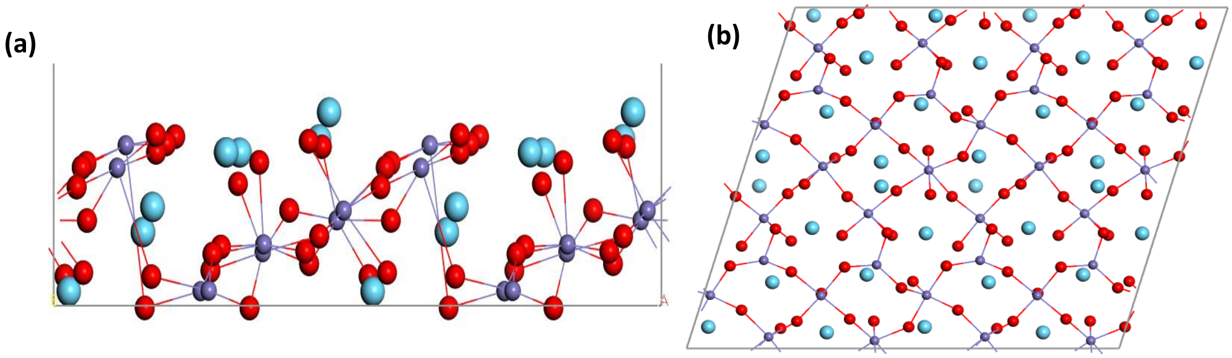

Figure IV.7: (a) Side and (b) onto view of the (121) $LaFeO_3$ surface.

The optimized structure of the clean (100) $LaFeO_3$ surface is presented in Figure IV.8, from which one can observe an alternance of the LaFeO an -O – O – layers.

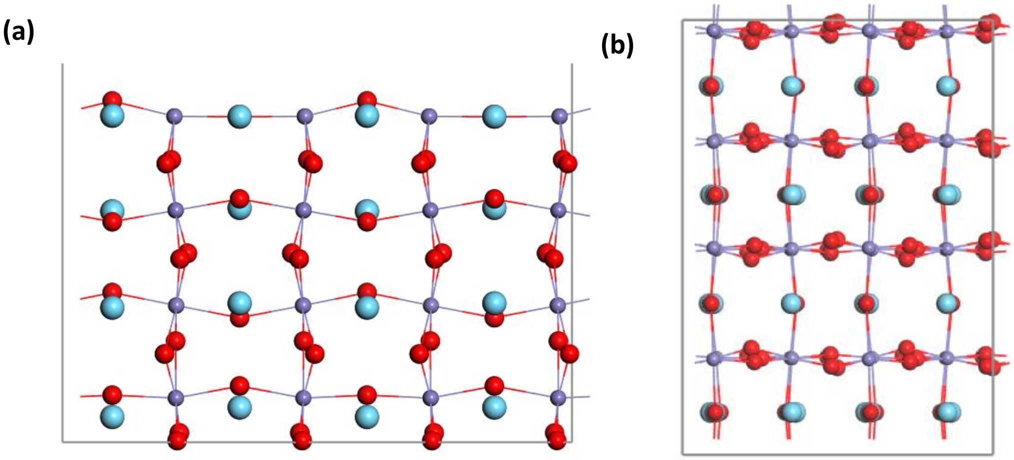

Figure IV.8: (a) Side and (b) onto view of the (100) $LaFeO_3$ surface.

VI.2.4 Optimization of the adsorbate

The optimized geometry of the methylene blue dye with the molecular formal $C_{16}H_{18}N_3ClS$ is shown in Figure IV.9. The calculated bond lengths of the C – N, C – H, C – C, and C – S bonds are reported in Table VI.4 compared to the experimental values. Our results agree well with the experimental ones.

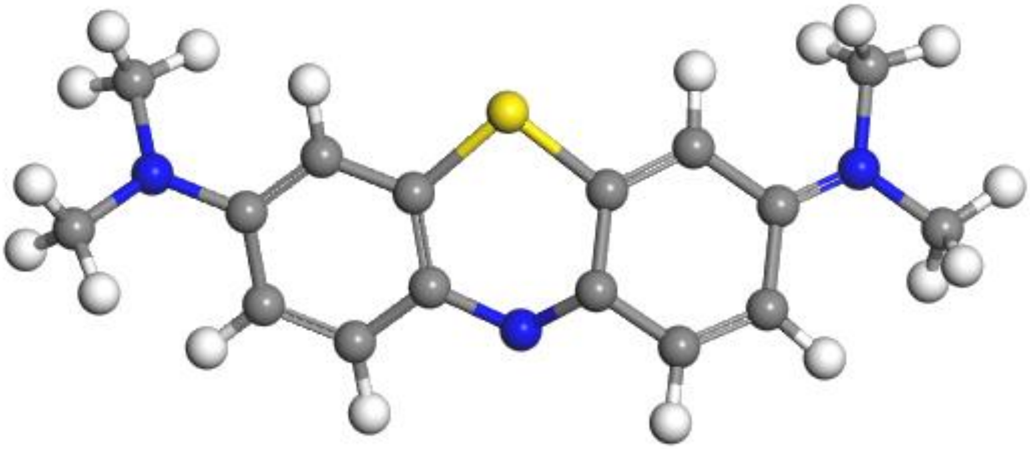

Figure VI.9: Optimized equilibrium geometry of Methylene Blue dye molecule.

Table VI.4: Calculated bond lengths of the methylene blue compared to the experimental values.

Bond	Calculated bond length (Å)	Experimental bond length (Å) [19]
C – H	1.081 – 1.111	0.77 – 1.12
C – N	1.323 – 1.474	1.331 – 1.465
C – C	1.392 – 1.484	1.341 – 1.445
C – S	1.812 – 1.823	1.721 – 1.728

VI.2.5 Methylene Blue Adsorption on $LaFeO_3$ Surface

The optimized structures of the adsorption configuration are shown in Figures VI.10 and VI.11. Table VI.5 reports the adsorption properties of MB on the (121) and (100) $LaFeO_3$ surfaces. Due to the high computational costs, the parallel position of methylene blue was chosen based on previous studies that show good adsorption results when the MB dye molecules are oriented parallel to the adsorbent surface [20-22]. As can be seen from Table VI.5, the adsorption of MB on the (100) $LaFeO_3$ exhibits the highest adsorption energy (-1.21 eV) compared to that of the (121) surface (-1.15 eV). The negative values of adsorption energy suggest thermodynamically preferred exothermic adsorption [23], which is consistent with the obtained experimental results (see Chapter 5). As depicted in Figure VI.10 and Table VI.5, the shortest atomic distance of $LaFeO_3$-MB is that of the H – O bond (equal to 2.706 Å), therefore indicating that the MB molecule tends to be adsorbed on the O sites of the (121) $LaFeO_3$ surface.

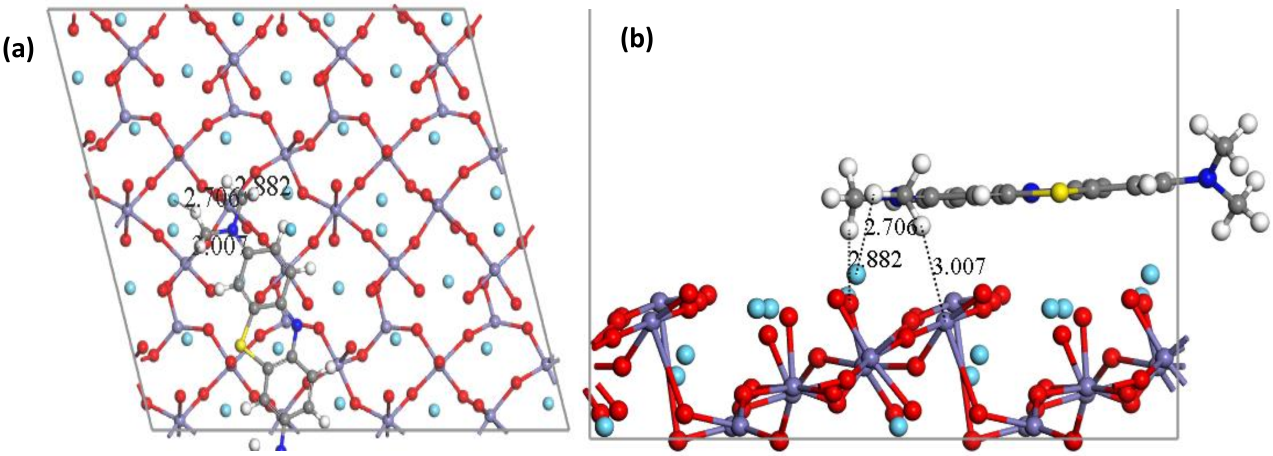

Figure VI.10: The configuration of MB molecular adsorption on $LaFeO_3$ (121) surface (a) onto view and (b) side view.

The length of the H - Fe bond is 2.6 Å, shorter than H - La (2.691 Å) and H - O (2.751 Å) (see Figure VI.11). This indicates that the Fe sites dominate the MB adsorption process on the (100) $LaFeO_3$ surface. According to the literature, both Fe and O sites are found to be favorable for the adsorption of different molecules, such as ethanol, O_2, NO and H_2, on the $LaFeO_3$ surface [24-27].

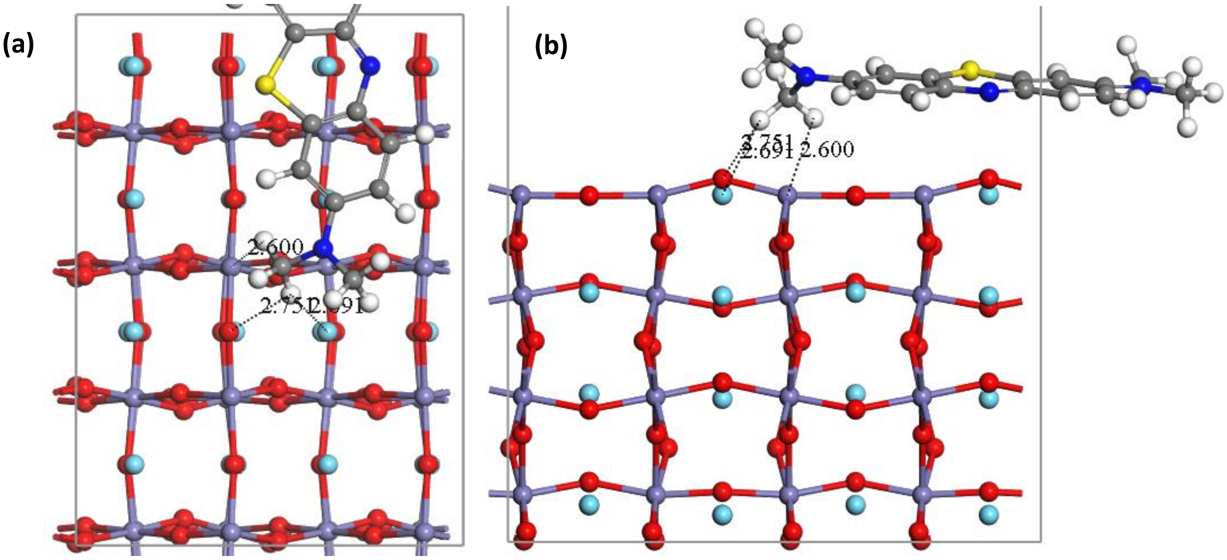

Figure VI.11: The configuration of MB molecular adsorption on (100) $LaFeO_3$ surface (a) onto view and (b) side view.

For both configurations, the bonds were hard to form due to the long equilibrium distance between the MB atoms and the $LaFeO_3$ surface atoms. Generally, the molecule–surface distance is 2 Å for a chemisorption process and 3 Å for physisorption [28]. Although relatively high values of the E_{ads} are obtained, the absence of any bond formation could be an indication of a physisorption process [29] that was already confirmed by the experimental values in Chapter 5. The values range of these distances and the adsorption energies suggest that the adsorption of MB on the $LaFeO_3$ surface occurs due to a weak hydrogen bonding and Van Der Wals interactions [30].

Table VI.5: Properties of the adsorption of MB on the (121) and (100) $LaFeO_3$ surfaces.

	d(H – La) (Å)	**d(H – Fe) (Å)**	**d(H – O) (Å)**	**E_{ads} (eV)**
(121)	3.007	2.882	2.706	-1.15
(100)	2.691	2.600	2.751	-1.21

References

[1] Okugawa, T., Weng, H., Yamamoto, T., Ozawa, T. C., & Kawazoe, Y. (2018). Weakly spin-dependent band structures of antiferromagnetic perovskite LaMO3 (M= Cr, Mn, Fe). *Journal of Physics: Condensed Matter, 30*(7), 075502. DOI: 10.1088/1361-648X/aaa4e8.

[2] Li, Y. R., Wu, M. S., Huang, H., & Ma, D. M. (2017). The structural properties of LaRO3 (R= Cr, Mn, Fe): a first-principles calculation. *Journal of Physics: Conference Series, 827*(1), 012005. DOI: 10.1088/1742-6596/827/1/012005.

[3] Jia, T., Zhao, H., Wang, Y., Gao, Y., & Zeng, S. (2017). First-principles study on the electronic, optical and thermodynamic properties of ABO3 (A= La, Sr, B= Fe, Co) perovskites. *RSC Advances, 7*(62), 38798-38804. DOI: 10.1039/C7RA05720C.

[4] Khalil, K. M. S., Mahmoud, A. H., & Khairy, M. (2022). Formation and textural characterization of size-controlled LaFeO3 perovskite nanoparticles for efficient photocatalytic degradation of organic pollutants. *Advanced Powder Technology, 33*(1), 103429. DOI: 10.1016/j.apt.2021.12.011.

[5] Phan, T. T. N., Tran, T. M., Nguyen, T. T., Le, Q. D., & Nguyen, T. H. (2018). Optimizing photocatalytic performance of hydrothermally synthesized LaFeO3 by tuning material properties and operating conditions. *Journal of Environmental Chemical Engineering, 6*(1), 1209-1218. DOI: 10.1016/j.jece.2017.12.020.

[6] Wiranwetchayan, O., Kaewkhao, J., Kothan, S., & Limsuwan, P. (2019). Characterization of perovskite LaFeO3 synthesized by microwave plasma method for photocatalytic applications. *Ceramics International, 45*(4), 4802-4809. DOI: 10.1016/j.ceramint.2018.11.177.

[7] Jana, S., Mohapatra, A., & Mahalakshmi, S. (2019). Charge disproportionate antiferromagnetism at the verge of the insulator-metal transition in doped LaFeO3. *Physical Review B, 99*(7), 075106. DOI: 10.1103/PhysRevB.99.075106.

[8] Azouzi, W., Lazzez, M., Jemai, R., & Gargouri, M. (2021). Structural and optical properties of LaFe1-xVxO3 as predicted by a DFT study. *Materials Today Communications, 26*, 101876. DOI: 10.1016/j.mtcomm.2021.101876.

[9] Javaid, S., & Akhtar, M. J. (2014). Pressure-induced magnetic, structural, and electronic phase transitions in LaFeO3: A density functional theory (generalized gradient approximation)+ U study. *Journal of Applied Physics, 116*(2), 023908. DOI: 10.1063/1.4889603.

[10] Maximoff, S. N., Ernzerhof, M., & Scuseria, G. E. (2004). Current-dependent extension of the Perdew–Burke–Ernzerhof exchange-correlation functional. *The Journal of Chemical Physics, 120*(5), 2105-2109. DOI: 10.1063/1.1642638.

[11] Delley, B. (2000). From molecules to solids with the DMol3 approach. *The Journal of Chemical Physics, 113*(18), 7756-7764. DOI: 10.1063/1.1316015

[12] Luo, Y., Liu, J., Zhang, X., & Zhang, S. (2014). Effects of global orbital cutoff value and numerical basis set size on accuracies of theoretical atomization energies. *Theoretical Chemistry Accounts, 133*, 1-11. DOI: 10.1007/s00214-013-1405-8.

[13] Peles, A. (2012). GGA+ U method from first principles: application to reduction–oxidation properties in ceria-based oxides. *Journal of Materials Science, 47*, 7542-7548. DOI: 10.1007/s10853-012-6603-9.

[14] Obodo, K. O., & Chetty, N. (2013). First principles LDA+ U and GGA+ U study of protactinium and protactinium oxides: dependence on the effective U parameter. *Journal of Physics: Condensed Matter, 25*(14), 145603. DOI: 10.1088/0953-8984/25/14/145603.

[15] Jia, T., Zhao, H., Wang, Y., Gao, Y., & Zeng, S. (2017). First-principles study on the electronic, optical and thermodynamic properties of ABO3 (A= La, Sr, B= Fe, Co) perovskites. RSC Advances, 7(62), 38798-38804. DOI: 10.1039/C7RA05720C.

[16] Timrov, I., Marzari, N., & Cococcioni, M. (2020). Electronic structure of pristine and Ni-substituted LaFeO3 from near edge x-ray absorption fine structure experiments and first-principles simulations. *Physical Review Research, 2*(3), 033265. DOI: 10.1103/PhysRevResearch.2.033265.

[17] Zhou, Y., Huang, L., Zhang, Y., & Zhang, D. (2021). The electronic properties and structural stability of LaFeO3 oxide by niobium doping: A density functional theory study. *International Journal of Hydrogen Energy, 46*(13), 9193-9198. DOI: 10.1016/j.ijhydene.2020.12.198.

[18] Blanck, D., Berrier, E., & Paul, J. F. (2017). First-Principles Investigation of the Relevant Surfaces Exposed by Polycrystalline LaFeO3. *ChemCatChem, 9*(12), 2383-2389. DOI: 10.1002/cctc.201700170

[19] Marr, H. E., Stewart, J. M., & Chiu, M. F. (1973). The crystal structure of methylene blue pentahydrate. *Acta Crystallographica Section B: Structural Crystallography and Crystal Chemistry, 29*(4), 847-853. DOI: 10.1107/S0567740873004562.

[20] Djellali, S., Touati, A., Semmeq, A., Kebaili, M., Badawi, M., & Bonilla-Petriciolet, A. (2022). Unravelling the methylene blue adsorption mechanism on doped and nondoped polyaniline: A combined molecular modeling and experimental investigation. *International Journal of Chemical Engineering*. DOI: 10.1155/2022/3181963.

[21] Allangawi, A., Aljar, M. A. A., Ayub, K., Abd El-Fattah, A., & Mahmood, T. (2023). Removal of methylene blue by using sodium alginate-based hydrogel; validation of experimental findings via DFT calculations. *Journal of Molecular Graphics and Modelling, 122*, 108468. DOI: 10.1016/j.jmgm.2023.108468

[22] Greathouse, J. A., Cygan, R. T., Fredrich, J. T., Jerauld, G. R., & Gable, C. W. (2015). Methylene blue adsorption on the basal surfaces of kaolinite: Structure and thermodynamics from

quantum and classical molecular simulation. *Clays and Clay Minerals, 63*(3), 185-198. DOI: 10.1346/CCMN.2015.0630302

[23] Lgaz, H., & Lee, H. (2023). Computational Exploration of Phenolic Compounds in Corrosion Inhibition: A Case Study of Hydroxytyrosol and Tyrosol. *Materials, 16*(18), 6159. DOI: 10.3390/ma16186159.

[24] Liu, X., Zhang, Y., Chen, Y., & Li, L. (2013). Theoretical calculation of ethanol molecule adsorption on LaFeO3 (010) surface. *Computational Materials Science, 68*, 90-94. DOI: 10.1016/j.commatsci.2012.10.017

[25] Liu, X., Hu, J., Cheng, B., Qin, H., Zhao, M., & Yang, C. (2009). First-principles study of O2 adsorption on the LaFeO3 (0 1 0) surface. *Sensors and Actuators B: Chemical*, *139*(2), 520-526. DOI: 10.1016/j.snb.2009.03.052.

[26] Sun, L., Hu, J., Gao, F., Zhang, Y., & Qin, H. (2011). First-principle study of NO adsorption on the LaFeO3 (0 1 0) surface. *Physica B: Condensed Matter*, *406*(21), 4105-4108. DOI: 10.1016/j.physb.2011.07.060

[27] Boateng, I. W., Tia, R., Adei, E., Dzade, N. Y., Catlow, C. R. A., & De Leeuw, N. H. (2017). A DFT+ U investigation of hydrogen adsorption on the LaFeO 3 (010) surface. *Physical Chemistry Chemical Physics*, *19*(10), 7399-7409. DOI: 10.1039/C6CP08698E.

[28] Kokalj, A., Kovačević, N., Peljhan, S., Finšgar, M., Lesar, A., & Milošev, I. (2011). Triazole, benzotriazole, and naphthotriazole as copper corrosion inhibitors: I. Molecular electronic and adsorption properties. *ChemPhysChem*, *12*(18), 3547-3555. DOI: 10.1002/cphc.201100537.

[29] Qin, X., Cui, H., & Zhou, Q. (2023). Physisorption Behaviors of Organochlorine Pesticides on the InP3 Monolayer from Theoretical Insight. *ACS omega*, *8*(35), 32168-32175. DOI: 10.1021/acsomega.3c04665.

[30] Albert, A. (2012). *Selective toxicity: the physico-chemical basis of therapy*. Springer Science & Business Media. DOI: 10.1007/978-1-4899-6832-6.

General Conclusion

$LaFeO_3$ nanoparticles were successfully synthesized through the sol-gel method. Two different powders were prepared using two different precursors, nitrate and chloride salts. Through TG, DTG, XRD, BET, SEM, EDX, and UV-Vis analyses, the significant effect of the used precursor on the thermal behavior, surface area, morphology, structural and optical properties as well as the catalytic and photocatalytic performance was highlighted in detail. TG and DTG analysis revealed the formation of the perovskite phase at 900°C and 600°C for the powder prepared using chloride and nitrate salts, respectively. Both powders crystallize in the orthorhombic perovskite structure (Pnma, 62) with crystallite between 42.51 and 86.26 nm. The surface area of the $LaFeO_3$ nanoparticles obtained from BET analysis, are found to be equal to 11.56, 8.90, and 5.94 m^2/g for the NLF1, NLF2, and CLF3 samples, respectively. Using chloride precursors, the samples show a nanoporous morphology originating from the release of chlorine from the $LaFeO_3$ matrix. The use of nitrate salts leads to the formation of cavities 20 µm in diameter, surrounded by microporous walls 5 µm in diameter. The EDX measurements revealed the presence of chlorine in the powders calcined at 600 and 900 °C and its disappearance with the rise of temperature to 1000 °C. The porosity of the three prepared samples is equal to 25.19, 29.24, and 40.21% for the NLF1, NLF2, and CLF3, respectively. The estimated band gap of the three samples, from the absorbance spectra, is about 2.25, 2.27, and 2.19 eV for NLF1, NLF2, and CLF3, respectively.

The adsorption capacity of methylene blue on the $LaFeO_3$ surface was equal to 8.135, 8.834, and 9.213 $mg.g^{-1}$ with an adsorption efficiency of 42.3, 45.7 and 47.8 % for NLF1, NLF2 and CLF3 samples, respectively. The adsorption kinetic study revealed that the experimental data are well fitted to the pseudo-second-order kinetic model, with a correlation coefficient of $R^2 = 0.99977$, 0.9999, and 0.99943 for NLF1, NLF2, and CLF3, respectively, while the intraparticle diffusion models showed that the adsorption may occur in two steps where external adsorption onto the $LaFeO_3$ surface is followed by intraparticle diffusion. The isotherm study shows that the Freundlich model describes well the adsorption process indicating a favorable and multilayer adsorption where the $LaFeO_3$ powder presents a slightly heterogenous surface. The thermodynamic adsorption study demonstrates the spontaneous, favorable, and exothermic adsorption process. Moreover, the ($-13.893 \rightarrow -20.228$ $kJ.mol^{-1}$) range values correspond to physical interactions, generally Van Der Walls, electrostatic or hydrogen bonding.

The photocatalytic tests revealed that the CLF3 sample exhibits the highest photodegradation capacity (100%) in a contact time of 40 min. The high photocatalytic efficiency of the MB dye removal using $LaFeO_3$ powder shows the potential value of using this mixed oxide as a dye removal for several technological and environmental applications.

Density functional theory (DFT) was used to investigate the fundamental ground state properties, i.e. structural, electronic, and magnetic properties of the studied material, and also to understand the adsorption properties of methylene blue on the (100) and (121) $LaFeO_3$ surfaces. Structural data, including lattice parameters, bond angles, and bond lengths are consistent with the previously experimental and theoretical ones. The calculated band structure using a Hubbard parameter of 4.5 eV gave a direct band gap of 2.27 eV, which agrees well with the measured values. The DOS calculations revealed that the Fe -3*d* and O -*2p*, mainly dominate the valence bands states while the conduction bands are mainly contributed by the La -5*d* and Fe -3*d* states. According to the electronic density maps and Mulliken population analysis, a covalence bonding could be remarkable between the Fe and O atoms. Moreover, the calculated individual and total magnetic moments were found to be 4.11 and 0 μ_0B indicating the antiferromagnetic nature of the $LaFeO_3$ perovskite. All the theoretical results are consistent with the experimentally obtained ones.

The study of the adsorption of MB on the (100) and (121) surfaces of $LaFeO_3$ showed that the (100) $LaFeO_3$ surface has the highest adsorption energy of -1.21 eV compared to that of the (121) surface (equal to -1.15 eV); the adsorption turns out to be exothermic for both surfaces. The smallest adsorption distance between the adsorbent and adsorbate is equal to 2.706 Å for the (121) surface and 2.6 Å for the (100) surface, while the dominant site for the adsorption of MB on the (121) and (100) surface was estimated to be O and Fe site, respectively. For both configurations, the bonds are hard to form due to the long equilibrium distance between the MB atoms and the $LaFeO_3$ surface atoms. According to the adsorption energies and distances, the adsorption of MB on the $LaFeO_3$ surface occurs due to the hydrogen bonding and Van Der Wals interactions, which is already confirmed by the experimental adsorption results.

Abstract

In this study, $LaFeO_3$ powders with crucial catalytic and photocatalytic performance were successfully prepared through the sol-gel method using chloride and nitrate salts. The influence of the used precursor on the crystallinity, morphology, specific surface area, and optical properties was investigated. TGA and XRD patterns confirmed the formation of the $LaFeO_3$ orthorhombic perovskite phase (Pnma, #62). SEM images highlighted a significant effect of the precursor type on the surface morphology of the synthesized nanoparticles. The obtained band gap varies between 2.19 - 2.27 eV. The kinetic and isotherm adsorption studies revealed that the adsorption of MB molecules on $LaFeO_3$ nanoparticles fitted well with the pseudo-second-order and Freundlich models. Moreover, the thermodynamic study demonstrated that the adsorption of MB on the $LaFeO_3$ samples is spontaneous, exothermic, and more favorable at low temperatures while the magnitude of enthalpy changes energies suggested a physisorption. Hence, $LaFeO_3$ samples prepared with chloride salts are expected to show high photodegradation efficiency of MB dye. In addition, our study was completed by the theoretical investigation, using DFT within GGA+U, of the Bulk and surface properties of $LaFeO_3$. A perfect agreement is found between the experimental results and the theoretical ones.

Keywords: $LaFeO_3$, Nanopores, Adsorption, Photocatalysis, Kinetic models, DFT

Résumé

Dans cette étude, des poudres de LaFeO3 présentant des performances catalytiques et photocatalytiques cruciales ont été préparées avec succès par la méthode sol-gel en utilisant des sels de chlorure et de nitrate. L'influence du précurseur sur la cristallinité, la morphologie, la surface spécifique et les propriétés optiques a été étudiée. L'ATG et la DRX ont confirmé la formation de la phase pérovskite orthorhombique $LaFeO_3$ (Pnma, #62). Les images MEB ont mis en évidence un effet significatif de type précurseur sur la morphologie de surface des nanoparticules synthétisées. La bande interdite obtenue varie entre 2.19 et 2.27 eV. L'étude de la cinétique d'adsorption et l'étude isotherme ont révélé que l'adsorption des molécules de MB sur les nanoparticules de $LaFeO_3$ correspondait bien au modèle de pseudo-second ordre et de Freundlich. De plus, l'étude thermodynamique a démontré que l'adsorption du MB sur les échantillons de LaFeO3 est spontanée, exothermique et plus favorable à basse température, tandis que les valeurs de l'enthalpie suggèrent une physisorption. Par conséquent, les échantillons de $LaFeO_3$ préparés avec des sels de chlorure devraient présenter une efficacité de photodégradation élevée du colorant MB. De plus, notre étude a été complétée par l'investigation théorique, en utilisant DFT avec GGA+U, des propriétés du massif et de surface de $LaFeO_3$. Un accord parfait est trouvé entre les résultats expérimentaux et les résultats théoriques.

Mots clés : $LaFeO_3$, Nanopores, Adsorption, Photocatalyse, modèles cinétiques, DFT

ملخص

في هذه الدراسة، تم تحضير مساحيق $LaFeO_3$ ذات الأداء الامتزازي والتحفيزي الضوئي بنجاح من خلال طريقة سول جل باستخدام أملاح الكلوريد والنترات. تم فحص تأثير السلائف المستخدمة على البلورة والتشكل والمساحة السطحية المحددة والخصائص البصرية. كشفت مخططات TGA وXRD أن مساحيق $LaFeO_3$ المصنعة اضهرت تشكل تركيبة البيروفسكايت (Pnma, 62#) باستخدام سلائف النترات والكلوريد. كشفت صور SEM عن التأثير الكبير لنوع السلائف على البنية السطحية للمساحيق المحضرة. اما بالنسبة لفجوة الطاقة فقد كانت محصورة بين 2.19 و2.27 الكترون فولط. كشفت دراسات الامتزاز الحركي والإيزوثرم أن امتزاز جزيئات MB على الجسيمات النانوية $LaFeO_3$ يتناسب جيدًا مع نموذج الامر الثانوي ونموذج فريندليش. بينما توضح الدراسة الديناميكية الحرارية أن امتزاز MBعلى عينات $LaFeO_3$ يكون تلقائيًا وطاردًا للحرارة وأكثر ملاءمة في درجات الحرارة المنخفضة في حين يشير حجم التغيرات الحرارية إلى وجود امتزاز فيزيائي. أظهر عينات$LaFeO_3$ المحضرة بأملاح الكلوريد كفاءة عالية في التحفيز الضوئي لصبغة ازرق الميثيلين.

تم استكمال الدراسة باستخدام حسابات نظرية الكثافة الوظيفية (DFT) باستعمال GGA+U لدراسة البيروفسكايت $LaFeO_3$ في الحالة الصلبة والسطح. اظهرت الحسابات توافق في النتائج مقارنة بالنتائج التجريبية.

كلمات مفتاحية:$LaFeO_3$ ؛ المسام النانوية؛ الامتزاز؛ التحفيز الضوئي؛ نماذج الامتزاز الحركي؛ DFT